Extending synchrotron X-ray refraction imaging techniques to the quantitative analysis of metallic materials

René Laquai

Dissertation

zur Erlangung des akademischen Grades
"doctor rerum naturalium"
(Dr. rer. nat.)
in der Wissenschaftsdiziplin: "Angewandte Physik"

eingereicht an der
Mathematisch-Naturwissenschaftlichen Fakultät
Institut für Physik und Astronomie
der Universität Potsdam
und
Bundesanstalt für Materialforschung und -prüfung (BAM)

Ort und Tag der Disputation: Potsdam, 10.02.2022

Hauptbetreuer: Prof. Dr. Giovanni Bruno
Zweitbetreuerin: Prof. Dr. Claudia Fleck
Gutachterin: Prof. Dr. Fulvia Arfelli

Published online on the
Publication Server of the University of Potsdam:
https://doi.org/10.25932/publishup-54183
https://nbn-resolving.org/urn:nbn:de:kobv:517-opus4-541835

Acknowlegments

I like to express my sincere thanks to the following persons without whom this work would not have been possible:

My supervisor, Prof. Dr. Giovanni Bruno, for his guidance and feedback throughout the project and, especially, his help with the publications related to this thesis. Prof. Dr. Claudia Fleck for her role as second supervisor. Dr. Bernd R. Müller who mentored this work, whose knowledge and experience steered me through the project, and who supervised the beamtimes at BAMline. Dr. Andreas Kupsch who was part of the beamtime team and who assisted with his insights and knowledge about the subject matter. Prof. Dr. Manfred P. Hentschel and Axel Lange, the original inventors of X-ray refraction topography. Thomas Wolk and Ralf Britzke for their technical support during beamtimes.

Jens Nellesen, Dr. Galina Kasperovich, Dr. Jan Haubrich, Prof. Dr. Guillermo Requena, Thomas Schaupp, and Dr. Axel Griesche who were project partners for the different case studies and provided samples, results from reference measurements, technical equipment and the materials science questions behind each case study.

All the other collegues from department 8.5 Micro-NDT of the "Bundesanstalt für Materialprüfung und -forschung (BAM)" for the friendly and inspiring atmosphere.

Finally, BAM for funding this project through the MIS program (Ideen_2013_25).

Abstract

In this work, two X-ray refraction based imaging methods, namely, synchrotron X-ray refraction radiography (SXRR) and synchrotron X-ray refraction computed tomography (SXRCT), are applied to analyze quantitatively cracks and porosity in metallic materials. SXRR and SXRCT make use of the refraction of X-rays at inner surfaces of the material, e.g., the surfaces of cracks and pores, for image contrast. Both methods are, therefore, sensitive to smaller defects than their absorption based counterparts X-ray radiography and computed tomography. They can detect defects of nanometric size. So far the methods have been applied to the analysis of ceramic materials and fiber reinforced plastics. The analysis of metallic materials requires higher photon energies to achieve sufficient X-ray transmission due to their higher density. This causes smaller refraction angles and, thus, lower image contrast because the refraction index depends on the photon energy. Here, for the first time, a conclusive study is presented exploring the possibility to apply SXRR and SXRCT to metallic materials. It is shown that both methods can be optimized to overcome the reduced contrast due to smaller refraction angles. Hence, the only remaining limitation is the achievable X-ray transmission which is common to all X-ray imaging methods. Further, a model for the quantitative analysis of the inner surfaces is presented and verified.

For this purpose four case studies are conducted each posing a specific challenge to the imaging task. Case study A investigates cracks in a coupon taken from an aluminum weld seam. This case study primarily serves to verify the model for quantitative analysis and prove the sensitivity to sub-resolution features. In case study B, the damage evolution in an aluminum-based particle reinforced metal-matrix composite is analyzed. Here, the accuracy and repeatability of subsequent SXRR measurements is investigated showing that measurement errors of less than 3 % can be achieved. Further, case study B marks the fist application of SXRR in combination with *in-situ* tensile loading. Case study C is out of the highly topical field of additive manufacturing. Here, porosity in additively manufactured Ti-Al6-V4 is analyzed with a special interest in the pore morphology. A classification scheme based on SXRR measurements is devised which allows to distinguish binding defects from keyhole pores even if the defects cannot be spatially resolved. In case study D, SXRCT is applied to the analysis of hydrogen assisted cracking in steel. Due to the high X-ray attenuation of steel a comparatively high photonenergy of 50 keV is required here. This causes increased noise and lower contrast in the data compared to the other case studies. However, despite the lower data quality a quantitative analysis of the occurance of cracks in dependence of hydrogen content and applied mechanical load is possible.

Kurzfassung

In der vorliegenden Arbeit werden die zwei, auf Refraktion basierende, Röntgenbildgebungsverfahren Synchrotron Röntgen-Refraktions Radiographie (engl.: SXRR) und Synchrotron Röntgen-Refraktions Computertomographie (engl.: SXRCT) für die quantitative Analyse von Rissen und Porosität in metallischen Werkstoffen angewandt. SXRR und SXRCT nutzen die Refraktion von Röntgenstrahlen an inneren Oberflächen des Materials, z.B. die Oberflächen von Rissen und Poren, zur Bildgebung. Beide Methoden sind daher empfindlich gegenüber kleineren Defekten als ihre auf Röntgenabsorption basierenden Gegenstücke, Röntgenradiographie und Röntgen-Computertomographie. Sie sind in der Lage Defekte von nanometrischer Größe zu detektieren. Bislang wurden die Methoden für die Analyse von keramischen Werkstoffen und faserverstärkten Kunststoffen eingesetzt. Die Analyse von metallischen Werkstoffen benötigt höhere Photonenenergien benötigt werden um eine ausreichende Transmission zu erreichen. Dies hat kleinere Refraktionswinkel, und damit geringeren Bildkontrast, zur Folge, da der Brechungsindex von der Photonenenergie abhängt. Hier wird erstmals eine umfassende Studie vorgelegt, welche die Möglichkeiten zur Untersuchung metallischer Werkstoffe mittels SXRR und SXRCT untersucht. Es wird gezeigt, dass der geringere Kontrast, verursacht durch die kleineren Refraktionswinkel, überwunden werden kann. Somit ist die einzig verbleibende Beschränkung die erreichbare Transmission, die alle Röntgenbildgebungsverfahren gemeinsam haben. Darüber hinaus wird ein Modell für die quantitative Auswertung der inneren Oberflächen präsentiert und verifiziert.

Zu diesem Zweck werden vier Fallstudien durchgeführt, wobei jede eine spezifische Herausforderung darstellt. In Fallstudie A werden Risse in einer Probe aus einer Aluminiumschweißnaht untersucht. Diese Fallstudie dient hauptsächlich dazu das Modell für die quantitative Analyse zu verifizieren und die Empfindlichkeit gegenüber Strukturen unterhalb des Auflösungsvermögens zu beweisen. In Fallstudie B wird die Entwicklung der Schädigung in einem aluminiumbasierten partikelverstärktem Metall-Matrix Komposit untersucht. Dabei wird die Genauigkeit und Wiederholbarkeit der SXRR Messungen analysiert und es wird gezeigt das Messfehler kleiner 3 % erreicht werden können. Darüber hinaus wird in Fallstudie B erstmals SXRR in Kombination mit *in-situ* Zugbelastung eingesetzt. Fallstudie C ist aus dem hochaktuellen Bereich der additive Fertigung. Hier wird Porosität in additiv gefertigtem Ti-Al6-V4 analysiert mit besonderem Augenmerk auf der Morphologie der Poren. Es wurde ein Verfahren zur Klassifizierung, basierend auf SXRR Messungen, erfunden, welches Bindefehler und Poren voneinander unterscheiden kann auch wenn die Defekte nicht räumlich aufgelöst werden können. In Fallstudie D wird SXRCT zur Analyse von wasserstoffunterstützter Rissbildung in Stahl angewandt. Wegen der hohen Röntgenschwächung des Stahls muss hier mit 50 keV eine vergleichsweise hohe Photonenenergie genutzt werden. Dadurch zeigen die Daten ein erhöhtes Rauschen und geringeren Kontrast verglichen mit den anderen Fallstudien. Allerdings ist es, trotz der geringeren Datenqualität, möglich das Auftreten von Rissen in Abhängigkeit der Wasserstoffkonzentration und mechanischen Belastung zu untersuchen.

List of abbrevations and symbols

Abbrevation/Symbol	Describtion
BET	Brunauer-Emmet-Teller method for determination of the specific surface by gas adsorption
C	refraction value from synchrotron X-ray refraction imaging techniques
C_{m}	refraction value from X-ray refraction topography
CT	computed tomography
d	X-ray penetration length through the sample, equivalent to sample thickness
DEI	diffraction enhanced imaging
DEI-CT	diffraction enhanced imaging computed tomography
DCM	double-crystal monochromator
DMM	double-multilayer monochromator
ϵ	refraction index decrement
E	photon energy
E_{v}	energy density of the selective laser sintering process
FBP	filtered backprojection
FWHM	full width at half maximum
HAC	hydrogen assisted cracking
I	measured X-ray intensity in general
I_0	X-ray intensity of the free X-ray beam in general
I_{max}	maximum intensity of the analyzer crystal's rocking curve
I_{R}	intensity of refracted X-ray; for X-ray refraction topography
I_{T}	total transmitted X-ray intensity
λ	photon wavelength
MIR	multiple-image radiography
MMC	metal-matrix composite
μ	linear X-ray attenuation coefficient
n	index of refraction
p	porosity
φ	rotation angle of sample in CT measurements
ρ	mass density
ρ_{e}	electron density
SAXS	small angle X-ray scattering
SEM	scanning electron microscopy
LPBF	laser powder bed fusion
SXCT	synchrotron X-ray computed tomography
SXRCT	synchrotron X-ray refraction computed tomography
SXRR	synchrotron X-ray refraction radiography

Abbrevation/Symbol	Describtion
θ	tilt angle of the analyzer crystal
θ_B	Bragg angle of the analyzer crystal
USAXS	ultra small angle X-ray scattering
ξ	specific surface, i.e., surface per unit volume
ζ	ratio of refraction values from 0° and 90° sample orientation

Contents

1 Introduction

The non-destructive evaluation of materials is an important task for the understanding of material properties and production process optimization. In many fields there is a desire to reliably detect and quantify ever smaller defects or features. Driven by this demand the spatial resolution of conventional X-ray radiography and computed tomography (CT) improved significantly with the development of better detectors. In systems using geometric magnification spatial resolutions of few micrometers can be reached and X-ray microscopes or synchrotron beamlines can reach resolutions of several hundred nanometers. However, such resolutions can only be achieved in a relatively small field-of-view ($1\,\mathrm{mm}^2 - 4\,\mathrm{mm}^2$) and for some applications the distribution of sub-micrometer structures in larger scale samples are of interest or the structures of interest are even smaller than the best spatial resolution. For these cases, techniques are of interest which can detect and quantify structures smaller than the spatial resolution of the used imaging system. Furthermore, weakly absorbing materials which produce very low image contrast cannot be properly analyzed with conventional X-ray imaging methods based on absorption contrast.

To address these limitations, methods have been developed over the last decades, which use the refraction of X-rays to enhance image contrast. They are most widely known under the term 'phase-contrast' methods and include propagation-based phase contrast [1], Talbot-Lau interferometry [2], and analyzer-based or diffraction enhanced imaging (DEI) [3]. A review of these methods can be found in [4]. They were proven to be capable of detecting small features which remained invisible with conventional absorption based X-ray imaging methods due to limited spatial resolution.

X-ray refraction or phase-contrast methods have so far only been applied to medical imaging and weakly absorbing materials, like fiber reinforced plastics or light ceramics. Metallic materials have not been investigated apart from one or two showcases, which remained demonstrative. The reason for this is, that metals usually require higher photon energies to yield enough transmission. Higher photon energies, however, lead to smaller refraction angles which make the analysis of the refractive properties of the sample more difficult. Also, the maximum usable photon energy of X-ray sources is limited especially since the X-rays need to be parallel and at least approximately monochromatic.

In this work, two X-ray refraction based imaging methods, namely, synchrotron X-ray refraction radiography (SXRR) and syncrotron X-ray refraction computed tomography (SXRCT) are applied to quantitatively analyze defects in different metallic materials. The aim is to demonstrate that optimization of both methods can overcome the challenges faced when measuring metallic materials and that sub-resolution features of the sample, such as cracks or pores, can be detected with similar quality as for light materials. Further, the suitability of SXRR for *in-situ* measurements is explored and a model is presented and verified which extracts quantitative information about inner surfaces, i.e., the surfaces of cracks or pores as well as interfaces between different phases of the material.

For this purpose, four dedicated case studies are presented in this work. Case study

A focuses on methodological aspects, i.e., to verify the detection of sub-resolution features as well as the presented model and the accuracy of necessary image registration. Case studies B, C and D, in addition to methodological aspects, each have goals with respect to the properties of the investigated materials. Case study B is conducted to gain insights into the evolution of damage in particle reinforced metal-matrix composites under tensile load by using *in-situ* measurements. In case study C porosity in additively manufactured Ti-Al6-V4 is investigated with an emphasis on detecting defects smaller 1 µm while being sensitive to the defect morphology and, thus, enabling further optimization of production parameters. Finally, case study D is performed with the goal to gain insights into the initiation of hydrogen assisted cracking by analyzing the occurance of sub-resolution sized cracks in dependence of hydrogen content and mechanical load.

2 Literature Review

This chapter summarizes the prior art related to the X-ray refraction imaging methods, SXRR and SXRCT, used in this work. The quantitive evaluation of the data is done similarly to X-ray refraction topography to extract the so called refraction value as a measure for the amount of inner surfaces of the sample. Hence, Section 2.1 summarizes the published work around this method. The experimental setup of SXRR and SXRCT is the same as that used for diffraction enhanced imaging (DEI) and the research around DEI is summarized in Section 2.2. However, is must be emphazised that DEI uses a very different analysis for the data focussing on the recovery of refraction angles. The evaluation procedures presented in Section 2.2 should, therefore, not be confused with the evaluation of SXRR and SXRCT. Finally, Section 2.3 summarizes previous materials science applications using SXRR and SXRCT.

2.1 X-Ray Refraction Topography

X-ray refraction topography, as a technique for non-destructive testing, was developed in the 1980s and 1990s at the "Bundesanstalt für Materialforschung und -prüfung (BAM)" in Berlin. Hentschel et al. [5] showed that metal wires, glass fibers, and hard elastic propylene fibers create an oriented scattering signal, which is caused by refraction of the X-rays passing through the cylindrical cross section of the fibers. This behavior is governed by the real part of the index of refraction n which, for X-rays in matter, is smaller than and very close to one. It is usually described using the refraction index decrement ϵ, $\Re(n) = 1 - \epsilon$ with $\epsilon \sim \rho_e \cdot \lambda^2 \approx 10^{-5}$, where ρ_e is the electron density of the material, and λ the X-ray's wavelength [6]. For all materials except hydrogen the electron density can be replaced by the mass density ρ. As a result the refraction angles are very small, on the order of few seconds of arc to few minutes of arc. Therefore, the signals are observed in an angular range smaller than common small angle X-ray scattering (SAXS).

Based on this phenomenon, a method was developed to gain quantitative information about the inner surfaces of a sample from the refraction signal [7, 8]. The measurement requires X-ray radiation of small divergence. Therefore, a Kratky type collimator is used and acceleration voltage and pre-filters are chosen to select only the characteristic radiation of the target material of the X-ray tube (commonly molybdenum, copper, or silver). Two X-ray detectors record i) the total transmitted intensity I_T, and ii) the intensity I_R under a certain refraction angle θ_R. A schematic representation of the experimental setup is shown in Figure 1.

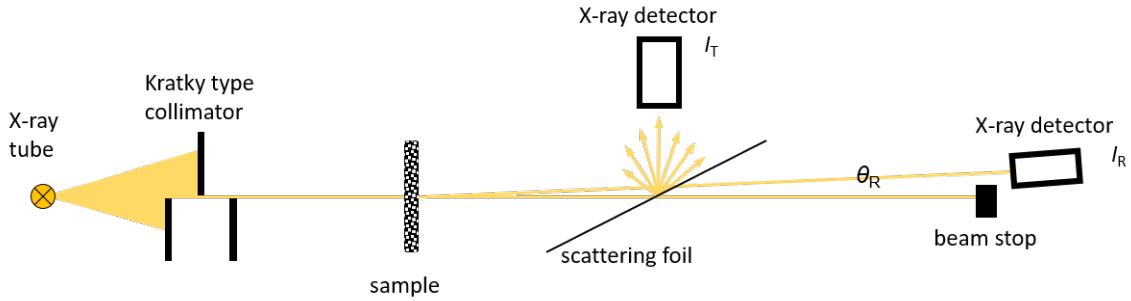

Figure 1: Schematic illustration of the experimental set up for X-ray refraction topography

It was shown [7], that under these conditions the absorption-corrected refraction intensity depends on the interface density within the object and the thickness of the specimen. A refraction value C_m was introduced which can be calculated from the measured absorption and refraction signal.

$$C_m \cdot d = \frac{I_{T0} \cdot I_R}{I_T \cdot I_{R0}} - 1 \tag{1}$$

The subscript 0 refers to the intensities measured without the sample and d represents penetration length, i.e., the sample thickness. The refraction value C_m is proportional to the specific surface (i.e. surface per unit volume) of the sample. The absolute value of the specific surface can be determined with a calibration measurement of a sample of known specific surface [9]. This can be, for example, a mono-disperse powder; the specific surface is then calculated from the powder particel size. The reference sample is ideally composed of the same material as the sample of interest, since the refracted intensity and, therefore, the refraction value depends on the electron density of the material. If the materials are different, the refraction values must be corrected by the squared ratio of the electron densities [9].

The method was then successfully applied to the characterization of porous ceramics and fiber reinforced composites. It was shown, that X-ray refraction topography can detect and quantify fiber debonding, impact damage, and cracking from mechanical loading and aging in various fiber reinforced polymers [10]. In [11, 12], X-ray refraction topography was used to calculate the pore size in ceramic materials, such as SiC or Al_2O_3. A complete analysis of porosity in titania-yttria compounds with X-ray refraction topography and mercury intrusion porosimetry was presented by Tzschichholz et al. [13]. The refraction value was also correlated to the retained strength of carbon fiber reinforced plastics after cyclic loading [11]. More recently Erdmann et al. [14] used X-ray refraction topography to investigate the generation of inner surfaces of diesel-saturated high-desnity polypropylene under tensile load. However, the most important application became the damage assessment in carbon or glass fiber reinforced plastics [15–17].

2.2 Diffraction Enhanced Imaging

In 1996, Chapman et al. [18] published their first paper on using single crystal diffraction and synchrotron radiation to analyze refraction of X-rays. They used a transmission crystal (Laue diffraction geometry) to split the incident synchrotron beam and captured the transmission and refraction image on one image plate. From these two images an absorption map and a map of the deflection angle was calculated.

One year later, the same group published the paper "diffraction enhanced x-ray imaging" [3] in which they lay the foundation of this X-ray imaging technique. Here, they switched from the Laue diffraction geometry to the Bragg geometry using a single crystal to reflect the X-rays onto a 2D detector. This setup is the same as that for SXRR and SXRCT and is depicted in Figure 6 (Section 3.3.1). However, the data analysis of DEI is different from that of SXRR. For DEI, two images of the object at two positions of the analyzer crystal's rocking curve were taken, namely on either side at the half-maximum called high angle and low angle side. From those images, maps of the "apparent absorption" and the refraction angle were calculated using a geometrical optics approximation. The apparent absorption map included also scattering effects that reduce the intensity in the straight transmission direction. Therein lay the major weakness of this method: it ignored a potential broadening of the rocking curve caused by scattering or multiple refraction at small unresolved structures, a phenomenon called "ultra small-angle X-ray scattering (USAXS)" in later publications.

The effect of USAXS was given much attention in the subsequent research on DEI. Wernick et al. [19] presented a method, called "multiple image radiography (MIR)", based on deconvolution of the intrinsic rocking curve and the response of the sample. From the resulting angular intensity spectrum three parametric images were calculated: attenuation (i.e. exponential intensity loss), refraction angle, and USAXS (i.e. variance of the refraction angle). Khelashvili et al. [20] presented a physical interpretation of MIR by solving a radiation transport function and linked the USAXS image to the samples micro-structure below the spatial resolution. Oltulu et al. [21] modeled USAXS as the width of a Gaussian distribution and added an extinction coefficient to create a total of four parametric images. Pagot et al. [22] also applied Gaussian curve fitting to extract USAXS information. These methods require the measurement of the entire rocking curve with at least 20 images. However, an implementation of MIR was presented by Chou et al. [23], which requires fewer images. Rigon et al. [24] defined the refraction angle as a probability density and the response of a single pixel as the integration of this statistical distribution. They used a second-order Taylor's expansion to calculate a map of the square width of the distribution. Based on this, they developed a method they called "generalized diffraction enhaced imaging" [25, 26] to extract apparent absorption, refraction angle, and USAXS with only three images taken at both half-slopes and the peak of the rocking curve using the values of the rocking curve as well as its first and second derivative at these positions. Other ways to improve the original geometrical optics approximation of DEI included a regularization approach [27] and a Fourier optics approach [28].

From a very early point on, DEI was extended to tomographic imaging. Dilmanian et

al. [29] applied standard filtered backprojection (FBP) to the parametric images of DEI, i.e., apparent absorption and refraction angle. For this they recorded three CT scans with a 360°-rotation of the sample; one each at the high and low angle side as well as one at the peak of the rocking curve. They obtained consistent results from which they concluded that FBP is suitable for DEI-CT. Zhu et al. [30] and Sun et al. [31] explored formal requirements for the application of FBP in the case of DEI, namely that the projections must be line integrals and the response of a single point in the sample must be invariant with the rotation angle. Both publications concluded that these are fulfilled as long as the rotation axis of the sample is perpendicular to the rotation axis of the analyzer crystal. When both rotation axes are parallel to each other, the requirement of invariance is broken and FBP can no longer be applied. However, other reconstruction algorithms that can be applied to this geometry were proposed. The same aspects are analyzed for SXRCT in Section 3.3.2 and the respective CT geometries are visualized there in Figure 10. Nesterets et al. [32] performed a similar analysis but included a theoretical assessment of the expected noise in both geometries showing that the setup with the rotation axis of the sample perpendicular to the rotation axis of the analyzer may yield less noisy images. Brankov et al. [33] presented the application of CT to MIR and Majidi et al. [34] investigated the possibility of using limited angle tomography in combination with MIR. Rigon et al. [35] also applied CT to their three-image version of DEI and supplied formal justification for the reconstruction with FBP. Some publications focused on reconstructing not just the parametric images but the index of refraction itself [31, 32, 36, 37]. To reduce experimental effort and dose, Wang et al. [37] proposed a method to gain a reconstruction of the refractive index with only one CT scan over 360° at a fixed analyzer position. They took advantage of the fact that the gradient of the refractive index ∇n at a given point (x, y, z) in the sample at rotation angle φ differs from the gradient at rotation angle $\varphi + \pi$ only by a negative sign. Li et al. [38] also achieved the reconstruction from a single CT scan by means of an iterative reconstruction algorithm.

In summary, the research around DEI focused on simplifying measurement routines, precise calculation of refraction angles, and reconstruction of the refractive index. Practical applications were only investigated in the field of biological and medical imaging. For mammographic imaging, the improved contrast in breast tissue with DEI-CT was demonstrated [39, 40] and even clinical studies were performed, e.g., [41]. Other performed tasks include the imaging of mammal crystalline lenses [42]; cartilage , bone, and soft tissue in mice [43], pig joints [44, 45], human ankles and toes [46]; or kidneys [47]. Nearly all studies used tomographic imaging and demonstrated higher sensitivity to small structures which could improve diagnosis. A review on the medical applications of DEI was published by Bravin et al. [48]. However, applications to materials science or non-destructive testing were not reported.

2.3 Materials science applications of SXRR and SXRCT

SXRR and SXRCT adopt the same basic experimental setup as DEI for the pupose of materials science and non-destructive testing by evaluating the data to gain informa-

tion about the inner surfaces, comparable to the information gained by X-ray refraction topography. First results on characterization of lightweight materials were presented in 2004 [49, 50]. It was shown on the example of a fiber reinforced metal matrix composite that fiber cracking and localized fiber debonding can be visualized in radiogaphic images using an analyzer crystal. The results were compared to absorption radiographs to demonstrate the higher contrast of the damaged regions. Also the feasibility of tomographic imaging was demonstrated. A matrix crack appeared larger in the SXRCT measurement than in the comparing synchrotron X-ray CT (SXCT) measurement. Further, fiber debonding could be visualized three dimensionally with the sample rotated 90° with respect to the scattering plane of the analyzer crystal [51].

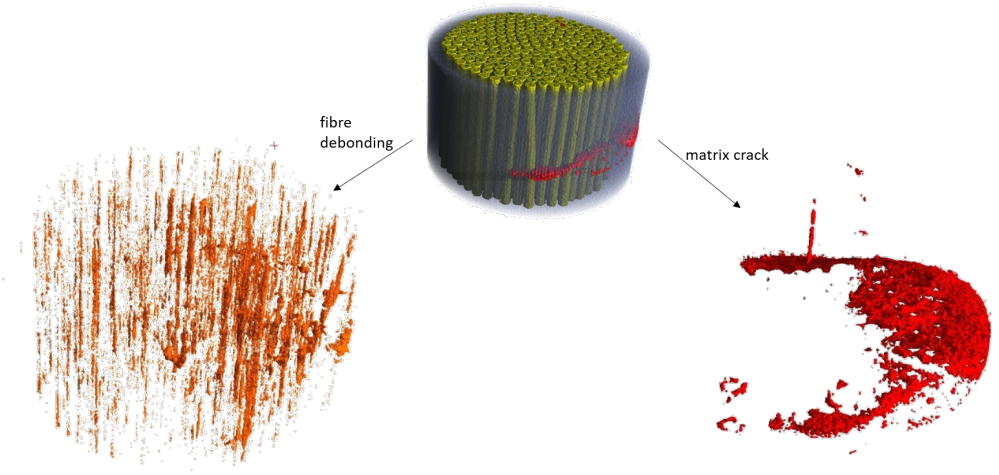

Figure 2: 3D visualization of fibre debonding and matrix crack in a fibre reinforced metal matrix composite; reprint with permission from [51]

In [52] the microstructure of SiC particle-reinforced aluminum with Fe-rich inclusions after fatigue cracking was analyzed with SXCT and SXRCT. The interest lay on the distribution, size, volume fraction, and shape of porosity and the Fe-rich inclusions. While it was pointed out that the two imaging methods are complementary, quantitative measures were only extracted from the SXCT measurement.

More recently, studies were published in which SXRR was used to characterize ceramic materials for diesel particulate filters. Kupsch et al. [53] quantitatively analyzed porosity and pore orientation in Cordierite and Müller et al. [54] investigated stress induced micro cracking in beta-eucryptide. Further, Cabeza et al. [55] investigated the damage accumulation during creep of Al-3.85Mg with SXRR and successfully corroborated the damage mechanism predicted by the solid-state transformation creep model. A good overview of X-ray refraction techniques for materials characterization, including SXRR and SXRCT, can be found in [56].

This work builds on these studies and further extends the application of SXRR and SXRCT towards metallic materials.

3 Synchrotron X-ray imaging techniques

The X-ray imaging experiments for this work have been carried out at the sychrotron radiation beamline "BAMline" at BESSY II operated by Helmotz-Zentrum Berlin für Materialien und Energie. This chapter first describes the general outline of BAMline and then the X-ray imaging techniques used for this work are described. There the focus is on the refraction based imaging techniques SXRR and SXRCT. The absorption based imaging techniques of X-ray radiography and SXCT will only be described briefly as they are mostly used as reference and already well described in published literature [57–61].

3.1 General description of BAMline

The experimental set up for SXRR and SXRCT is part of BAMline [62, 63], a hard X-ray imaging beamline installed at the electron storage ring BESSY II operated by Helmotz-Zentrum Berlin für Materialien und Energie. The photon source is a 7 T wavelength shifter insertion device with a characteristic energy of 13.5 keV for an electron energy of 1.7 GeV. The spectrum emitted by the wavelength shifter is shown in Figure 3 [64] with the maximum of the photon flux density at 11.2 keV and an exponential decrease for higher energies. The photon energy required for the imaging of metallic materials depends on the specific metal and the sample thickness. For the imaging of aluminum samples with thicknesses of few millimeters photon energies of 20 keV to 25 keV are sufficient. This is not so different from the photon energies typically used for light weight ceramics or fiber reinforced plastics, i.e., the established fields for the application of SXRR. In this energy range the photon flux density of the wavelength shifter is between 84 % and 71 % of its maximum value. To image titanium samples with thicknesses of just a few hundred micrometers an photon energy of 30 keV is required, where the photon flux density is reduced to 58 % of its maximum value. At 50 keV, the photon energy required to image steel samples with about 1 mm thickness, the photon flux density is reduced to 21 %. The reduced photon flux density leads to longer exposure times and a lower signal to noise ratio when imaging metallic materials compared to weaker absorbing materials and poses a challenge to the application of SXRR and SXRCT to metallic materials.

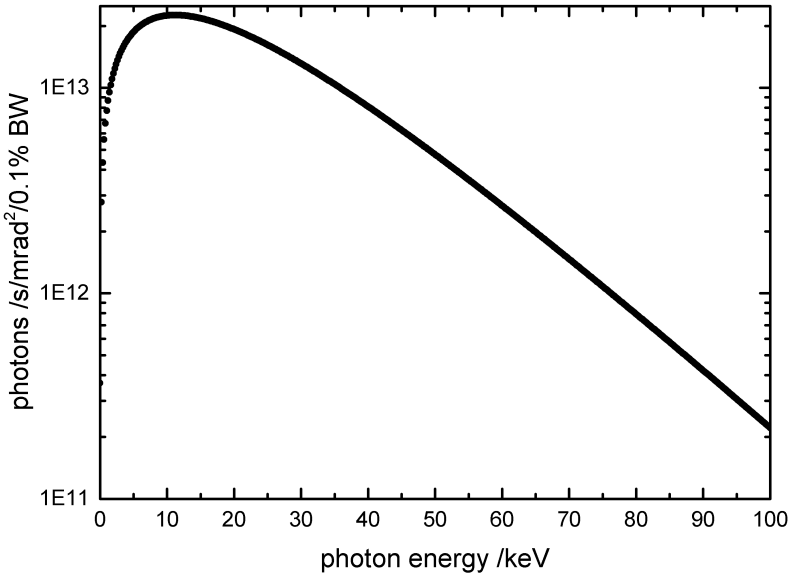

Figure 3: Emitted spectrum of the wavelength shifter at BAMline [64]

Two monochromators are installed at the beamline to select a specific photon energy from the spectrum. These can be used separately or in combination, depending on the measurement task. The first one is a double multi-layer monochromator (DMM) consisting of alternating layers of tungsten (1.2 nm thickness) and silicon (1.68 nm thickness). It provides an energy resolution of $\Delta E/E = 1.7\,\%$ and a divergence of the exiting X-rays of 0.6 mrad. The second one is a Si(111) double crystal monochromator (DCM). Its energy resolution and divergence of the exiting X-rays are $\Delta E/E = 0.14\,\%$ and 0.01 mrad, respectively. Hence, the photon flux density is about 100 times higher for the DMM than for the DCM for a selected photon energy. The layout of the beamline optics is schematically shown in Figure 4.

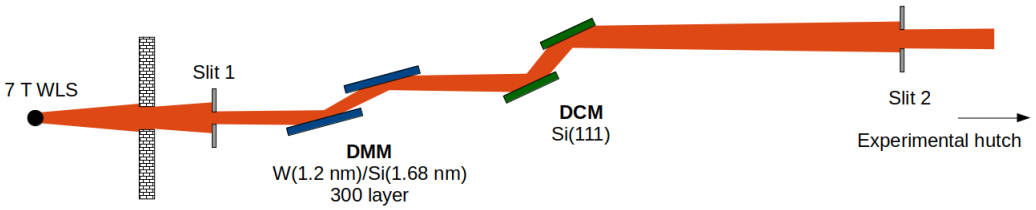

Figure 4: Schematic illustration (side view) of the BAMline optics with double multi-layer monochromator (DMM) and double crystal monochromator (DCM)

SXRR and SXRCT require approximately monoenergetic X-rays of smaller divergence than the observed angles of refraction. While the DMM would provide sufficiently monochromatic X-rays, its divergence is two to ten times larger than typical refraction angles and, thus, too large for SXRR and SXRCT measurements. Therefore, the DCM is used for these experiments. This, however, limits the the maximum usable photon energy to about 50 keV because of the lower photon flux density. Furthermore, the crystals of the DCM are 300 mm long. Therefore, the field-of-view is vertically limited to about 3 mm at 50 keV because of the the small incident angle of the X-rays.

An air filled ionization chamber is installed directly in front of the exit window to the experimental hutch which constantly monitors the photon flux density. Especially when using the DCM the photon flux density at the experiment declines over time, which is critical for long time measurements such as CT scans. This decline is caused by the crystals of the DCM becoming misaligned due to unavoidable thermal drifts and mechanical instabilities. This is compensated for by automatically adjusting the second crystal by means of a piezo actuator, if the photon flux density at the exit window drops below a certain level. Thus, a relative photon flux density above 96 % can be maintained, enabling long time measurements.

3.2 Imaging methods based on absorption contrast

This section describes imaging methods used in the course of this work which are based on the attenuation of X-rays for image contrast. These are used for comparison and to better interpret the results from X-ray refraction imaging methods as they yield complementary information. Also, the respective projection images are required as input for data processing for refraction based imaging methods as described in Section 3.3.

3.2.1 X-ray radiography

X-ray radiography was the first X-ray imaging technique used to investigate the inner structure of an object. Its principle is that the X-rays emitted by the source penetrate the sample and the transmitted X-ray intensity is measured (here by a 2D digital detector). The image contrast is based on the attenuation of the X-rays when passing through the object. The measured intensity I is determined by the incident intensity I_0, the linear attenuation coefficient μ of the material, and the penetration length d through the material according to Beer's law of attenuation.

$$I = I_0 \cdot e^{-\mu \cdot d} \tag{2}$$

The linear attenuation coefficient μ includes all physical interactions of a photon with matter that lead to the photon not reaching the detector, i.e., photoeffect μ_{ph}, coherent μ_{coh} and incoherent μ_{incoh} scattering, and electron-positron pair formation μ_{pair}, all of which depend on the photon energy. However, since monochromatic X-rays are used here this is of no concern other than the choice of photon energy and is, therefore, omitted.

$$\mu = \mu_{\text{ph}} + \mu_{\text{coh}} + \mu_{\text{incoh}} + \mu_{\text{pair}} \tag{3}$$

To create a map of the product $\mu \cdot d$, which represents the local density of the sample at each detector pixel, at least three 2D images are required. One with the object placed in the X-rays path which represents I. A second without the object which represents I_0. And a third with the X-ray source switched off, I_{dark}, which represents the background signal caused by stray light and the electronics of the detector. The image of I_0 is also called the flat-field or gain image and the image of I_{dark} is called the dark-field or offset. $\mu \cdot d$ is then calculated by rearranging Eq. 2 and subtracting the dark-field image from the image of the object and the flat-field image.

$$\mu \cdot d = -\ln\left(\frac{I - I_{dark}}{I_0 - I_{dark}}\right) \tag{4}$$

This map of $\mu \cdot d$ can further be processed to generate a porosity map of the single-phase sample. Porosity is defined as the ratio between the volume of voids V_{void} and the total volume V. X-rays detected by each pixel probe a total volume defined by the pixels area and the sample thickness. As the pixel area is the same in all cases the ratio of the volumes can be replaced by the ratio of the respective lengths of voids and material along the X-rays paths. Figure 5a illustrates the case of a dense material with a linear X-ray attenuation coefficient μ_0. In this case the value of the $\mu \cdot d$ map is equal to $\mu_0 \cdot d$. The case of a porous material with the same linear X-ray attenuation coefficient μ_0 is shown in Figure 5b. Here, the X-rays only pass through the dense material for a path length of $d - l_{void}$. The path length l_{void} through the voids, however, cannot be measured and the value of the $\mu \cdot d$ map is expressed by an effective μ, which is smaller than μ_0. Thus, the porosity p can be expressed by the ratio between the linear X-ray attenuation coefficient μ_0 of the dense material and the linear X-ray attenuation coefficient μ effectively gained from the measurement according to Eq. 5.

$$p = \frac{V_{void}}{V} = \frac{l_{void}}{d} = 1 - \frac{\mu}{\mu_0} \tag{5}$$

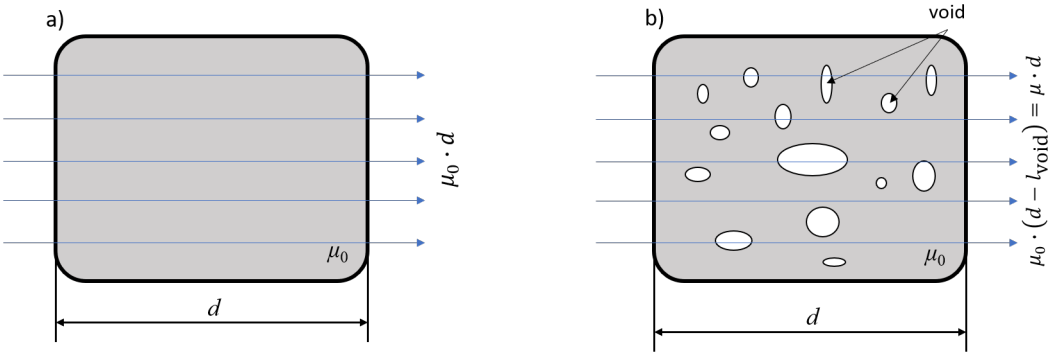

Figure 5: Illustration of the influence of porosity on the measured X-ray attenuation $\mu \cdot d$ in a single-phase material with a linear X-ray attenuation coefficient of μ_0

This approach requires knowledge of the linear X-ray attenuation coefficient of the dense material μ_0, with porosity $p = 0$, and the length of the X-rays path through the sample, which corresponds in a first approximation to the sample thickness. Information about μ_0 can be gained from tabulated data (e.g. [64]) or, if the pores are well resolved in the radiographs, a pore free section of the sample can be used as reference. The accuracy of such a measurement is limited by the uncertainty of the X-rays path length d and the nominal attenuation coefficient μ_0, which might differ from tabulated data for real samples.

3.2.2 Synchrotron X-ray CT

X-ray CT, today, is a well established method for non-destructive evaluation and materials science application. In contrast to radiography it yields true 3D information about the inner structure of an object. The principle of CT is to take radiographs of an object from different views and use this image sequence to reconstruct a 3D representation of the object. The different views are, most commonly, evenly distributed along a 360° or, for parallel X-rays, 180° rotation of the object (circular trajectory). The number of radiographs needed along this trajectory depends on the object size and the resolution of the detector and usually lies between 2000 and 3000. When using synchrotron light sources, it is common practice to record flat-field images, i.e., images of the X-ray beam without sample, at regular intervalls during the scan by moving the object out of the beam. At BAMline this is usually done after every 100 projections.

The projections are first processed to create maps of $\mu \cdot d$ in the same way as for X-ray radiography following Eq. 4. These maps are then supplied to the CT reconstruction. For reconstruction the filtered backprojection algorithm for parallel beam geometry is applied here, which was described in detail by Kak and Slaney [65]. The result is a 3D voxel grid with the spatial distribution of the linear X-ray attenuation coefficient μ which is proportional to the density. Evaluations are done by segmenting different features in the volume according to their density and then analyzing volume fractions, morphology, or orientations of segmented parts or performing dimensional measurements. For detailed information about X-ray CT, its data aquisition, image processing, reconstruction algorithms, and analysis the reader is refered to an abundance of published literature, e.g., [57–61, 65].

The use of synchrotron radiation offers several advantages over conventional X-ray sources. Most importantly the X-rays from synchrotron sources are nearly parallel so that there is no geometric unshapress originating from the source spot. Therefore, the spatial resolution is only limited by the resolution of the detector. Thus, resolutions of only a few hundred nanometers can be achieved, while conventional X-ray CT systems achieve resolutions of few micrometers which is approximately the size of the focal spot on the target of the X-ray tube. Further, the higher photon flux density allows the use of monochromatic X-rays. Together with the small divergence this avoids many imaging artifacts, such as cone beam or beam hardening artifacts. However, SXCT is more prone to so called ring artifacts which appear as concentrical circles around the center of rotation in the volume data. These arise when pixels have a systematic offset.

Because this offset is stationary in all projections it causes the circular artifact around the center of rotation. In conventional X-ray CT systems these artifacts are avoided by a so called "bad pixel map" which is a map of all pixels with systematic offset. The read out of these pixels is ignored and their values interpolated from neighbouring pixels. Such a correction, however, is much harder in case of a synchrotron light source due to two reasons. First, the "bad pixels" are not necessarily stationary for all measurements at all times. This is because the origin of the pixels offset can not only be a defect of the CCD of the detector but also scratches or other damage on the scintilator screen or the monochromator. Therefore, as theses optical elements are moved against each other, e.g., when selecting a different photon energy, the position of the defect pixels shift. Second, "bad pixels" in SXCT are often not isolated pixel but areas of hundreds of pixels or more. This makes the interpolation less reliable. Thus, it is often not feasible to remove these ring artifacts as projections would need to be filtered so heavily that features of the sample might be removed as well.

3.3 Imaging methods based on refraction contrast

The following section describes the X-ray refraction imaging methods, namely SXRR and SXRCT, which are in the focus of this work. The evaluation in both cases aims at providing the same type of information as X-ray refraction topography (see Section 2.1), which is to detect and quantify inner surfaces. However, different calculations are required due to the different experimental setup.

3.3.1 Synchrotron X-ray refraction radiography

Experimental setup

As already stated earlier, SXRR adopts the imaging setup of DEI as shown in Figure 6. The key part is an analyzer crystal placed between sample and detector, which reflects the transmitted X-rays into the detector unit. The analyzer crystal is made of silicon cut symmetrically in (111) orientation to match the crystals of the DCM. The detector unit consists of a $CdWO_4$ scintillator screen, a photographic objective, and a CCD camera (effective pixel size $(3.5\,\mu m)^2$).

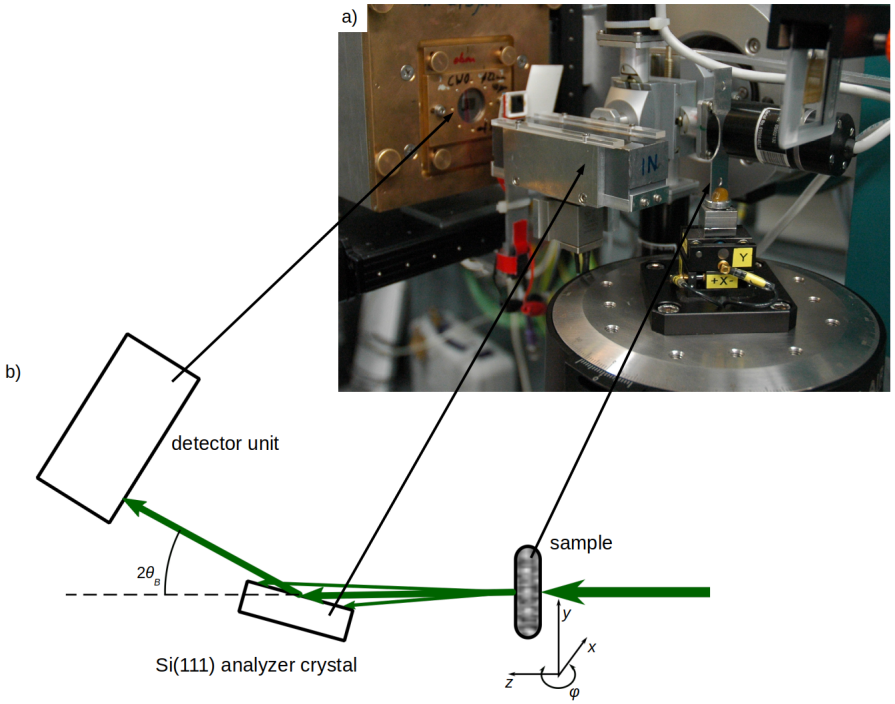

Figure 6: Experimental setup for SXRR; a) photograph of the SXRR setup installed at BAMline; b) schematic representation of the SXRR setup

Sample, analyzer crystal, and detector are arranged in the Bragg diffraction geometry (see Figure 6) and, therefore, only X-rays impinging on the analyzer crystal with an incident angle equal to the Bragg angle θ_B are reflected; all other X-rays are rejected. In this way the analyzer crystal acts as an angular filter for the X-rays. This effect, however, is only observed within the scattering plane of the crystal. The scattering plane is created by the normal vector of the crystal surface and the optical axis as shown in Figure 7. Therefore, the measurement is sensitive to the orientation of the inner surfaces of the sample. Only surfaces whose surface normals have a significant component within the scattering plane and perpendicular to the optical axis can be detected. Own experimental evidence shows that surfaces with a surface normal tilted by $\pm 45°$ with respect to the y-axis (as shown in Figure 6) can be detected. Thus, two measurements with the sample rotated by 90° are sufficient to detect all surfaces.

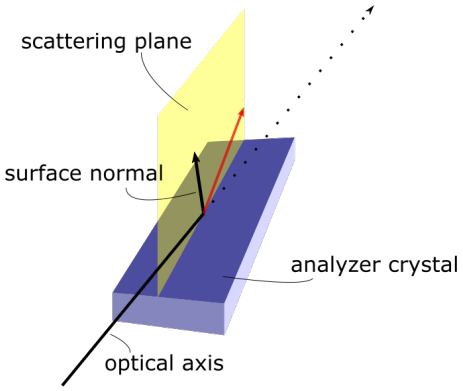

Figure 7: Sketch of the analyzer crystal's scattering plane created by surface normal and optical axis

The central element of SXRR is scanning the so-called rocking curve of the analyzer crystal. The rocking curve is a well known X-ray diffraction measurement for crystallographic analysis. It is measured by adjusting the X-ray source, the crystal, and the detector to the proper Bragg condition. Then the crystal is rocked in a narrow range around the Bragg angle θ_B for the reflex under investigation while detector and source remain fixed. The resulting plot of intensity vs. the crystal's tilt angle θ reveals broadening of the reflex caused by, e.g., mosaicity, strain, or limited layer thickness of the crystal. In contrast to this classical use of the rocking curve, in SXRR, it is not used to analyze a crystal but the incident X-rays. The crystal is a silicon single crystal and, therefore, deviations from the ideal reflex, such as shifts or broadening, must be attributed to the characteristics of the X-rays incident onto the analyzer crystal.

Examples of rocking curves, measured at BAMline, of the Si(111) reflex at 30 keV are shown in Figure 8. The respective data was acquired from samples of case study C. The rocking curve of the free photon beam, i.e., without any object, is marked by red squares. The effect of a purely attenuating sample on the rocking curve is shown by the rocking curve marked by gray triangles; the intensity at every angular position is reduced but the full-width at half-maximum (FWHM) remains the same. The last rocking curve, marked by blue circles, shows the effect of an attenuating and refracting sample. Here, not only the intensity is reduced but also the FWHM is increased. Note

that the attenuation for the blue and gray rocking curves is the same, i.e., both have the same integral intensity.

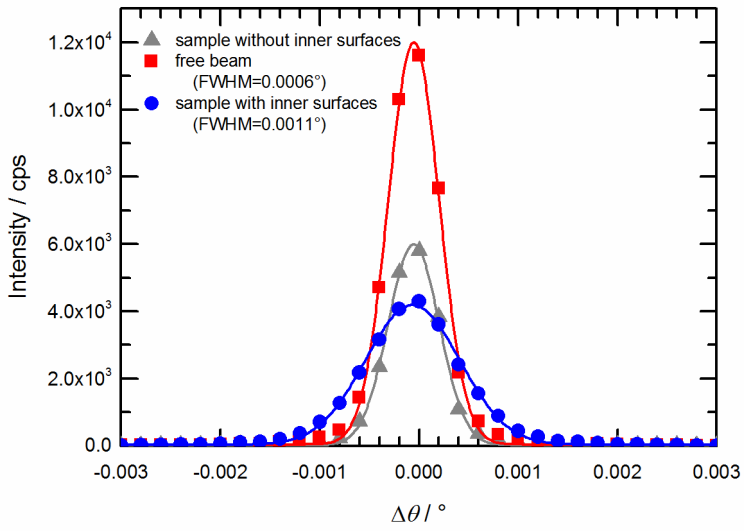

Figure 8: Examples of rocking curves; red squares: rocking curve of the incident beam without sample, gray triangles: rocking curve of a sample without inner surfaces showing the effect of pure attenuation, blue circles: rocking of sample with inner surfaces showing the combined effects of attenuation and refraction

Computation of refraction value for synchrotron measurements

In SXRR the refracted X-rays are discriminated differently than in X-ray refraction topography. In X-ray refraction topography, on the one hand, the X-rays are discriminated by a beam stop blocking the direct beam what corresponds to a spatial discrimination. The analyzer crystal used for SXRR, on the other hand, creates an angular discrimination. That is the X-ray are analysed according to their propagation direction and not by their position on the image plane. Therefore, a different approach for the calculation of the refraction value is required. Figure 8 demonstrates, that the maximum of the rocking curve is reduced more strongly than the integral of the rocking curve if inner surfaces are present in the sample. The reason for this is, that refraction only redistributes intensity from the center of the rocking curve to its flanks. A straightforward way to describe this additional loss at the maximum of the rocking curve is to add the refraction value C as another component to the attenuation coefficient in Eq. 3. Thus, the intensity at the maximum of the rocking curve $I_{\max}$ can be expressed by Eq. 6.

$$I_{\max} = \max I(\theta) = \max(I_0(\theta) \cdot e^{-(\mu+C)\cdot d}) = I_{\max,0} \cdot e^{-(\mu+C)\cdot d} \tag{6}$$

The integrated intensity of the rocking curve is only affected by pure attenuation and can, therefore, be expressed equivalently to Eq. 2.

$$I_{\mathrm{T}} = \int I(\theta) d\theta = \int I_0(\theta) \cdot e^{-\mu \cdot d} d\theta = I_{\mathrm{T},0} \cdot e^{-\mu \cdot d} \tag{7}$$

Dividing Eq. 6 by Eq. 7 eliminates the linear attenuation coefficient μ.

$$\frac{I_{\max}}{I_{\mathrm{T}}} = \frac{I_{\max,0}}{I_{\mathrm{T},0}} \cdot e^{-C \cdot d} \tag{8}$$

Solving for the exponent $C \cdot d$ yields Eq. 9.

$$C \cdot d = -\ln\left(\frac{I_{\max} \cdot I_{\mathrm{T},0}}{I_{\mathrm{T}} \cdot I_{\max,0}}\right) \tag{9}$$

$C \cdot d$ can be approximated by using only the first term of the series expansion of the logarithm to yield a similar expression as the definition of $C_{\mathrm{m}} \cdot d$ in Eq. 1.

$$C \cdot d \approx 1 - \frac{I_{\max} \cdot I_{\mathrm{T},0}}{I_{\mathrm{T}} \cdot I_{\max,0}} \tag{10}$$

The difference between the approximation and the exact logarithm is shown exemplary on a measurement of paper performed at BAMline. One sheet of paper was folded several times to create samples with two, four, and eight layers of the same material. The results presented in Figure 9 show that a significant difference , i.e., larger than the standard deviation, between logarithm and approximation occurs at 8 layers of paper. The corresponding refraction values of $C \cdot d = 0.1311$ and $C \cdot d = 0.1229$, respectively, are already quite high. $C \cdot d$ values observed in regular samples are usually one order of magnitude smaller. Thus, the approximation usually yields valid results.

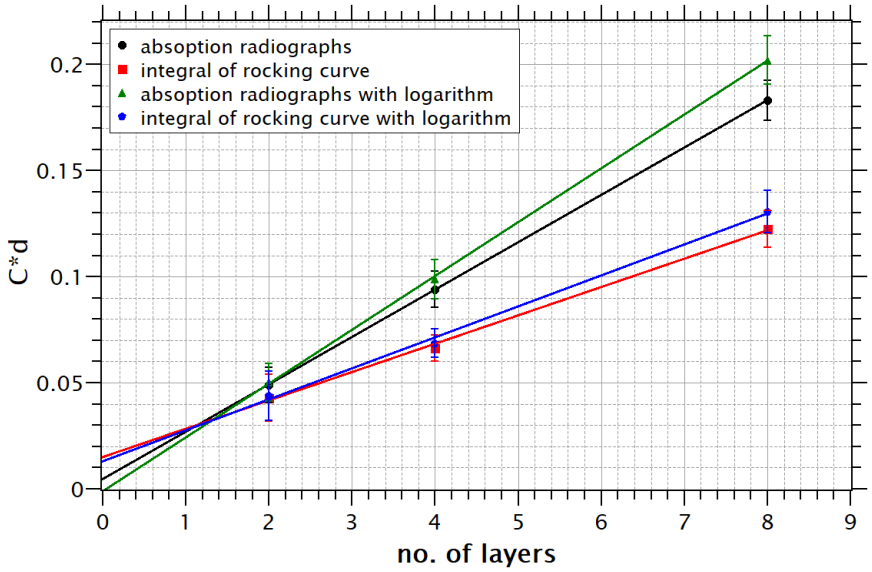

Figure 9: Refraction value $C \cdot d$ of different number of layers of paper; blue pentagons: calculation using the logarithm (Eq. 9) and I_T from the rocking curve, red squares: calculation using the approximation (Eq. 10) and I_T from the rocking curve, Black circles: calculation using the approximation (Eq. 10) and I_T from radiographs, green triangles: calculation using the logarithm (Eq. 9) and I_T from radiographs; Error bars indicate standard deviation over sample area

Figure 9 also compares results for $C \cdot d$ gained with two different approaches to determine the transmitted intensity I_T. In the first, I_T is gained from the rocking curve and, in the second, from absoption radiographs taken without the analyzer crystal. It is observed that the linear fits do not intersect the y-axis at the origin when I_T is gained from the rocking curve. This is caused by the sampling of the rocking curve. In practice, I_T is not calculated as an integral but as the sum of the sampled points of the rocking curve and, therefore, is systematically underestimated. Calculating I_T from actual radiographs can avoid this error as can be recognized from the black and green graphs in Figure 9. However, this requires the radiograph to be registered to the image at the maximum of the rocking curve. This process can lead to errors from inaccuracies of the registration. Alternatively, a Gaussian distribution could be fitted to the sampled points of the rocking curve to calculate the integral intensity. This, however, is computationally extensive as the fit needs to be performed for each detector pixel. Since the refraction value is a relative measure for the inner surface density and real samples compared to each other show relatively small differences compared to the data shown in Figure 9, the error from the underestimated I_T is usually negligible. Thus, for practical purpose, the approach of using the sum of the sampled points is applied.

The quantity $C \cdot d$ still includes the penetration length, i.e., the thickness of the sample, and artifacts arise from slight thickness variations. To avoid such artifacts the quantity $\frac{C}{\mu}$ is calculated as $\frac{C \cdot d}{\mu \cdot d}$, which is independent on the sample thickness.

Furthermore, it should be noted that the absolute value of C from SXRR measurements differs significantly from C_m from X-ray refraction topography (Eq. 1); for the paper samples C_m ranges between 0.5 and 2. Because of the different data acquisition and calculation the two values are not equivalent, however, as relative measures they describe the same effects and yield the same quantitative information. But absolute information about the inner surfaces can only be given relative to a selected reference.

Calibration of the refraction value

An absolute value of the inner surface density or specific surface area ξ ($[\xi] = \frac{m^2}{m^3}$ or $[\xi] = \frac{m^2}{g}$) is gained from C by means of a calibration measurement. This requires the measurement of a sample with known specific surface area. This can, for example, be a monodisperse powder with spherical particles, where the specific surface area is calculated theoretically or a porous sample where the specific surface area was measured by a reference method, e.g, gas adsorption. The latter is based on measuring volumetrically the amount of adsorbed gas (usually nitrogen, argon, or krypton) in dependence of the pressure to gain isotherms. The Brunauer-Emmet-Teller (BET) method is the standard practice to calculate the surface area from these isotherms. BET calculates the amount of molecules in a monolayer of the adsorbed gas and then the total surface area by using the average area occupied by one adsorbed molecule [66].

Since the C depends on the electron density of the material [5], samples and reference sample should ideally consist of the same material. If this is not possible the relation between the refraction values of materials with different electron densities ρ_e is given by Eq. 11.

$$\frac{C_1}{C_2} = \left(\frac{\rho_{e1}}{\rho_{e2}}\right)^2 \tag{11}$$

The electron density can be replaced with the mass density for all materials except hydrogen.

If the specific surface area of the reference sample ξ_r and the corresponding refraction value C_r are known, the specific surface area ξ of a sample with refraction value C is then given by the following simple relation.

$$\xi = C \cdot \frac{\xi_r}{C_r} \tag{12}$$

3.3.2 Synchrotron X-ray refraction computed tomography

The SXRR imaging technique can also be extended to tomographic imaging with the goal to gain true 3D information about the inner surfaces of the sample. The principle is the same as for SXCT, i.e., to record multiple (~2000) SXRR radiographs of the object from different views along a circular trajectory and apply FBP to reconstruct a 3D representation of the the refraction value C.

To successfully apply the FBP algorithm the projection data must fulfill basic requirements. As already stated in Section 2.2 the projections must represent line integrals of

the quantity to be reconstructed along the X-rays path and the response of each volume element must be invariant with the rotation angle of the sample.

The first condition is already proven in Section 3.3.1. Figure 9 shows that the value $C \cdot d$ measured in the projections increases linearly when layers of identical refraction value C are added. Thus, the final value of $C \cdot d$ can be expressed as the sum $\sum_i C_i \cdot d_i$ of all layers i. With infinitesimal layer thicknesses it follows the definition as integral.

$$[C \cdot d]_\varphi (u, v) = \int_{(\varphi,u,v)line} C(x, y, z) ds \tag{13}$$

Here, $[C \cdot d]$ denotes the value of the projection at detector coordinate (u, v) and rotation angle φ of the sample. Using a delta function this could be rewritten as the Radon transform of $C(x, y, z)$.

To analyze the second condition the orientation dependency of the SXRR measurement must be recalled. The analyzer crystal is only sensitive to inner surfaces whose surface normal has a significant component within the scattering plane and perpendicular to the optical axis. The condition of invariance is satisfied if this component does not change during the sample rotation as it is the crucial geometrical parameter influencing the measured refraction value. In Figure 10 two configurations are illustrated. Figure 10a shows the rotation axis perpendicular to the scattering plane of the analyzer crystal. In this setup the previously described component of the surface normals will change with the samples rotation and, thus, the condition of invariance is not satisfied. In Figure 10b the rotation axis lays within the scattering plane of the crystal and is perpendicular to the optical axis. Here the condition of invariance is satisfied.

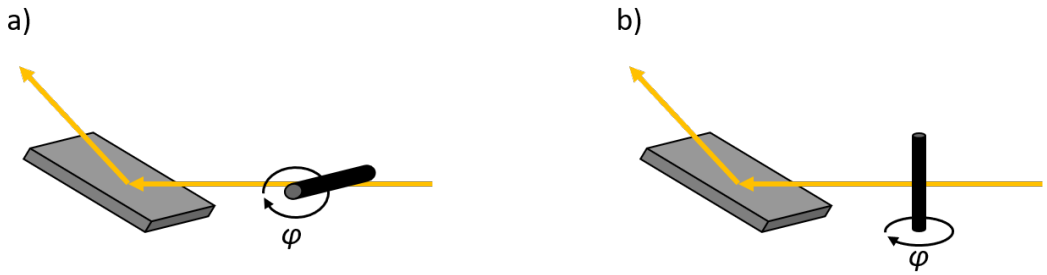

Figure 10: Illustration of orientations of the samples rotation axis with respect to the analyzer crystal; a) rotation axis lays perpendicular to scattering plane and condition of invariance is not satisfied; b) rotation axis lays within the scattering plane and the condition of invariance is satisfied

For the imaging system used at BAMline about 2000 SXRR projections are needed for the reconstruction. As each projection would need to be processed as described in Section 3.3.1 a rocking curve would have to be recorded at each of the 2000 angular positions of the sample. This, however, is not practical because it would result in scanning times of several days. Therefore, a different scanning strategy is needed.

Regarding the definition of the refraction value C in Eq. 10 only two intensities are actually required for the calculation; the maximum $I_{\max}$ and the integral I_{T} of the rocking curve. $I_{\max}$, on the one hand, is usually gained from fitting a peak to the sampled rocking curve but it can just as well be gained directly from one measurement taken at the maximum of the rocking curve. For this purpose, the analyzer is adjusted to the maximum of the rocking curve of the X-ray beam without sample and the scan is performed with the analyzer crystal remaining fixed at this position. This assumes that the sample does not cause the rocking curve to shift its position. This scan is referred to as SXRCT scan. I_{T}, on the other hand, is identical to the total transmitted intensity which can be gained from a measurement without the analyzer crystal. This scan is referred to as SXCT scan. Thus, only two CT scans can yield all information needed to reconstruct the refraction value C; one with the analyzer crystal tuned to the maximum of the rocking curve and one without the analyzer crystal. Both scans can then be processed together according to Eq. 10 to compute projections representing $C \cdot d$ which can in turn be reconstructed using FBP to gain a 3D representation of C. In practice, however, this procedure is met by two major challenges.

First, the analyzer crystal must remain stable at the maximum of the rocking curve during the entire SXRCT scan. Depending on the required exposure time a scan can last one to four hours and unavoidable mechanical instabilities and thermal drifts will cause the analyzer crystal to become dejusted from the maximum during that time span. Therefore, the photon flux is monitored regularly during the scan by means of a photo diode. Every time before a new flat-field is measured, i.e., every 50 to 100 projections, the photo diode is moved into the X-rays path and the photon flux is measured. If it drops below a specified level (usually 96 %) of its starting value the analyzer crystal is readjusted by means of a piezo actuator. Thus, the analyzer crystal remains sufficiently close to the maximum of the rocking curve during the entire scan.

Second, the two CT scans are performed with different beamline optics, i.e., with and without the analyzer crystal. Therefore, there exists a non-rigid transformation between the images. Non-rigid means that the images are not only translated and rotated with respect to each other but also scaled differently, i.e., stretched or compressed. Translation and rotation are caused by misalignments of the analyzer crystal which cannot be avoided completely, while scaling is caused by the cut of the analyzer crystal, which is never perfect along the (111) lattice planes. The registration is further complicated by the different modalities of the images. This means, that the same feature of the sample appears differently in the two images. Therefore, especially on less structured objects, automatic registration tools do not work reliably. Consequently, the transformation between the images is determined on a reference sample. As reference sample a brass grid was chosen which covered the whole image. To distinguish mirrored images of the grid its symmetry was broken by adding a cross of brass wires positioned off the center of the grid. Two images of the reference sample are taken: the first before the beginning of the SXRCT scan with the analyzer crystal in the X-ray beam and the second after the SXCT scan without the analyzer crystal. The registration process was performed using the ImageJ plugin bUnwarpJ [67, 68]. First, the two images of the brass grid are registered to each other and the respective transformations are stored. bUnwarpJ stores

the transformation in both directions. One of these transformation is then applied to all projections of the respective CT scan to register both scans to each other. This, of course, assumes that the transformation remains constant for all projections of the CT scans.

The so registered projections are then processed to create projections of $C \cdot d$ which are reconstructed using FBP to gain the 3D distribution of C. For quantitative analyses the volume data is segmented using thresholding methods and volume measurements, counting defects, or gray value analyses are performed on the segmented data. The different process steps of an SXRCT measurement are visualized in Figure 11.

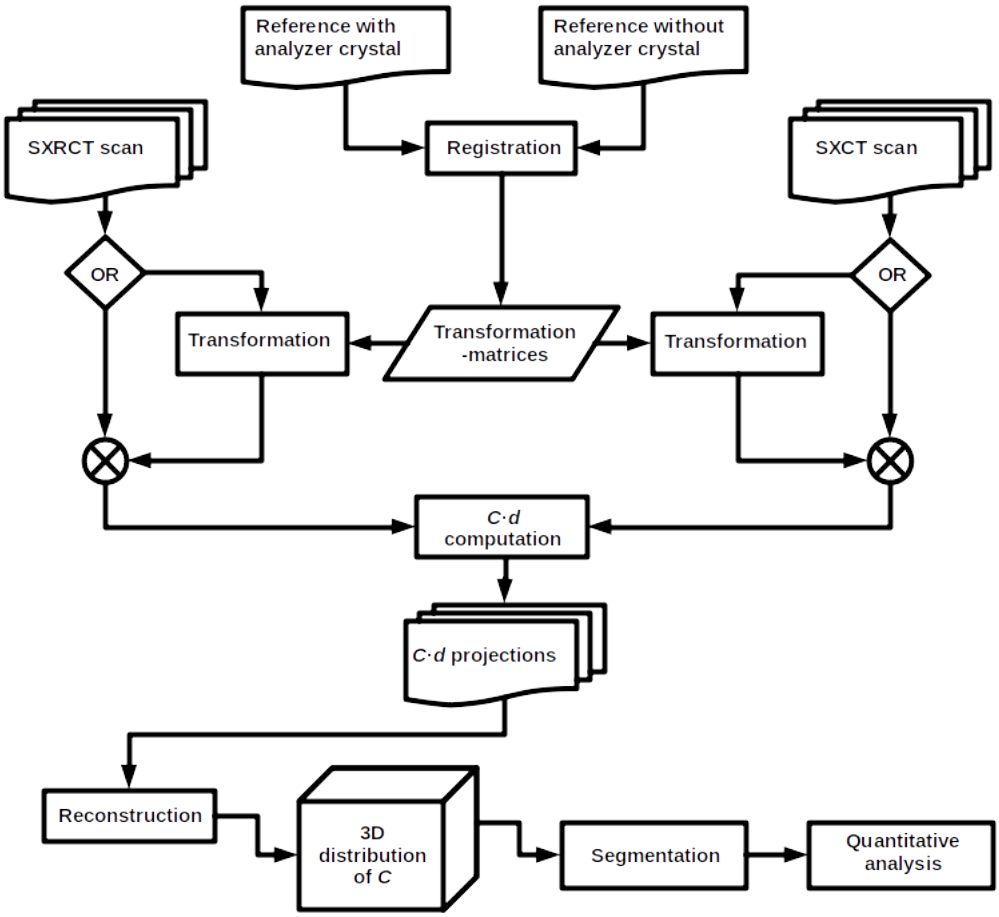

Figure 11: Flow chart visualizing the process tree of a SXRCT measurement; only one of the two scans is transformed and the computation of $C \cdot d$ is performed according to Eq. 10

The SXRCT scan can also be processed on its own following the standard SXCT processing chain, i.e., processing the projections according to Eq. 4 before reconstruction. From Eq. 6 it follows that the result of this procedure is the 3D distribution of the quan-

tity $C + \mu$ as the SXRCT scan represents a measurement of $I_{\max}$. This procedure is simpler as it avoids the image registration and is sufficient for some application, since it allows the segmentation and subsequent volumetric analysis of defects. However, without further knowledge of the sample it can not be distinguished whether a high $C + \mu$ signal is caused by high attenuation, high refraction, or a combination of both. Therefore, the procedure described before is preferable, especially in the case of multi-phase materials.

4 Case studies for the application of X-ray refraction techniques to metallic materials

SXRR and SXRCT as presented in the previous sections are applied in this chapter. In four case studies, the possibilities of these techniques to characterize metallic materials are shown. Each case poses a unique challenge to the imaging task. They cover materials of different X-ray attenuation strength, i.e., aluminum (case studies A and B), titanium (case study C), and steel (case study D); composite materials (case study B); measurements under *in-situ* tensile loading (case studies B); and different aspects of quantitative evaluation are discussed.

4.1 Case Study A: Crack detection in aluminum weld seam

In this case study SXRR and SXRCT are used to investigate cracks in an aluminum weld seam and demonstrate the possibility to detect small cracks of sub-resolution size in light weight metallic materials. The case study was performed in collaboration with Department 9.4 Weld Mechanics and 9.3 Weld Technology of the "Bundesnastalt für Materialforschung und -prüfung". The collegues of Department 9.3 provided the welded plates and the collegues of Department 9.4 prepared the sample from the weld seam. who prepared the sample from the weld seam. SXRR, SXRCT, and SXCT measurements as well as all subsequent evaluations were done by the author. Results of this case study are published in [69].

4.1.1 Motivation

This case study was performed to verify the crack detection capabilities of SXRR and SXRCT. Aluminum was chosen as sample material because it offers the lowest X-ray attenuation coefficient of all metals commonly used as structural material. Thus, relatively low photon energies of about 20 keV to 25 keV, depending on the thickness of the sample, can be used for the imaging. These are not much higher than the photon energies used for light weight ceramics or fiber reinforced plastics for which SXRR and X-ray refraction topography have been developed and are typically applied to. For comparison, X-ray refraction topography typically uses the characteristic K_α radiation of Molybdenum or Silver, which are at 17.48 keV and 22.16 keV, respectively. Therefore, a similar image contrast and crack detection capability is expected.

The aim is to prove that the refraction based imaging techniques SXRR and SXRCT are capable of detecting fine cracks which are not detected by their respective absorption based imaging techniques X-ray radiography and SXCT given the same spatial resolution. Furthermore, in this case study the reconstruction of the refraction value C as described in Section 3.3.2 is performed for the first time and, therefore, the precision of the registration process described in Section 3.3.2 is yet untested. Especially the assumption that the transformation is constant for all projections is critical as the monochromator and analyzer crystals are readjusted several times during the scan. Also, the model for calculation of the refraction value C for synchrotron applications

as presented in Section 3.3.1 has not been verified experimentally. These two aspects are investigated by quantitatively comparing the reconstructions from the original projections and from the $C \cdot d$ projections. It wil be shown that the registration is sufficiently precise and that the model for the refraction value holds.

4.1.2 Welding Test and X-ray imaging

For the case study a sample from an aluminum weld seam containing a substantial amount of cracks was prepared and investigated. The welding test was performed on 6 mm thick plates made from aluminum alloy EN AW - 6060 (AlMgSi0.5). The chemical composition of the material is given in Table 1.

Table 1: Chemical composition of sample A1 according to DIN EN 573-3 in wt%

Si	Fe	Cu	Mn	Mg	Cr	Zn	Ti	Al
0.3 -0.6	0.1 - 0.3	0.1	0.1	0.35 - 0.6	0.05	0.15	0.1	Balance

The plates were welded using a 4.4 kW Nd:YAG laser with a focal distance of 200 mm. At a welding speed of 0.5 m min^{-1} a butt joint (I-shaped seam) without filler material was produced. The shielding gas (industrial grade argon) was supplied to the rear side of the weld pool. These parameters produced a weld seam which contains a significant amount of cracking. Sample A1 is a coupon of about 6 mm $\times$ 5 mm $\times$ 13 mm, which was cut from the weld seam for subsequent imaging. The geometry of the plates and weld seam as well as the position of the coupon, i.e., sample A1, are depicted in Figure 12.

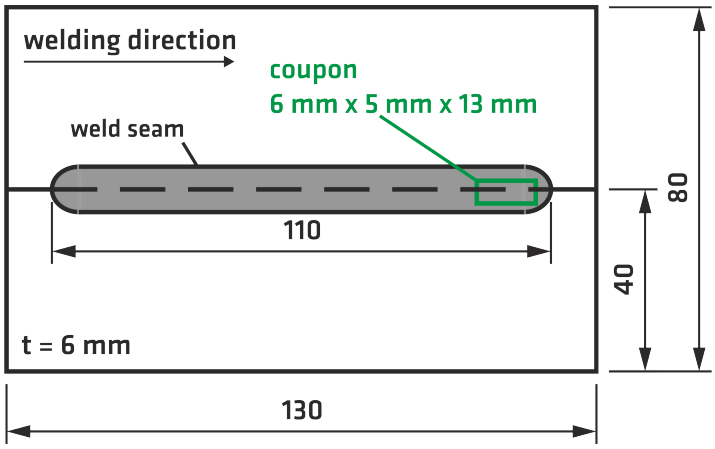

Figure 12: Geometry of plates and position of weld seam with sample A1 being the coupon marked in green; all measures are in mm

All X-ray measurements were performed at a photon energy of 25 keV using a 2048 $\times$ 2048 pixel detector with a nominal pixel size of $(3.5\,\mu\text{m})^2$. The rocking curve was

recorded as described in Section 3.3.1 with 41 exposures with 0.0001° intervals resulting in a scanned range of $-0.002°$ to 0.002° relative to the Bragg angle. The data were evaluated to obtain a map of $\frac{C}{\mu}$. Additionally, an X-ray radiograph of the coupon was taken as described in Section 3.2.1 and a map of $\mu \cdot d$ was calculated for comparison. The SXRCT measurement was performed according to Section 3.2.2. The recorded projections were then processed in two ways. First, they were reconstructed directly with the standard CT processing chain, i.e., the projections were first processed according to Eq. 4 creating projections of $(C + \mu) \cdot d$ (see Eq. 6) which are then reconstructed by filtered backprojection. Second, they were processed together with projections from a subsequent SXCT measurement to calculate projections of $C \cdot d$, which were then reconstructed by filtered backprojection. The SXCT measurement was performed with the same camera system as the SXRCT measurement and has the same spatial resolution. The SXCT data were also reconstructed and all three reconstructed volumes are compared. The reconstructions were performed using the custom filtered backprojection software of BAM.

4.1.3 Results and discussion

The X-ray radiograph and the SXRR radiograph of sample A1 are shown in Figure 13a and b, respectively. The SXRR radiograph represents $\frac{C}{\mu}$, which is proportional to the specific surface, and, therefore, cracks appear as bright areas. In the X-ray radiograph, representing $\mu \cdot d$, the cracks appear as dark areas. A qualitative comparison of both radiographs reveals several cracks, which are clearly visible in the SXRR radiograph, but cannot be recognized in the X-ray radiograph. Some of these are highlighted by red arrows. Also, in the SXRR radiograph, the orientation dependency of SXRR imaging technique can be observed. Of the large pore on the left hand side of the sample (circled in magenta) only the horizontally oriented edges at the top and bottom of the pore are visible since only they cause refraction within the scattering plane of the analyzer crystal. The vertically oriented edges at the left and right are invisible. The transition from visible and invisible parts of the pore's circumference is roughly at 45°, corroborating the statement about the orientational acceptance of the analyzer crystal made in Section 3.3.1.

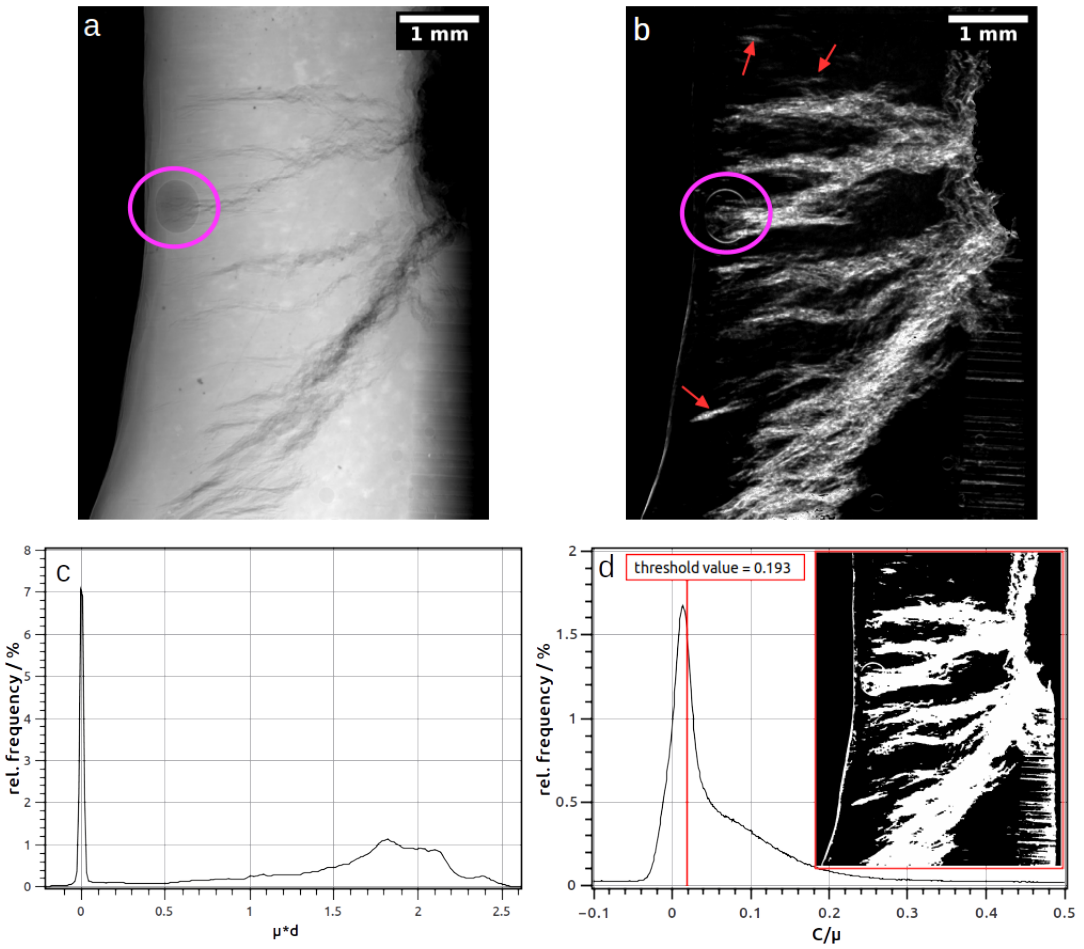

Figure 13: X-ray radiograph ($\mu \cdot d$) (a) and SXRR radiograph ($\frac{C}{\mu}$) (b) of the coupon with respective gray value histogramms (c and d); inset shows result of the thresholding; red arrows indicate fine cracks detected with SXRR but not with X-ray radiography; large pore referred to for illustration of orientation dependency is circled in magenta

The respective histograms of the transmission and SXRR radiographs are shown in Figure 13c and d. Negative values for $\mu \cdot d$ and $\frac{C}{\mu}$ are caused by noise and are physically meaningless. However, they are included in the histograms to show the whole shape of the background peak. In the histogram of the X-ray radiograph (Figure 13c) the background and material peaks can be discerned. This makes it easy to segment the sample as a whole. However, any cracks have values of $\mu \cdot d$ within the broad complex shaped material peak. This makes it impossible to segment the cracks by a global threshold. The histogram of the SXRR radiograph (Figure 13d) shows the background peak with a distinct shoulder, which contains the values of $\frac{C}{\mu}$ of the cracks. Such a histogram is typical for SXRR radiographs. Although there is an apparent overlap between the back-

ground and the signal, the cracks can be segmented by a global threshold. For example, using the Huang thresholding method [70] yields a threshold value of $\frac{C}{\mu} = 0.193$ which is marked in the histogram (Figure 13d). The result of this threshold is presented as binary mask in the inset of Figure 13d. Comparing this binary mask with the actual SXRR radiographs shows that all cracks are segmented. However, some of the segmented areas appear to be noise particles and not actual cracks. This is to be expected as the two peaks in the histogram of the SXRR radiograph (Figure 13d) overlap. The segmentation can impact quantitative measures, e.g., the average value of $\frac{C}{\mu}$, by up to 15 % depending on the chosen threshold and post-processing. This is still acceptable considering the simplicity of the segmentation by global thresholding and that a projection of a complex shaped sample with inhomogeneous thickness is regarded.

Figure 14 presents tomograms (slices of the 3D reconsrtuction) of the reconstructed volumes from the SXCT and SXRCT measurements taken from the same location within the sample. Figure 14a shows the SXCT tomogram. Here, the gray value of the image represents μ and cracks appear as dark areas. The edges of the cracks appear brighter because of propagation-based phase contrast. The measurement was performed with a distance between sample and detector of 180 mm, which is enough create a phase contrast effect. Actual propagation-based phase contrast measurements are performed at larger distances , e.g. in [1] a distance of 820 mm is used. However, for holotomography, where the sample is measured at different sample-detector distances, 180 mm is about the smallest distance used within a measurement series [71]. Figure 14b shows the SXRCT tomogram as obtained from the reconstruction of the original projections. Here, the gray value of the image represents the sum $C + \mu$. As observed in the SXCT tomogram the material has homogeneous density and, thus, brighter areas indicate regions with high refraction value, i.e., high inner surface density. These areas correspond to fine cracks, most of which are not detected in the SXCT measurement. Some of these are indicated by red arrows in Figure 14b. These fine cracks can actually be up to 1 mm long. Furthermore, the edges of larger cracks appear bright as well. This is expected as the SXRCT measurement is intended to enhance surfaces and the roughness of these surfaces cause a relatively high refraction value. However, the top edges appear brighter than the bottom edges. This is caused by a slight dejustment of the analyzer crystal during the measurement causing the SXRCT projections to not be taken exactly at the maximum of the rocking curve. Figure 14c shows the tomogram of the reconstruction of the pure refraction value C. For this, the projections of the SXCT and SXRCT measurements where used to calculate projections representing the value $C \cdot d$ as described in Section 3.3.2 which were then reconstructed. Thus, bright areas indicate regions with high inner surface density just as in the reconstruction of the original SXRCT projections. The actual sample has vanished from the tomogram because the contribution of the linear attenuation coefficient is removed. Comparing Figure 14c to Figure 14b shows that all fine cracks visible in the reconstruction of the original SXRCT projections can also be identified in the reconstruction of C, i.e., no information is lost during the intermediate computations.

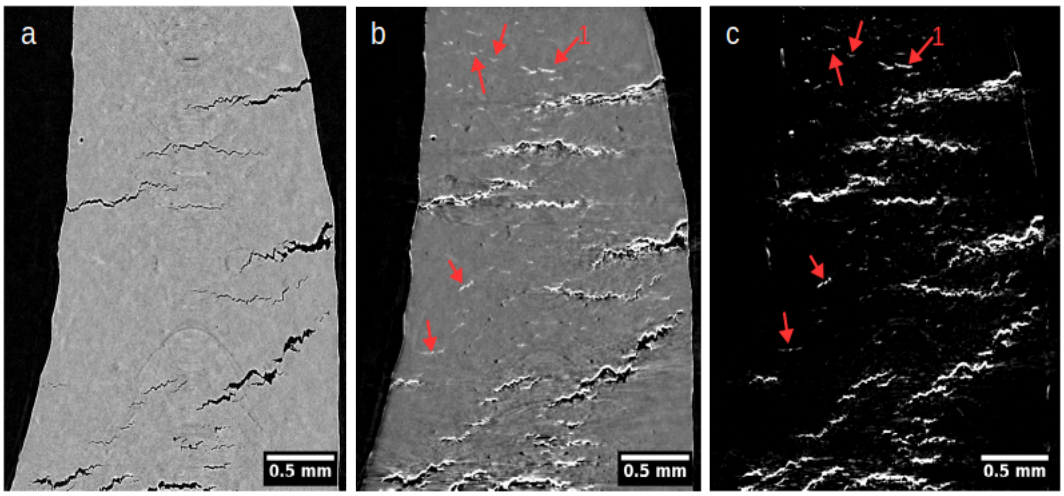

Figure 14: Vertical tomograms through the volumes of the coupon obtained from (a) reconstruction of the SXCT data, (b) reconstruction of the SXRCT data, and (c) reconstruction of the refraction value C calculated from SXCT and SXRCT data. SXCT and SXRCT measurements were performed with the same camera system and have the same spatial resolution. Red arrows indicate examples of cracks detected by SXRCT but not by SXCT.

The advantage of reconstructing C rather than the sum $C + \mu$ is that areas of high gray value in Figure 14c are unambiguously caused by inner surfaces whereas in Figure 14b they could also be caused by higher density particles. Only comparing Figure 14b with Figure 14a reveals that this is not the case. However, especially when analyzing multi-material samples (compare case study B, Section 4.2), such a comparison must be performed quantitatively to not overlook fine cracks within higher density particles. This would require a 3D registration of both volume data which is more complicated and would require advanced volume correlation methods to deal with the different image modalities.

The crucial step for calculating the projections representing $C \cdot d$ is the registration of the SXCT and SXRCT projections. This must be performed with sufficient accuracy to ensure that edges are not significantly blurred. Due to the edge enhancement caused by refraction, edges are already blurred in the SXRCT projections and, thus, the requirements to the precision is not as strict as, e.g., for digital image correlation.

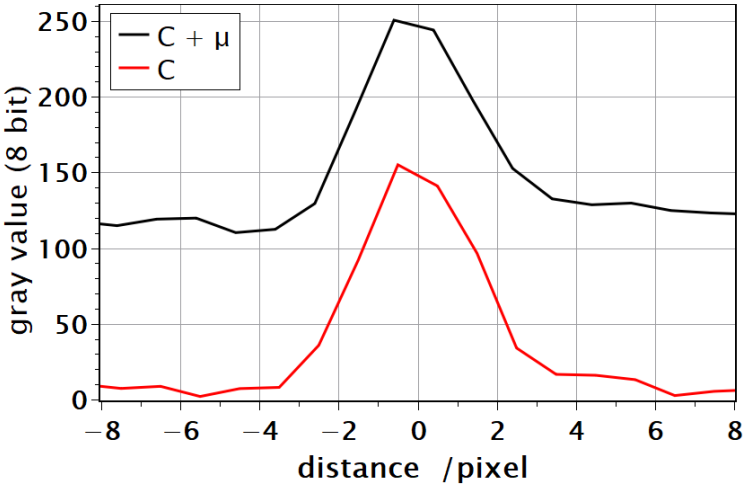

Figure 15: Profiles of a vertical line through the crack marked 1 in Figure 14b and c. Black profile is obtained from the reconstruction of the original SXRCT projections and red profile from the reconstruction of the calculated $C \cdot d$ projections.

Figure 15 shows examplarily the respective gray value profiles through the fine crack marked 1 in Figures 14b and c. The observed peaks representing the crack have approximately the same width (FWHM of 3.74 pixel) and amplitude (135 gray values); only the background is raised in case of the reconstruction from the original SXRCT projections by about 110 gray values. This is due to the added linear attenuation coefficient. Thus, no blurring from the registration is observed; this shows that the chosen registration approach is sufficiently precise. Furthermore, this verifies the model presented in Section 3.3 as the linear attenuation coefficient μ and refraction value C are shown to be indeed additive factors in Beer's law of attenuation. In the calculation of the $C \cdot d$ projections this is assumed but it is not inherently assumed in the reconstruction of the original SXRCT projections. Thus, a discrepancy would be observed in Figure 15 if the model would not hold.

4.1.4 Conclusion

In this case study SXRR and SXRCT was successfully applied to the crack detection in a coupon taken from an aluminum weld seam. It was demonstrated that the refraction based imaging techniques SXRR and SXRCT are capable of detecting fine cracks which cannot be identified in the respective absorption based imaging techniques X-ray radiography and SXCT due to limited spatial resolution. These fine cracks can have lengths of up to 1 mm and contribute significantly to the overall damage in the sample. In the SXRR radiograph the cracks could be segmented using a global thresholding method with sufficient accuracy to allow a quantitative analysis. The SXRCT and SXCT projections were successfully used to compute the 3D distribution of C, an approach realized for the first time in the course of this work. The approach of registering the original

SXCT and SXRCT projections is sufficiently precise to not introduce observable artifacts or inaccuracies into the images, e.g., increased edge blurring. Finally, the model for calculating C for synchrotron applications presented in Section 3.3.2 was verified.

For the analysis of cracks both methods, SXCT and SXRCT, are complementary. Cracks with openings of at least several pixels are better analyzed with SXCT, because the edges of these cracks are significantly blurred in SXRCT measurements, and the surface of these cracks cannot be determined accurately. However, smaller cracks cannot be detected by SXCT and the refraction contrast is necessary to be able to analyze them.

4.2 Case Study B: Aluminum based metal-matrix-composite under *in-situ* tensile loading

In this case study SXRR is used to quantitatively analyze *in-situ* the evolution of internal damage in a particle reinforced metal-matrix-composite (MMC) during tensile loading. The study represents the first application of SXRR in combination with *in-situ* loading. Also a qualitative comparison between SXRCT and SXCT is presented. The experiments were performed in collaboration with TU Dortmund. The collegues provided the samples and a custom made tensile test rig which allows *in-situ* X-ray imaging. They also assisted during the *in-situ* SXRR measurements controlling the test rig. The author performed the SXRR, SXRCT and SXCT measurements as well as all post-processing and the data analyses. The results of this case study have been published in [72].

4.2.1 Motivation

Materials science aspects In general, aluminum-based MMCs possess low density, high strength, and high stiffness. Therefore, they are promising structural materials for light weight applications. However, their composition of brittle ceramic reinforcements embedded in a ductile metallic matrix leading to smaller fracture toughness than the matrix, that limits their practical use. Therefore, the damage mechanisms in MMCs were intensively studied [73]. In particle reinforced composites, they are divided into three classes: (1) matrix ductile fracture, (2) matrix/particle decohesion, and (3) particle cracking. The damage in the ductile matrix begins as strain concentrations with subsequent nucleation of voids or cracks of sub-micrometer size. In the course of mechanical loading these microcracks grow and coalesce to form longer, macroscopic cracks.

On a microscopic level these mechanisms have been investigated, e.g., by means of high resolution synchrotron X-ray tomography; also with *in-situ* tensile loading [74–82]. The focus of these investigations was to resolve individual cracks and analyze their formation and growth in dependence of different loading states. The nominal pixel sizes ranged from $(1\,\mu m)^2$ to $(2\,\mu m)^2$ and the investigated volumes were relatively small with $(0.5\,mm)^3$ to $(2\,mm)^3$. Also the particle sizes, ranging between 40 µm and 200 µm, were chosen according to the respective spatial resolution so that the particles can be easily resolved.

However, for the analysis of materials with smaller reinforcement particles or the investigation of larger sample volumes the ability to detect and quantify cavities of sub-resolution size is required. Therefore, this case study explores the suitability of SXRR for *in-situ* measurements as it allows the analysis of damage evolution on a larger scale.

Methodological aspects The measurement with *in-situ* tensile loading poses a special challenge to SXRR imaging. The individual measurements of the series must be quantitatively comparable without significant fluctuations of the gray values in subsequent measurements. Therefore, the imaging system must be sufficiently stable to achieve the required repeatability or a reference is needed for every measurement to

allow normalization of the series. In the usual *ex-situ* case, the DCM and analyzer crystal are adjusted before every measurement. However, a precise adjustment cannot be performed for each measurement of the *in-situ* series. However, it is demonstrated that the need for such readjustments is superseded at least for the measurements performed in short succession, i.e., within one *in-situ* series.

The SXRCT measurement is compared to a SXCT measurement of higher resolution to investigate the limit for the detection of small cavities by SXRCT. For the analysis of the SXRCT data the calculation of projections representing the refraction value $C \cdot d$ from the original projections, as described in Sections 3.3.1 and 3.3.2 is necessary. The different constituents of the material have different X-ray attenuation properties and, thus, the contrast in the radiograph at the maximum of the rocking curve can arise either from higher attenuation or refraction. A reconstruction of the pure refraction value is, therefore, required to unambiguously identify regions of high inner surface density.

4.2.2 Material and method

Material The MMC investigated in this case study consisted of an Al6061 matrix reinforced with 10 vol% ceramic Al_2O_3 particles with particle sizes between 2 µm and 40 µm. The chemical composition of the matrix is provided in Table 2. The composite material was produced via a melting metallurgical route by the Leichtbaukompetenzzentrum Ranshofen (LKR), Austria. After primary forming the material was extruded. The extrusion process causes the reinforcement particles to be aligned parallel to the extrusion direction as is evident from the optical micrograph shown in Figure 16b. The samples were subjected to a peak-aging heat treatment (T6) which consists of three steps: 1) homogenization at $T = 530\,°C$ for 30 min, 2) quenching in water to ambient temperature, and 3) precipitation annealing at $T = 160\,°C$ for 24 h. During the precipitation annealing, fine Mg_2Si precipitates form in the matrix phase.

Table 2: Chemical composition of the matrix material Al6061 in wt%

Element	Cr	Cu	Fe	Mg	Mn	Si	Ti	Zn	Al
wt-%	0.04-0.35	0.15-0.4	0.7	0.8-1.2	0.15	0.4-0.8	0.15	0.25	bal.

For the *in-situ* experiments dog-bone shaped samples (see Figure 16a) have been prepared. The cross section of the gauge volume was about 1.7 mm × 2.7 mm. The dimensions were chosen because the samples also had to be suitable for high resolution CT measurements. SXRR would have supported larger cross sections with the attenuation length of the material being the most important restraint.

Tensile tests and X-ray imaging The tensile test rig was placed on the sample stage in such a way that the X-rays could pass through the gauge section of the sample during loading as shown in Figure 17a. For that purpose the design of the test rig included a window in the back plate (Figure 17b).

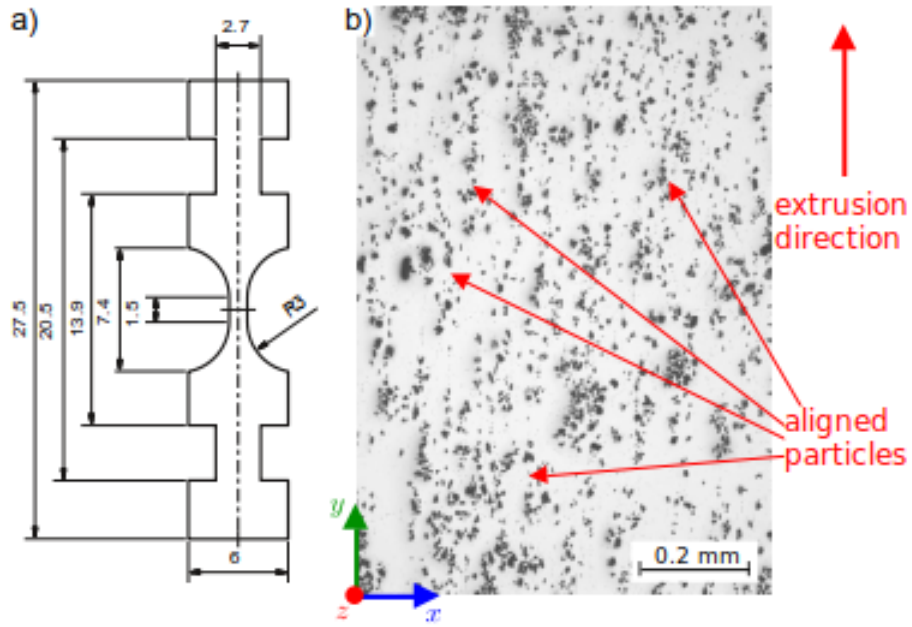

Figure 16: a) Drawing of the samples with dimensions in mm, thickness = 1.7 mm; b) Optical micrograph of the polished sample surface showing the alignment of Al_2O_3 particles with extrusion direction

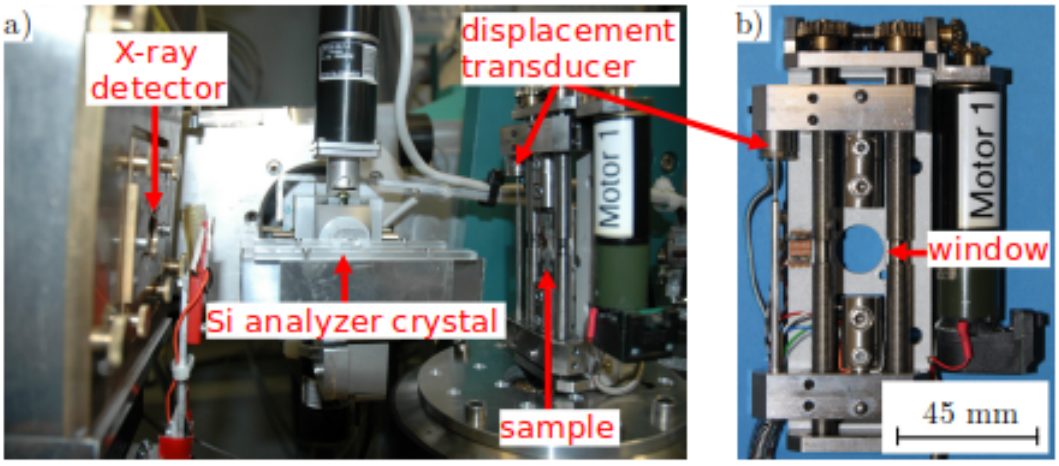

Figure 17: a) Photograph of the experimental set up for *in-situ* SXRR with tensile rig, analyzer crystal and X-ray detector; b) Photograph of the tensile test rig showing the window for X-rays

The tensile load was applied displacement controlled and the loading course was interrupted several times to capture complete rocking curves of the sample. The radiographs were taken with a 2048 × 2048 pixels camera with a nominal pixel size of

$(3.5\,\mu m)^2$. During image acquisition the displacement was held constant. This lead to a drop of the applied stress due to relaxation of the specimen at each step. This procedure was chosen to avoid sample movement during image acquisition which would have caused artifacts. The stress levels at which the loading course was interrupted are summarized in Table 3 and the corresponding plots of engineering stress vs. elongation are presented in Figure 18. Two samples, labeled B1 and B2, were investigated with different load intervals between SXRR measurements. For sample B1 the tensile test was interrupted regularly during the entire loading cycle (see Table 3 (left) and Figure 18a). For sample B2 the tensile test was interrupted more frequently at loads above the yield strength of the material to closely investigate the damage evolution during plastic deformation (see Table 3 (right) and Figure 18b). Each time, the loading was stopped shortly before reaching the ultimate strength of the material.

Table 3: Stress levels for SXRR measurements of samples B1 (left) and B2 (right)

State	Engineering stress /MPa
0	10
1	148
2	156
3	166
4	196
5	245
6	294
7	303
8	330

State	Engineering stress /MPa
0	11
1	148
2	294
3	300
4	305
5	309
6	314
7	319
8	323
9	328
10	331

The SXRR measurements were performed according to the general description in Section 3.3.1 with 41 exposures per rocking curve. A photon energy of 22 keV was selected which resulted in a transmission of about 33 %. At each load state the rocking curve of the sample was recorded and immediately followed by a rocking curve of the free X-ray beam, i.e., the flat-field. This procedure was chosen over the procedure of capturing both images at each analyzer crystal position. The results of both procedures proved to be of similar quality with respect to image artifacts. However, this is only true if the time period between the two measurements is not longer than a few minutes. Image artifacts are caused by defects, e.g., scratches, in the monochromator, analyzer crystal, and scintillator. Since, these are independent objects in the optical path of the

X-rays their relative positions in the image can change due to thermal or mechanical drifts. Therefore, a mismatch between flat-field and object image cannot be fully compensated by image registration. In addition to the rocking curves, a radiograph without the analyzer crystal was taken as well at each load state for comparison. This required the analyzer crystal to be moved out of and back into the X-rays path each time. At the end of the load cycle another measurement was taken after removing the load. After the load cycle sample B1 was investigated *ex-situ* by SXRCT as well as SXCT with the same optics as the SXRR measurements. In addition, it was investigated by a second SXCT measurement with a nominal pixel size of $(0.5\,\mu m)^2$ using the standard SXCT setup at BAMline and the DMM for energy selection.

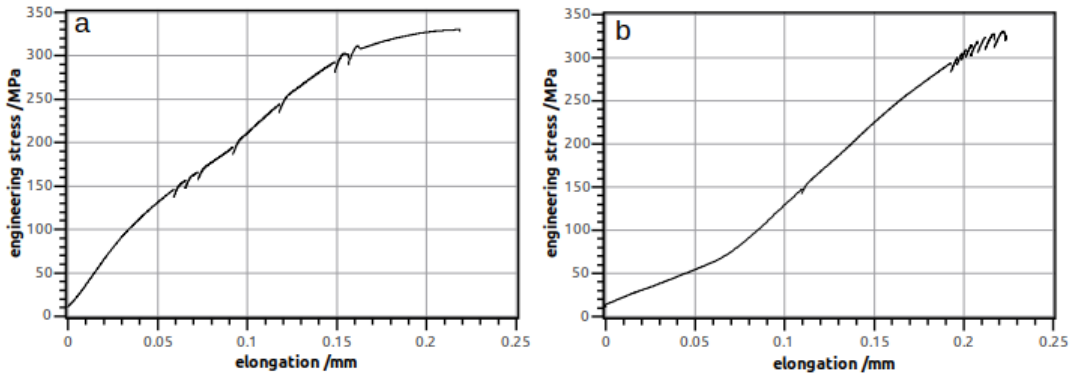

Figure 18: Stress elongation curves of samples B1 (a) and B2 (b); states at which SXRR measurements were preformed can be identified by the discontinuities in the curves

Image Processing The obtained rocking curves were evaluated according to Section 3.3.1 by calculating $\frac{C}{\mu}$. Similarly, $\mu \cdot d$ was calculated from the respective X-ray radiographs according to Section 3.2.1 from the radiographs taken without analyzer crystal. The resulting individual images of each load cycle were aligned so that the gauge section appears at the same position in all images. For quantitative evaluation, the mean value of $\frac{C}{\mu}$ across the gauge section and a reference area was determined. As reference a combined area of the sample above and below the gauge section was selected. These areas can be expected to be unaffected by the applied load as the engineering stress in these regions is much smaller due to the larger cross section.

The projections of the SXRCT scan and the SXCT scan with the same resolution were registered to each other and then a set of projections of $C \cdot d$ were calculated and reconstructed yielding the 3D distribution of C according to Section 3.3.2. All reconstructions were performed using the custom filtered backprojection software of BAM. The high-resolution SXCT volume was filtered with a bilateral Gaussian filter [83] to reduce ring

artifacts. Such a filter smooths the image by convolution with a Gaussian kernel. However, if the difference in gray values exceeds a specified limit the kernel is cut off so that the smoothing is only applied to homogeneous regions and not across edges. Thus, a bilateral Gaussian filter is considered to be edge preserving.

4.2.3 Results and discussion

Figure 19 shows complete SXRR radiographs of selected load stages from sample B1 representing $\frac{C}{\mu}$. The proportions of the gauge section and the image size illustrate the potential of investigating larger gauge sections with SXRR of up to several millimeters. The loading state of 10 MPa represents the initial state with only a small pre-load applied to fix the specimen in the test rig. This state already shows a significant value of $\frac{C}{\mu}$, which is caused by the interfaces between matrix and Al_2O_3 particles and Mg_2Si precipitates, as well as initial imperfections, like cracks and pores, introduced during sample preparation. Increasing the load to 294 MPa, which is just around the yield stress of the material, does not lead to an apparent change of $\frac{C}{\mu}$. Only in the last loading state at 330 MPa an increase of $\frac{C}{\mu}$ in the gauge section of the sample occurs.

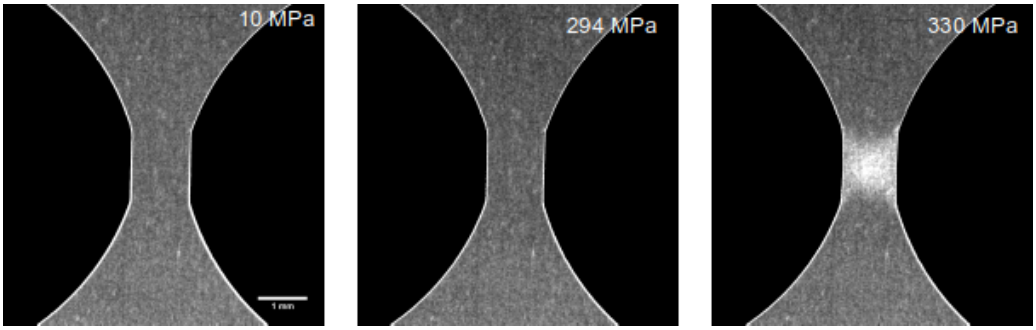

Figure 19: Radiographs of the relative specific surface $\frac{C}{\mu}$ at selected load states of 10 MPa (initial state), 294 MPa (around yield stress), and 330 MPa (final state) of sample B1

The large field of view, in this case, offers the confirmation that the regions above and below the gauge section can be used as reference. In these areas no change of the microstructure occurs during the tensile test and, therefore, the repeatability of the measurement can be evaluated. The respective plots of $\frac{C}{\mu}$ against the applied engineering stress are shown in Figure 20.

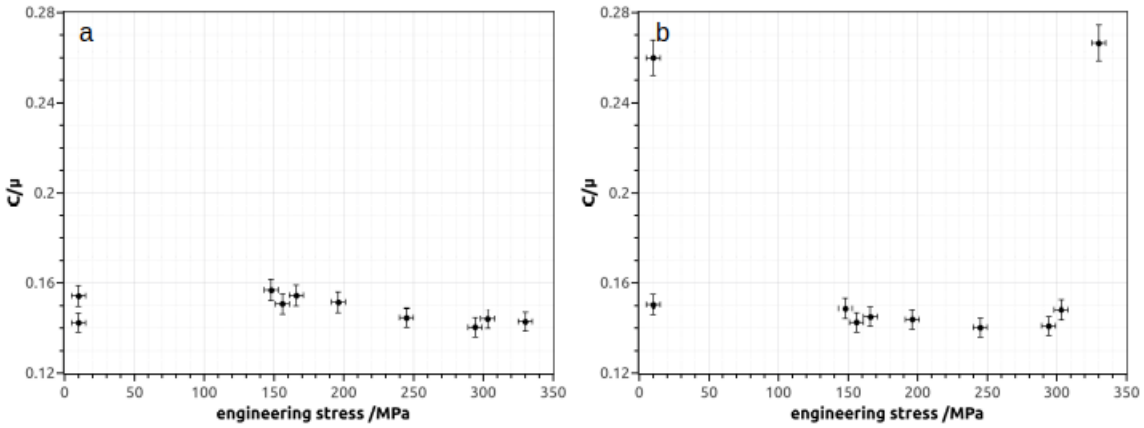

Figure 20: Plots of the relative specific surface $\frac{C}{\mu}$ against the applied engineering stress (a) outside the gauge section and (b) inside the gauge section for sample B1. Error bars represent $\pm 3\,\%$ on the ordinate, which represents the estimate of the uncertainty for a single measurement, and $\pm 5\,\mathrm{MPa}$ on the abcissa, which is based on the relaxation during measurement

Outside the gauge section (Figure 19a) $\frac{C}{\mu}$ ranges between 0.140 and 0.157 and appears to be continuously decreasing. This decrease is caused by an increasing dejustment of the analyzer crystal or the DCM. If uncorrected, this spread must be considered as the uncertainty of the measurement as this area does not show any change of the microstructure during the tensile test. Inside the gauge section a similar decrease can be recognized up to an engineering stress of about 250 MPa. A significant increase of $\frac{C}{\mu}$, indicating damaging of the sample, only occurs at the last load step. Comparing Figure 20 to the respective stress elongation curve in Figure 18a, it can be recognized that only the last measurement was taken at an engineering stress above the yield stress.

To investigate the increase of $\frac{C}{\mu}$ beyond the yield stress more closely, the load cycle of sample B2 was interrupted more frequently during plastic deformation. Selected radiographs of sample B2 are presented in Figure 21 showing only the enlarged gauge section. The SXRR radiographs shown in Figure 21a reveal a continuous increase of $\frac{C}{\mu}$ over several load steps, which appears to be growing from the right hand side of the sample. This asymmetry is caused by a superimposed bending moment induced by the sample fixture. Although $\frac{C}{\mu}$ increases over a relatively large area, several hotspots can be identified where $\frac{C}{\mu}$ is the highest at all load steps. Some of these spots can already be identified in the initial unloaded state. Thus, it can be concluded that damage is induced within the entire sample. However, the highest amount of damage is localized at initial imperfections, which continue to grow. The results of the conventional radiographs, visualizing the quantity $\mu \cdot d$, are shown in Figure 21b. Here, no change of the sample with load can be recognized. This demostrates the higher sensitivity of SXRR for the detection of inner surfaces.

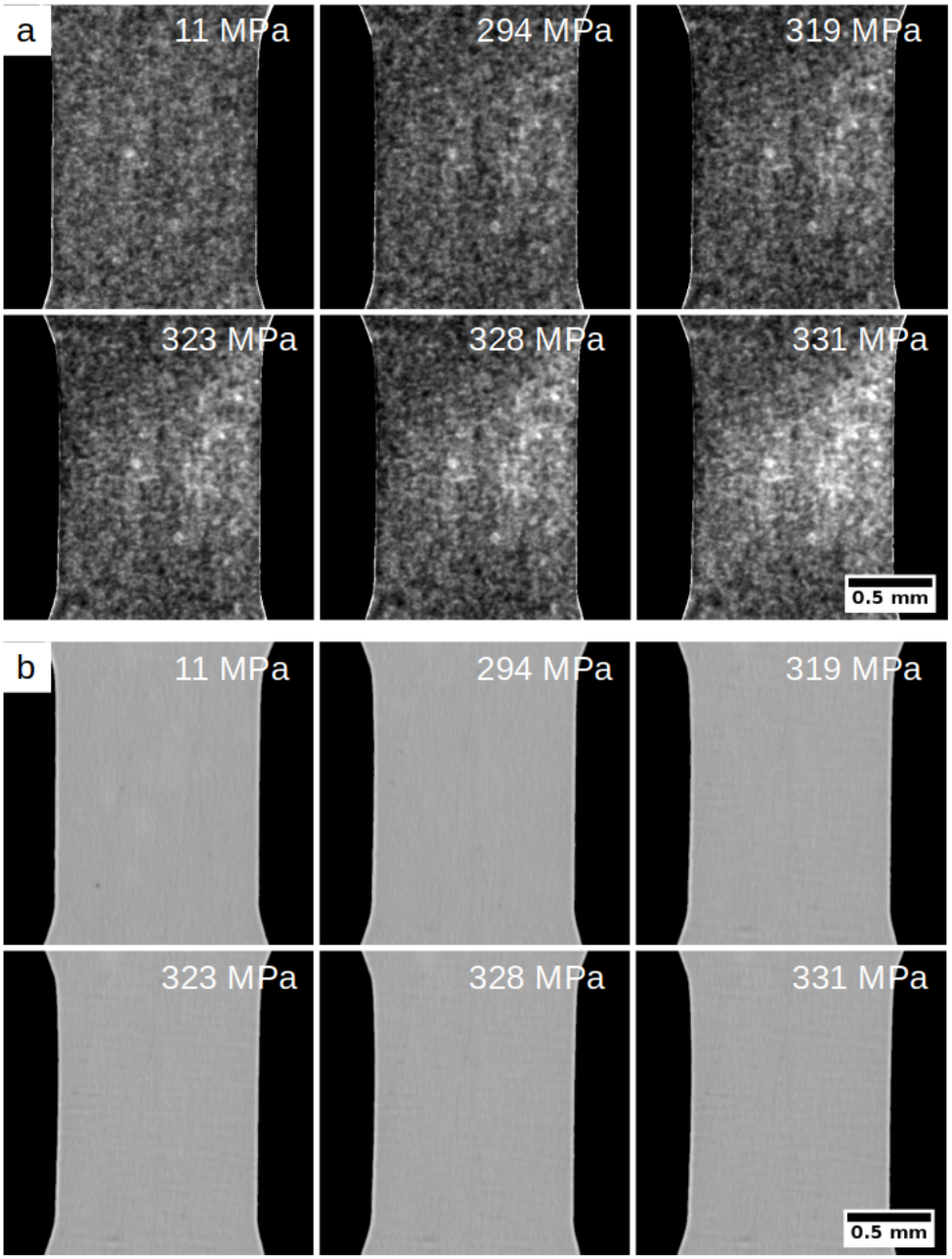

Figure 21: a) SXRR radiographs of the relative specific surface $\frac{C}{\mu}$ at selected load steps showing the enlarged gauge section of sample B2; b) conventional radiographs of $\mu \cdot d$ at selected load steps showing the enlarged gauge section of sample B2

The change of $\frac{C}{\mu}$ with applied stress of sample B2 is plotted in Figure 22. Outside the

gauge section, shown in Figure 22a, $\frac{C}{\mu}$ behaves similar as in sample B1 with exception of the initial and final measurement at the preload of 11 MPa. In these two measurements a global increase of $\frac{C}{\mu}$ is observed. For the other measurements $\frac{C}{\mu}$ ranges between 0.142 and 0.152, also showing a continuous decrease. Inside the gauge section a rapid increase of $\frac{C}{\mu}$ is observed at stresses above 300 MPa.

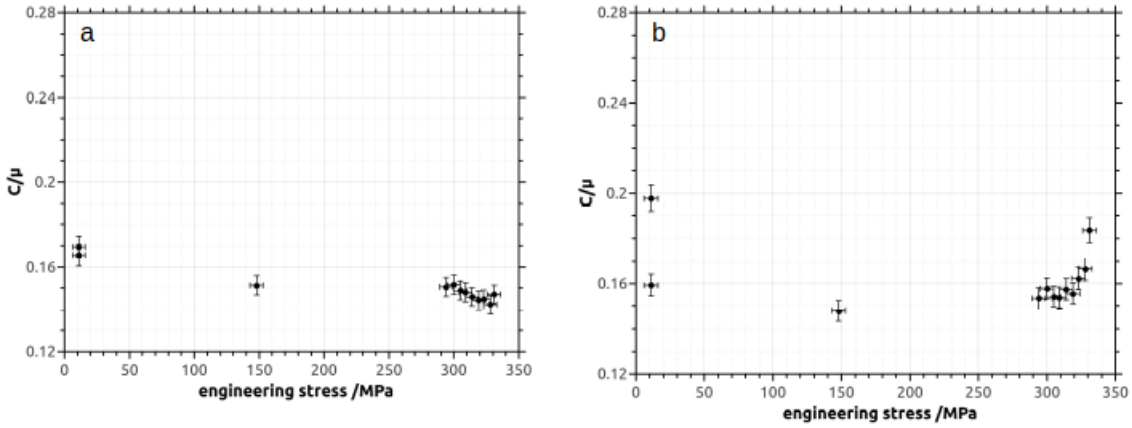

Figure 22: Plots of the relative specific surface $\frac{C}{\mu}$ against the applied engineering stress outside the gauge section (a) and inside the gauge section (b) for sample B2. Error bars represent ± 3 % on the ordinate, which represents the estimate of the uncertainty for a single measurement, and ± 5 MPa on the abscissa, which is based on the relaxation during measurement

To compensate for the variations between subsequent measurements observed in the reference area outside the gauge section, one possibility is to regard only the difference between gauge section and reference area. This difference $\Delta\frac{C}{\mu}$ is plotted against the engineering stress in Figure 23 and represents the amount of additional free surfaces within the gauge section with respect to the initial condition. As damage is generally associated with an increasing amount of free surfaces through the generation and growth of cracks or voids, $\Delta\frac{C}{\mu}$ is a direct measure for the amount of damage induced by the tensile load. $\Delta\frac{C}{\mu}$ does not change significantly up to a stress of 300 MPa. After that point, the amount of damage increases rapidly and non-linearly in the stress region of 300 to 330 MPa. At the final state $\Delta\frac{C}{\mu}$ has increased to 0.124 and 0.037 for samples B1 and B2, respectively. Comparing this result to the stress elongation curves in Figure 18 shows that the initiation of damage coincides with the transition from elastic to plastic deformation. Hence, additional damage is only induced during plastic deformation, which is in accordance with results reported in the literature [75, 78, 80, 82]. Around 330 MPa, which is close to the ultimate strength of the material (see Figure 18), the increase becomes asymptotic indicating imminent failure. Comparing the result of the last state of each series with the result from the measurement after removing the load a decrease of $\Delta\frac{C}{\mu}$ can be observed. This means that small cavities are held open by the

in-situ load and close upon unloading.

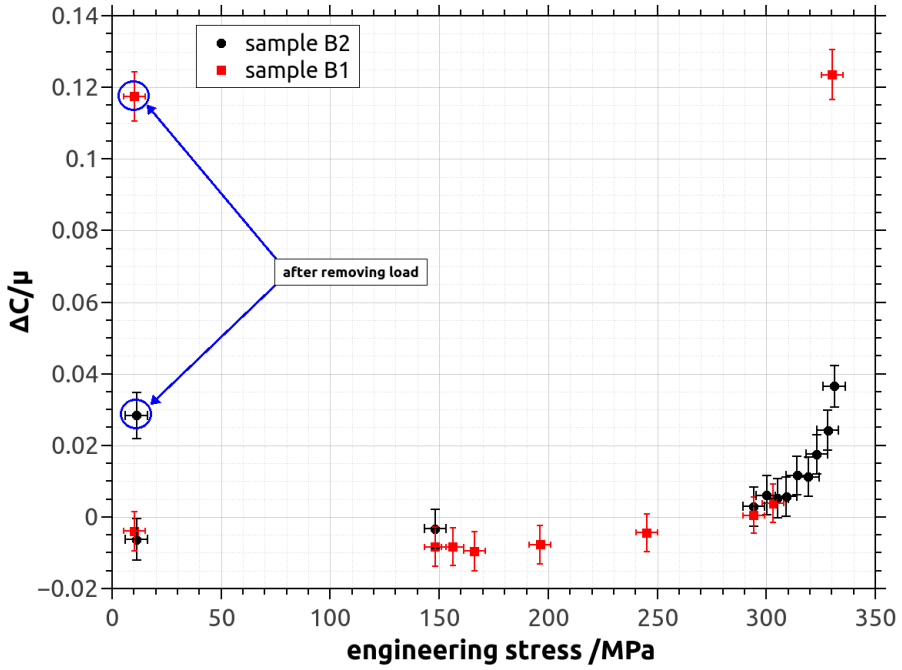

Figure 23: Difference of relative specific surface between gauge section and reference area $\Delta\frac{C}{\mu}$ plotted against engineering stress for both samples B1 and B2. Error bars on the ordinate are based on the estimated $\pm 3\,\%$ of the original data through error propagation, and $\pm 5\,\mathrm{MPa}$ on the abcissa, which is based on the relaxation during measurement

To identify the microstructural features that cause the increase of $\frac{C}{\mu}$, sample B1 has been investigated by means of SXCT with different resolutions (voxel sizes of $(3.5\,\mu\mathrm{m})^3$ and $(0.5\,\mu\mathrm{m})^3$) as well as with SXRCT (voxel size of $(3.5\,\mu\mathrm{m})^3$). Tomograms taken at the same position in the sample of all three measurements are shown in Figure 24. In the high-resolution SXCT tomogram (Figure 24c) the individual cavities are recognized. The sample contains matrix cracks, debonded particles as well as cracked particles, although it appears that the most frequent type of damage is particle cracking. In the lower resolution SXCT tomogram (Figure 24b) only the largest of these are identified. The majority of defects is too small to be resolved. For example, none of the defects presented as enlarged details in Figure 24 (bottom row) can be recognized. In the SXRCT tomogram (Figure 24a), however, all the cavities recognizable in the high-resolution tomogram can be identified as well, despite the fact that the resolution of SXRCT is lower. As an example, all cavities shown in the enlarged details produce a distinct signal in the SXRCT tomogram. This demonstrates that the detectabilty of cavities in a SXRCT measurement is comparable to that in a SXCT measurement of at least seven times better spatial resolution.

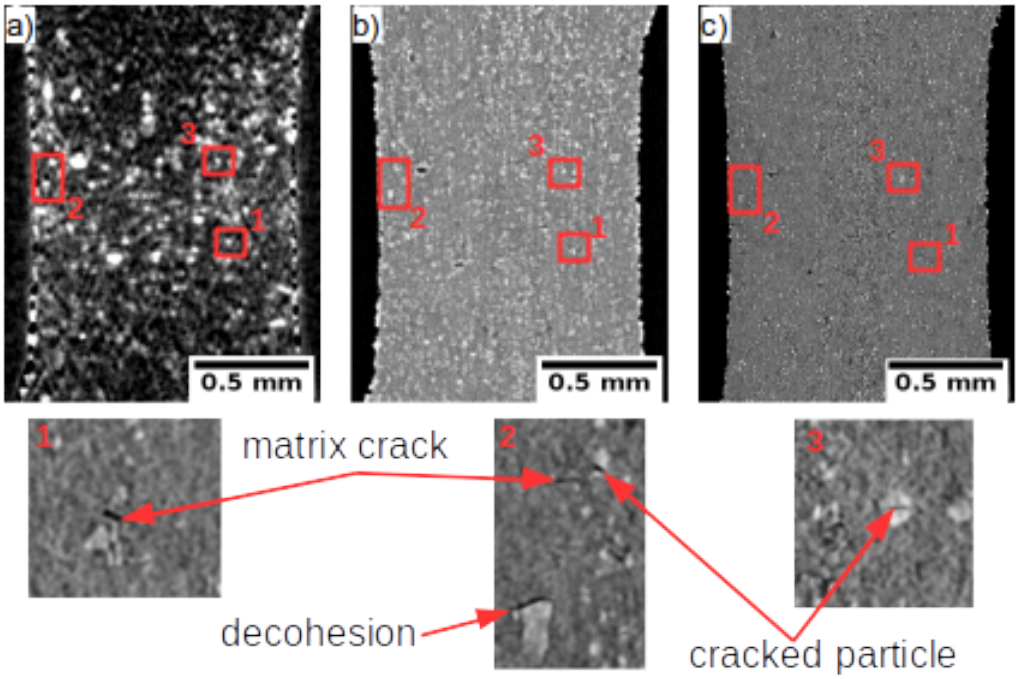

Figure 24: Tomograms of sample B1 obtained by a) SXRCT with voxel size $(3.5\,\mu m)^3$, b) SXCT with voxel size $(3.5\,\mu m)^3$, and c) SXCT with voxel size $(0.5\,\mu m)^3$. 1, 2, and 3 show 6× magnified details of the high resolution SXCT tomogram, red rectangles indicate the corresponding positions in all tomograms

4.2.4 Conclusion

In this case study SXRR was, for the first time, successfully applied to monitor the evolution of mechanically induced damage under *in-situ* load in an Al6061 / Al_2O_3 MMC. It was possible to follow the increasing amount of damage over several load states beginning immediately after reaching the yield stress. Additional damage is generated only during plastic and not during elastic deformation. Damage increases asymptotically approaching the ultimate strength of the material. High-resolution SXCT revealed the individual cavities to be cracked particles, matrix cracks, and debonded particles; the most frequent defect type appeared to be the first.

SXRR was shown to be well suited for *in-situ* applications. As it is a 2D technique no rotation of the loaded sample is required. This allows for a simpler design of the test rig compared to *in-situ* CT. Also, the X-ray attenuation poses only a restriction to sample size in one direction (thickness) allowing investigation of plate shaped samples with large volume. With respect to the quantification of damage, SXRR offers similar information as high-resolution SXCT without the necessity of complex crack detection algorithms. However, a distinction between different damage mechanisms is not possi-

ble. Thus, SXRR and SXCT complement each other with SXRR offering quick and easy access to the global amount of damage in relatively large samples and SXCT providing detailed information on the mechanisms involved.

The accuracy of the SXRR measurement within one measurement series and the repeatability between measurement series is about 10 % without any corrections. Normalization to a reference area improves the repeatability to less than 3 %. This is sufficient for a quantitative analysis of damage in this case study. The most important source of error is a mismatch between the images of the object and the respective flat-field image. To minimize this error the time interval between measurement and flat-field should not be longer than a few minutes.

SXRCT was shown to detect cavities which are barely recognizable in a SXCT measurement with seven times better spatial resolution. Trivially, for SXRCT the same restrictions to sample geometry apply as for SXCT and the measurement time increases by a factor of two since two subsequent CT scans are required for the calculation of $\frac{C}{\mu}$.

4.3 Case Study C: Porosity analysis in Ti-Al6-V4 produced by laser powder bed fusion

In this case study SXRR is applied to the analysis of porosity in additively manufactured laser powder bed fusion (LPBF) Ti-Al6-V4. The experiments were performed in collaboration with the Institute for Materials Research of the German Aerospace Center (Deutsches Zentrum für Luft- und Raumfahrt, DLR), Department Metallic and Hybrid Materials. The collegues provided the materials science backgroud, prepared the samples, and were responsible for Archimedes and microscopy measurements as well as high-resolution SXCT measurements at ESRF. SXRR and SXCT measurements at BAM-line were performed by the author who is also responsible for all analyses of these data. The results of this case study have been published in [84, 85].

4.3.1 Motivation

Materials science aspects Laser powder bed fusion (LPBF) is a powder bed additive manufacturing technique enabling near net-shape production of components. In the process, a layer of powder is deposited onto a base plate and then selectively fused by means of one or more lasers. After one such layer is processed the base plate is lowered and a new layer of powder is deposited on top, which is again selectively fused. Thus, the part is created layer by layer. The so called build direction is the direction in which the new layers are deposited on top of each other, i.e., the opposite of the base plates movement direction.

LPBF, just like other additive manufacturing techniques, enables the fabrication of very complex and customized parts directly from computer aided design (CAD) models [86]. Because of these advantages many industries, such as aerospace, began to intensively explore the technology over the last decade. In the aerospace industry the titanium alloy Ti-Al6-V4 is widely used in the form of wrought products owing to its well-balanced properties which combine mechanical performance, corrosion resistance, and low density. Therefore, the production of this material by LPBF has been in the focus of much research activity. While Ti-Al6-V4 is generally well suited for LPBF production, rapid solidification during the process and non-optimal process parameters cause instabilities. Both factors lead to the formation of several types of internal defects: binding or fusing faults, balling, keyhole pores, and crack formation from thermal residual stresses [87]. These defects have a large impact on the damage tolerance behavior of the material, especially under cyclic loading, as confirmed experimentally in, e.g., [88–91], and by numerical simulations in, e.g., [92]. Thus far, several studies have dealt with the optimization of LPBF process parameters or post-treatment leading to improved static and fatigue properties of the LPBF parts (e.g. [87–89, 93, 94]). It was found that the minimum of porosity occurs only in a narrow window of processing parameters and outside of this window the amount of defects increases due to either over-heating (keyhole pores) or insufficient fusion (binding defects, balling) [95]. However, not only the total amount of porosity is important for the mechanical properties of the material but also the shape, or morphology, of the defects [96–98]. It could be shown that binding

defects are more detrimental to the mechanical properties of the material than keyhole pores [91] and, thus, the process parameters should be adjusted to minimize this type of defect.

Methodological aspects Methods commonly applied to the investigation of porosity in additive manufactured materials are Archimedes method, optical microscopy, and SXCT. However, all of these methods have their specific shortcomings in detecting and identifying small voids or thin cracks. Archimedes method can provide an indication for the amount of void within the sample, however, it fails to account for open porosity and compositional changes. Also no information about the morphology of voids can be gained. Optical microscopy offers insights into the morphology as well as the total amount of porosity but is only a local probe and requires tremendous experimental work to gain statistically relevant information, since multiple micrographs need to be taken with preparation steps in between. SXCT offers even more detailed information about morphology and porosity in the sample. However, the spatial resolution of the tomograms sets a limit to the smallest detectable defects. A reliable detection of defects smaller than 1 µm is at the limit of even advanced SXCT and, as with optical microscopy, the good spatial resolution comes at the price of a small probed volume which again means that multiple measurements are required to gain statistically relevant information.

This case study explores SXRR as a suitable method for the investigation of porosity in LPBF materials to complement other established methods. The main advantage of SXRR is the possibility to investigate relatively large sample volumes and still detect very small defects (< 1 µm). Furthermore, the sensitivity of SXRR to surface orientation offers information about the defect morphology, thus providing statistically relevant information about porosity and morphology with fewer measurements and less experimental effort.

With respect to the previous two case studies this one marks a step towards stronger absorbing metallic materials. In the relevant photon energy range the linear X-ray attenuation coefficient of Ti is seven to eight times higher than that of Al and, therefore, a higher photon energy needs to be selected for the imaging of Ti. This leads to smaller refraction angles and, thus, to a reduced contrast in the SXRR radiographs. As an example, for Ti imaged at 30 keV the refraction angles are about 20 % smaller than for Al imaged at 22 keV. This case study demonstrates that this reduction of contrast does not compromise the SXRR analysis.

4.3.2 Material, sample preparation, and X-ray imaging

For the study, cuboids of 10 mm × 10 mm × 10 mm were produced in an SLM-280 HL (SLM solutions) machine equipped with a 400 W laser operating at a wavelength of 2070 nm. The chamber was under argon atmosphere and the building platform was held at 200 °C. The raw material was Ti-Al6-V4 ELI powder received from Advanced Powders & Coatings (AP&C, Canada) with a size distribution such that 10 % of the

particles are smaller than 31 µm (D10), 50 % smaller than 42 µm (D50), and 90 % smaller than 53 µm (D90).

The cuboids were produced with a laser power P of 175 W, a hatch distance h of 0.1 µm, a layer thickness l of 30 µm, and a laser focus of 0 mm with respect to the layer surface, i.e. the laser beam was focussed on the surface of the processed layer. Only the scanning velocity v was varied between 200 mm s^{-1} and 1100 mm s^{-1}. In terms of the commonly used volume energy density E_v, defined as $E_\mathrm{v} = \frac{P}{v \cdot h \cdot l}$, this translates into a variation between 50 J mm^{-3} and 300 J mm^{-3}. The exact values of scanning velocity and resulting volume energy density of the samples are listed in Table 4.

Label	C1	C2	C3	C4	C5
scan velocity /mm s^{-1}	200	300	500	800	1100
energy density /J mm^{-3}	292	195	117	73	53

Table 4: Sample labels with respective scanning velocities and resulting volume energy densities; all other production parameters remained constant

Although the individual parameters impact porosity differently, it is common practice to describe porosity in dependence of E_v. It was shown in several studies (e.g. [89, 95, 96]) that there exists an optimum energy density where the porosity is lowest and that on either limit of this optimum different defect types dominate. On the one hand, fusing defects and balling are observed at volume energy densities below the lower limit, which appear as crack-like voids of up to more than 100 µm length sometimes filled with unprocessed powder particles. On the other hand, round vaporization (keyhole) pores are observed at energy densities above the upper limit, which can have diameters of up to 50 µm. The range of energy densities chosen in this case study covers all of these regions.

For each cuboid the porosity was analyzed by different methods. First, the entire cuboid was characterized by the Archimedes method (with $\rho_0 = 4.43\,\mathrm{g\,cm^{-3}}$). Afterwards, several samples were prepared from each cuboid for further investigations. For 2D optical microscopy, at least three metallographic cross-sections perpendicular to the building direction were prepared and for each cross-section the entire 10 mm × 10 mm area was investigated with about 100 individual micrographs. For SXCT three cylinders with a diameter of 0.8 mm and a height of 7 mm were prepared. The microscopy, tomography, and Archimedes experiments as well as the sample preparation were performed by the project partners from DLR and further details can be found in [95]. For SXRR 0.35 mm thick plates (10 mm × 10 mm lateral size) were cut from the center of each cuboid parallel to the building direction and polished on both sides with SiC grinding paper up to 4000 grit. The thickness of the plates is limited by the transmission that can be achieved with a reasonable photon energy and the polished surface is necessary to avoid artifacts.

The SXRR experiments were performed as described in Section 3.3.1. The photon energy was set to 30 keV resulting in a transmission of about 30 % and the rocking curve was sampled in 61 steps in a range of $\Delta\theta = \pm 0.006°$ around θ_B. The nominal pixel size of the X-ray detector was $(3.5\,\mu m)^2$ and the actual spatial resolution was determined to be 5 µm by means of a microfocus resolution chart for X-rays (JIMA RT RC-02). The analyzed field of view was 6.37 mm × 4.78 mm. The samples were imaged in two orientations: first, with the building direction laying within the scattering plane of the analyzer crystal, called parallel orientation, and, second, with the building direction perpendicular to the scattering plane, called perpendicular orientation. Using the recorded rocking curves $\frac{C}{\mu}$ was computed according to Section 3.3.1. Also X-ray radiographs were taken of each sample using the same detector unit as for the SXRR measurements to determine the porosity of the samples according to Section 3.2.1. The nominal X-ray attenuation coefficient μ_0 was determined from a reference area of each sample which was free of pores. This was necessary because the exact composition and density of the material after LPBF processing is unknown and no tabulated data on the X-ray attenuation coefficient exists. To further corroborate the results of SXRR a small portion was cut out of two of the plates, which were then investigated by SXCT at BAMline with a voxel size of $(0.43\,\mu m)^3$. In that way tomographic images and SXRR projections of the exact same defects were acquired.

4.3.3 Results and discussion

Porosity analysis The porosity maps calculated from X-ray radiographs of all samples taken in both orientations are shown in Figure 25. The gray value of these maps represents the local porosity, i.e., the porosity in a volume element defined by the pixel size and the thickness of the sample. Sample C3 shows the smallest number of pores. For all samples there is no significant difference between the two orientations, as would be expected. In sample C1, which was produced at a volume energy density well above the upper limit of the optimum region, keyhole pores are observed as the predominant type of defect. In samples C4 and C5, which were produced at volume energy densities well below the lower limit of the optimum region, binding defects are observed as the predominant defect type. A quantitative evaluation of the shape, however, is not possible since shape descriptors such as circularity do not yield accurate results because of the overlap of defects at different depths of the sample and the small size of many defects.

The total porosity of the samples was determined as the sum over all pixels of the porosity maps and averaged over both orientations. The results are presented in Figure 26 together with the results of optical microscopy, Archimedes, and SXCT. All methods except Archimedes method show a minimum porosity of < 0.05 % at a volume energy density of about $120\,J\,mm^{-3}$. X-ray radiography and microscopy show similar results for the total porosity, while SXCT yields significantly higher porosities at lower volume energy densities. This is likely due to a higher sensitivity of SXCT to small crack-like cavities because SXCT offers the best spatial resolution.

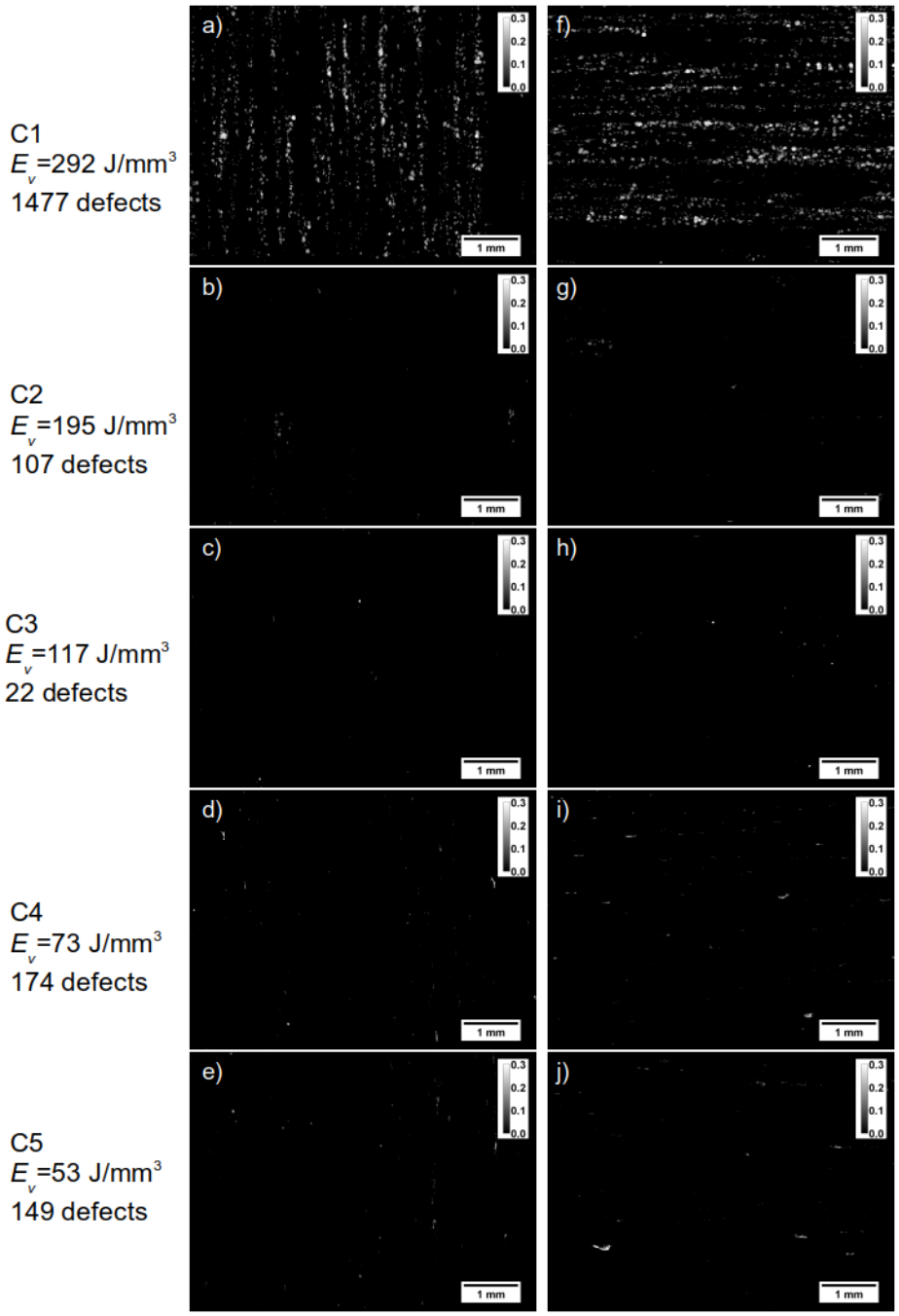

Figure 25: 2D distribution of porosity in LPBF Ti-Al6-V4 produced with different energy density; (a-e) building direction perpendicular to scattering plane; (f-j) building direction within to scattering plane; defects appear aligned with the layers of the production process and minimum number of defects is observed in sample C3; large defects show different shape at high (sample C1) and low (sample C5) energy density

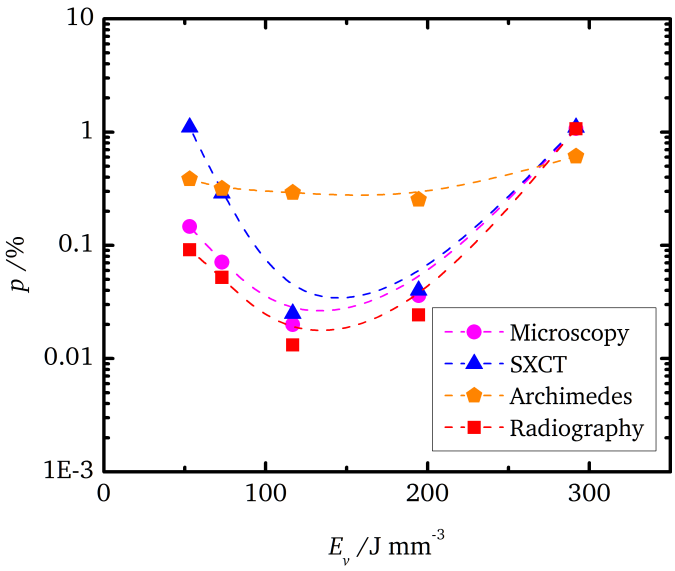

Figure 26: Total porosity p in dependence of volume energy density E_v as determined by optical microscopy, SXCT, X-ray radiography, and Archimedes weighing

Specific surface analysis Figure 27 shows maps of the relative specific surface $\frac{C}{\mu}$ of each sample and both orientations. The minimum amount of defects is observed in sample C3 (117 J mm^{-3}), which is consistent with the observations from the porosity maps and total porosity analysis. Comparing the maps of $\frac{C}{\mu}$ to the porosity maps shows that the amount of defects detected by SXRR is higher for all samples except for sample C2. However, in samples C1 and C2 (produced at high energy densities) the difference is small and not statistically significant. A significant difference is only observed at lower energy densities, i.e., samples C3, C4, and C5. Moreover, there is a significant difference between the two orientations in the SXRR radiographs. When measured with the building direction laying within the scattering plane significantly more defects are detected. This indicates a preferred orientation of the defects parallel to the layers of production. In contrast, at high energy densities, i.e. sample C1, no difference between the two orientations is observed. Sample C4 has significantly more defects than sample C5, which is counterintuitive as sample C5 has higher porosity. This, however, can be explained by the larger sizes of the individual defects in sample C5 and possible agglomeration of several defects or an overlap of several defects at different depths of the sample in the projection.

Qualitatively, the different defect types can be recognized from their appearance and shape. The different morphologies of the defect types is already reported in literature, e.g., [95], and was, additionally, verified by high resolution SXCT measurements of small sections of samples C1 and C5. Figure 28 shows enlarged details of the $\frac{C}{\mu}$ maps together with a 3D rendering of the defects marked I-IV as obtained from the SXCT measurements.

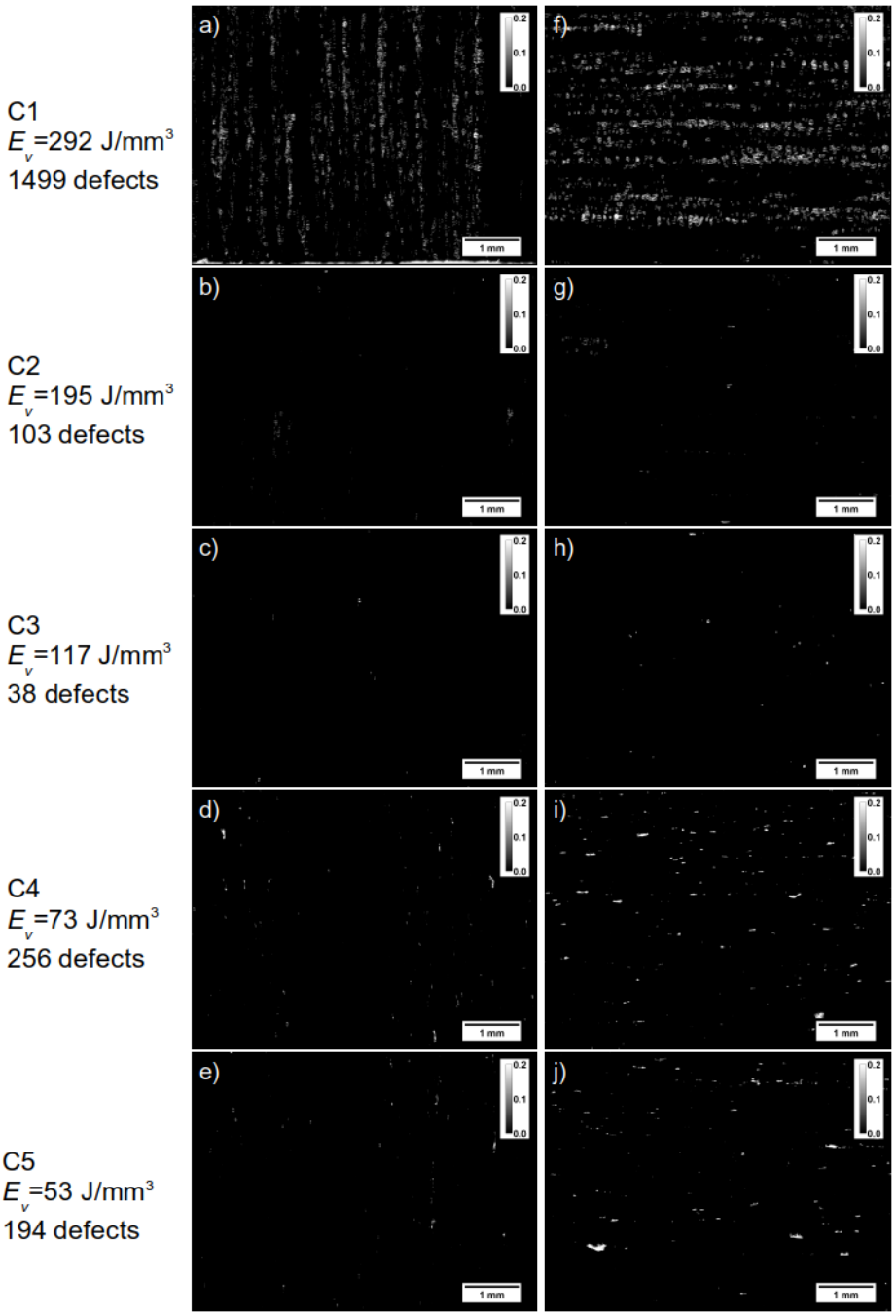

Figure 27: Synchrotron X-ray refraction radiographs of LPBF Ti-Al6-V4 produced with different energy density; (a-e) building direction perpendicular to scattering plane; (f-j) building direction parallel to scattering plane; defects appear aligned with the layers of the production process and minimum number of defects is observed in sample C3; at low energy densities (samples C4 and C5) there is a significant difference in the number of detected defects in the two orientations

Binding defects (Figure 28a and b), which are predominant at lower energy densities, appear as solid areas with high values of $\frac{C}{\mu}$. Furthermore, the difference between the two orientations is apparent and can be explained by the preferred orientation of the surfaces observed in the SXCT measurement. From the 3D renderings (Figure 28I to III) it is observed that these defects are crack-like cavities, which appear to be voids between approximately spherical objects (i.e., unprocessed powder particles) and balling effects. In Figure 28I it is evident that unprocessed powder particles remain within the cavity.

Keyhole pores (Figure 28c and d), which are predominant at higher energy densities, appear as crescent shapes. These crescent shapes originate from the refraction at the edges of the round pores and the sensitivity to surface orientation causes only the surfaces perpendicular to the scattering plane to appear in the images. In the center of the pore the refraction signal is low, because there is no internal structure which could cause refraction. Also there is no significant difference between $\frac{C}{\mu}$ in the two orientation except for the orientation of the crescent shapes.

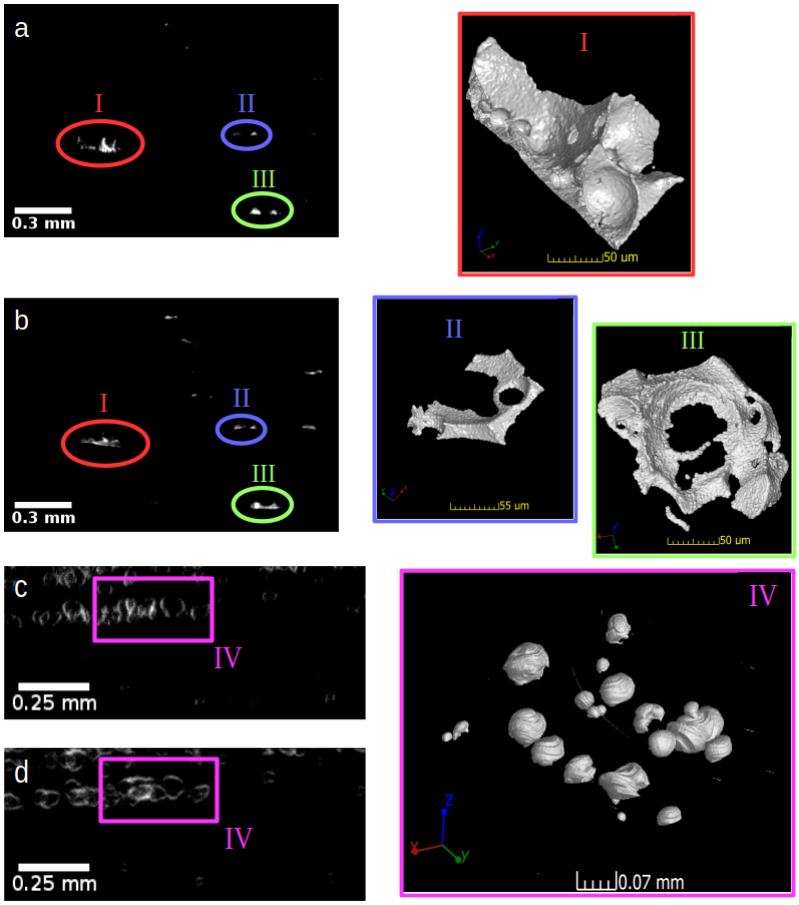

Figure 28: SXRR radiographs of sample C5 imaged in perpendicular orientation (a) and parallel orientation (b) and of sample C1 imaged in perpendicular orientation (c) and parallel orientation (d); 3D renderings of the respective defects marked in the SXRR radiographs (I-IV)

For a quantitative analysis the defects in the SXRR radiographs have been segmented by means of a global threshold and the individual mean values of $\frac{C}{\mu}$ for each defect have been determined. Figure 29 shows the mean value over all segmented defects of $\frac{C}{\mu}$ in dependence of E_v, separately for both sample orientations. At low energy densities the defects show a higher value of $\frac{C}{\mu}$, because the binding defects, which are predominant in this region, exhibit a larger amount of free surfaces. Most importantly, there is a significant difference between the two sample orientations at low energy densities. In parallel orientations, i.e., when the building direction lays within the scattering plane, $\frac{C}{\mu}$ is increased, meaning that the surfaces are mostly aligned parallel to the layers of production. Increasing the energy density leads to a decrease of $\frac{C}{\mu}$ and the difference between the two orientations becomes smaller. This means that with increasing energy density the proportion of spherical keyhole pores increases. At high energy densities,

where keyhole pores are the predominant defect, $\frac{C}{\mu}$ is roughly the same for the two orientations as would be expected for spherical voids. The increase of $\frac{C}{\mu}$ in sample C1 with $E_v = 292\,\mathrm{J\,mm^{-3}}$ can be explained by its high defect density. As evident from Figure 27a and f the individual defects in different depths overlap in the projection and cannot be segmented from each other.

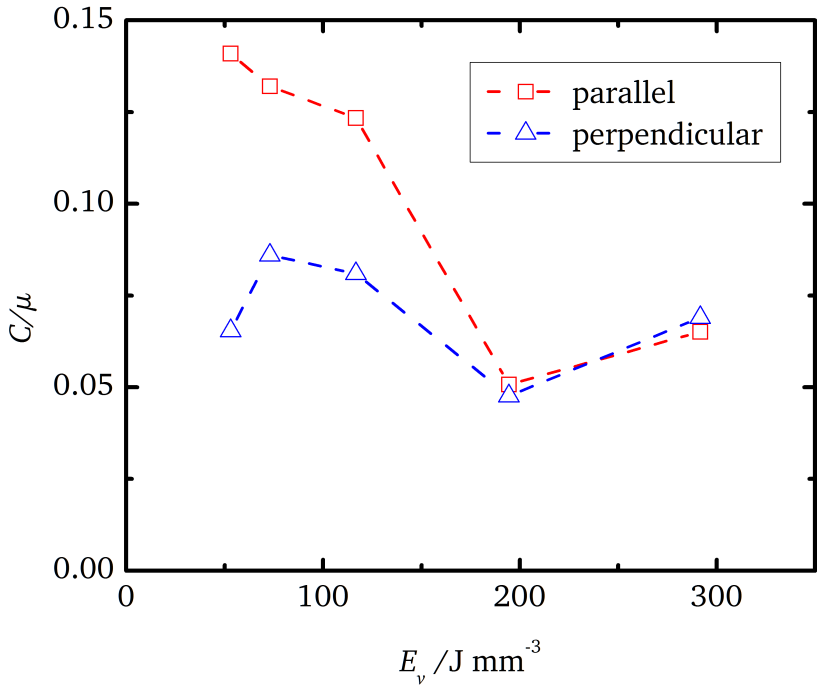

Figure 29: Mean refraction value $\frac{C}{\mu}$ of segmetned defects in dependence of volume energy density for both orientations

Classification of defects To quantify the fraction of each type of defect in dependence of energy density it is necessary to classify the detected defects into keyhole pores and binding defects. Thus, process parameters could be optimized to minimize binding defects.

Based on the results presented so far, $\frac{C}{\mu}$ can be used to make this distinction, even when the shape of the defects cannot be discerned due to limited image resolution. As indicator for this distinction the ratio ζ between the two sample orientations was chosen.

$$\zeta = \frac{\left(\frac{C}{\mu}\right)_{\text{perpendicular}}}{\left(\frac{C}{\mu}\right)_{\text{parallel}}} \tag{14}$$

ζ was calculated this way to avoid division by zero, since many defects, especially binding defects, appear only in the parallel orientation. To evaluate ζ as potential quantity

to distinguish both types of defects, ζ was calculated for each segmented defect in samples C1 and C5. These samples were chosen because they represent the extreme cases in terms of high and low volume energy density of all samples prepared for this case study. Therefore, it can be assumed that the defects present in the respective sample are almost entirely keyhole pores, in sample C1, or binding defects, in sample C5. Frequency histograms, representing the amount of defects in dependence of ζ, were created and are presented in Figure 30. The histogram of sample C1 shows a well defined peak centered at $\zeta = 0.58$ as determined by fitting of a Pearson Type VII distribution to the histogram. The peak of sample C5 is less pronounced due to the fact that there are much less defects present than in sample C1. However, it is still possible to also fit a Pearson Type VII distribution to this histogram which is centered at $\zeta = 0.02$. The Pearson Type VII distribution is chosen because it matched the given data most accurately. To use ζ as measure for classification of the defect types a threshold value ζ_{thr} is defined. If $\zeta > \zeta_{\text{thr}}$ the respective defect is classified as keyhole pore, and if $\zeta < \zeta_{\text{thr}}$ it is classified as binding defect. From the histograms of samples C1 and C5 the threshold was determined as the value half way between both peaks, i.e., $\zeta_{\text{thr}} = 0.3$.

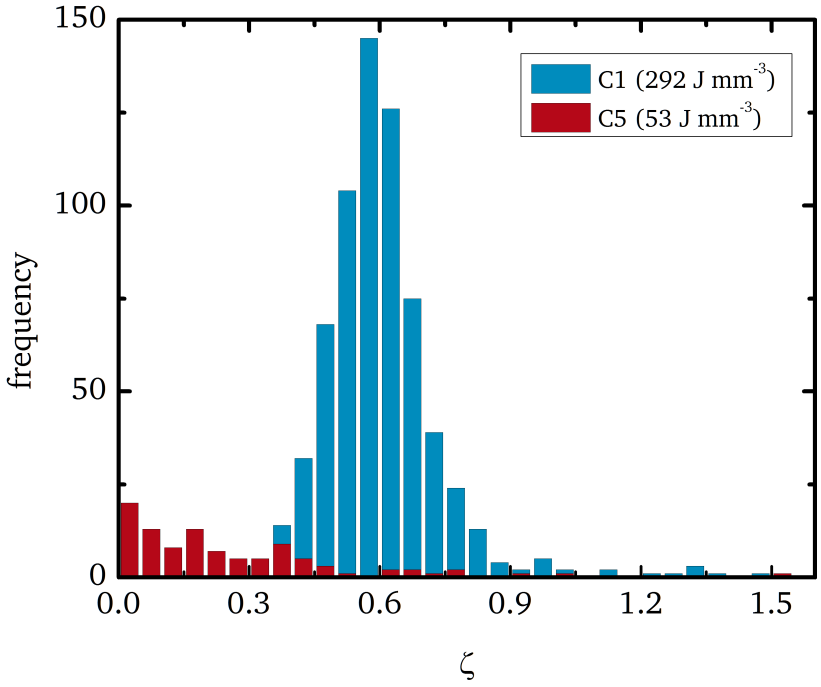

Figure 30: Frequency histograms of the ratio ζ of samples C1 and C5

To corroborate the meaningfulness of the threshold value it was used to classify the defects in a third sample, namely C2. The result is presented in Figure 31, which shows the sum of $\frac{C}{\mu}$ from both sample orientations with each defect marked according to the classification result. To evaluate the quality of the classification the result is compared to a classification according to the defect shape. In the investigated area of the sample a

total of 68 defects are identified, of which 19 are too small to evaluate their shape. Of the remaining 49 defects, on which both classifications are performed only three are classified incorrectly by means of ζ_{thr}. That represents a total of 6 % false classifications. The total amount of defects for this analysis is smaller than for the entire sample because only the overlapping area of the two sample orientations is regarded.

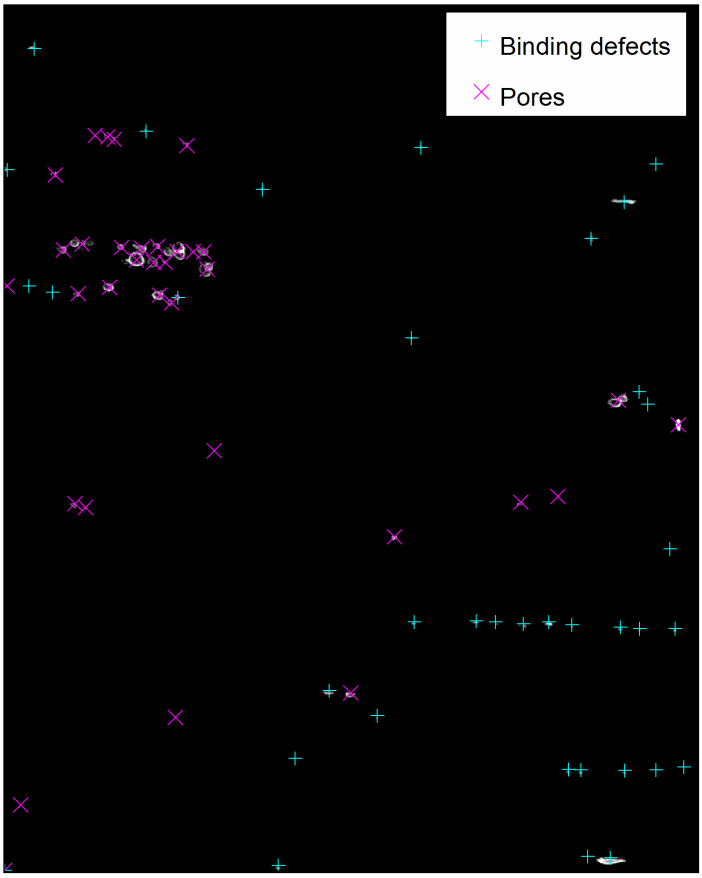

Figure 31: SXRR radiograph representing the sum of the refraction value $\frac{C}{\mu}$ in both orientations of sample C2 with defects classified into binding defects and keyhole pores using $\zeta_{\text{thr}} = 0.3$

As result of the classification sample C2 contains 39 binding defects and 29 pores. Thus, binding defects still form the majority of defects although the sample was produced with a volume energy density in the vicinity of the upper limit of the optimum range. Since binding defects are more detrimental to mechanical properties [91], it may be worth considering to produce parts at volume energy densities above the upper limit for minimum porosity. While this introduces higher total porosity, the morphology of the cavities would be more favorable.

4.3.4 Conclusions

In this case study SXRR was successfully applied to the analysis of porosity in additively manufactured Ti-Al6-V4. The necessary increase of the photon energy and, therefore, smaller refraction angles did not compromise the measurements. The obtained refraction values of the defects are, on average, in the same range as in the previous two case studies (Al and MMC), i.e. $\frac{C}{\mu} \approx 0.1$, at roughly the same noise level. Therefore, no significant decrease in contrast is observed. However, the contrast is generally reduced for smaller defects.

It is found that the minimum of porosity, under the chosen production conditions, is achieved at a volume energy density of $E_v \approx 120\,\mathrm{J\,mm^{-3}}$. At the same energy density a minimum amount of defects is observed in the SXRR radiographs.

Furthermore, the different morphology of the defect types causes a difference in their orientation dependency in the SXRR radiographs as verified by a comparison between SXRR and SXCT of the exact same defects. While $\frac{C}{\mu}$ is nearly independent of orientation for keyhole pores, binding defects show an about three times higher value of $\frac{C}{\mu}$ in parallel orientation than in perpendicular orientation. This different orientation dependency was successfully exploited to classify the defects. The proposed classification by using a threshold of the ratio ζ between the refraction values in the two orientations was shown to have an accuracy of 94 % and has been applied to defects whose shape could not be resolved due to limited detector resolution.

The volume of the samples analyzed by SXRR is about 20 times larger than the volume of the samples analyzed by SXCT, thus, providing better statistics, especially since the defects are not necessarily evenly distributed over the sample volume (see Figure 25 and Figure 27).

4.4 Case Study D: Hydrogen assisted cracking in lean-duplex stainless steel

This case study presents SXRR and SXRCT measurements on lean-duplex steel samples to analyze hydrogen assisted cracking (HAC). The task was to identify and locate cracks caused by absorbed hydrogen in combination with tensile load. The experiments were performed in collaboration with department 9.4 Weld Mechanics of the "Bundesanstalt für Materialforschung und -prüfung (BAM)". The colleagues provided the samples and performed the hydrogen charging, tensile tests, carrier gas hot extraction measurements of the hydrogen content as well as fractographic investigations of the samples. The SXRR and SXRCT measurements, their post-processing and data analysis was performed by the author.

4.4.1 Motivation

Materials science aspects Lean-duplex stainless steels are frequently used in the petrochemical and food industry as well as for off-shore applications because of their combination of high corrosion resistance and good mechanical properties. Their microstructure consists of ferrite and austenite phases with typical grain sizes of only a few micrometers. Because austenite is more ductile than ferrite, the load in the ferrite phase increases as the austenite begins to deform plastically under tensile load causing crack initiation in the ferrite phase. These small cracks coalesce through the austenite to form macroscopic cracks, thereby leading to failure.

Hydrogen is well known to cause degradation of mechanical properties in metallic materials, a phenomenon referred to as hydrogen embrittlement [99]. Combined with internal or external stresses HAC can occur which results in brittle fracture of the material at stresses well below the expected ultimate strength of the material. Hydrogen uptake occurs, e.g., during welding or corrosion processes. The mechanisms of hydrogen assisted cracking are not completely understood yet but several theories have been developed [100]. The most accepted ones are hydrogen-enhanced decohesion [101] and hydrogen-enhanced localized plasticity [102]. The diffusion of hydrogen in metals [103–106] as well as the the strains induced by absorbed hydrogen through lattice expansion [107] has been widely studied to gain insights into crack formation. Usually, the crack formation is characterized using fractographic and metallographic methods like scanning or transmission electron microscopy. While these methods already provide a rich source of information it would be important to analyze the three dimensional structure and spatial distribution of the cracks, particularly in the early stages of formation.

X-ray CT has already been applied to the investigation of crack formation. For example, it was used to investigate hot cracks in aluminum welds [108, 109] or the fatigue crack growth in aluminum alloys [110, 111]. Also subsurface stress corrosion cracking in steel has been observed with X-ray CT [112]. However, HAC in lean duplex stainless steels has never been successfully studied with X-ray CT, since the initial cracks are only few micrometers large because of the small grain size of the ferrite phase. Such cracks

are smaller than the spatial resolution of common X-ray CT systems or even SXCT and, therefore, cannot be detected. Thus, in this case study, SXRCT is applied to detect and quantitatively analyze cracks in hydrogen charged lean-duplex stainless steel. The goal was to gain insights into the crack initiation.

Methodological aspects From a methodological point of view the measurement of steel samples poses a challenge for X-ray imaging techniques because of the high X-ray attenuation of steel. Thus, to achieve sufficient transmission a photon energy of 50 keV is need to image even small samples of just 1 to 2 mm in thickness. This is about the highest usable photon energy of BAMline. Compared to the photon energies commonly used for SXRR an SXRCT, i.e., around 20 keV the photon flux density at 50 keV is reduced to less than a third, see Figure 3. This results in longer integration times and noisier images. The maximum usable energy of about 50 keV is also not sufficient to achieve a transmission comparable to those usually aimed for, i.e., about 30 %. Instead only 10 % can be reached resulting in low contrast of features within the sample. Furthermore, the high photon energy causes smaller refraction angles what reduces the contrast further. As an example, for Fe imaged at 50 keV the refraction angles are about 50 % smaller than for Al imaged at 22 keV. This case study will demonstrate that the investigation of steel samples is possible and yields reliable results despite these limitations.

4.4.2 Materials and experimental details

The material used for the SXRCT analysis was the lean duplex steel X2CrMnNiN21-5-1 (1.4162) according to DIN EN 10088-2. Its chemical composition is shown in Table 5 as measured by spark plasma spectroscopy. The microstructure consists of about 50 % ferrite and 50 % austenite and the orientation of these phases with respect to the rolling direction is illustrated in Figure 32a.

Table 5: Chemical composition in wt.-% of the lean duplex steel 1.4162

Cr	Ni	Mo	C	N	Mn	Fe
20.96	1.54	0.183	0.02	0.17	4.88	Balance

For the SXRCT measurements round tensile samples were prepared by turning from a 6 mm thick plate in the as delivered state. The axis of the tensile sample was parallel to the rolling direction. To achieve a suitable X-ray transmission the gauge section of the sample was then machined to a diameter of 1.5 mm by cylindrical grinding. The complete sample geometry is illustrated in Figure 32b.

To generate HAC the samples where electrochemically charged with hydrogen. The process was performed via cathodic charging in a galvanostatic charging cell. There, the tensile sample operates as working electrode (cathode) and a platinum electrode operates as counter electrode (anode). The electrolyte was an aqueous solution containing 0.1 mol H_2SO_4 and 0.05 mol $NaAsO_2$. The sodium arsenite acts as an inhibitor

to prevent the recombination of hydrogen gas on the sample surface. The current density was set to $8\,\mathrm{mA\,cm^{-1}}$ and the samples were charged for 120 h and 170 h to vary the hydrogen concentration in the samples. To prevent desorption of the hydrogen, the samples were stored in liquid nitrogen at $-196\,^{\circ}\mathrm{C}$ immediately after the charging process.

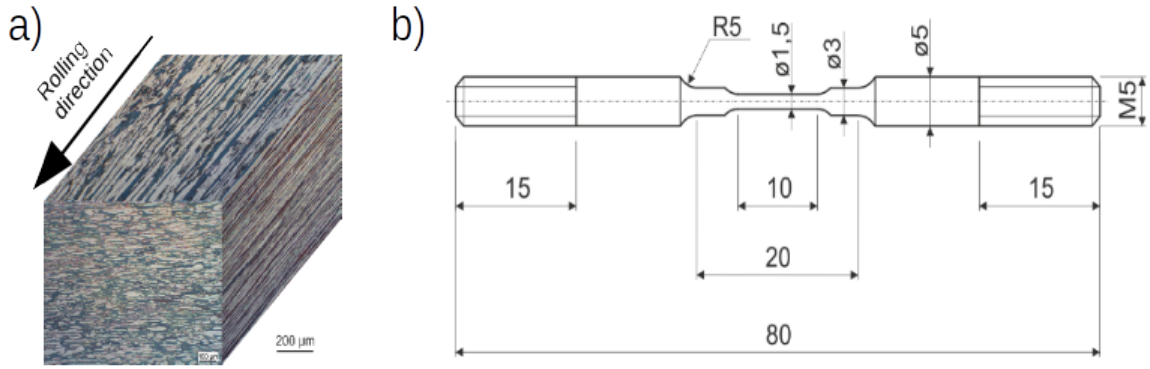

Figure 32: (a) Microstructural orientation of the ferritic phase (dark) and austenitic phase (bright); (b) geometry of the tensile samples, all measures are in mm

For the tensile test the samples were taken out of the liquid nitrogen and defrosted in acetone for 1 min to room temperature. The samples were then pulled at a constant elongation rate of $1.67\,\mathrm{mm\,min^{-1}}$. The tensile tests were performed such that different loading scenarios, i.e., failure, plastic deformation, and elastic deformation, were realized for the different hydrogen charging conditions. To determine the hydrogen concentration of the samples one part of the ruptured samples was stored again in liquid nitrogen, while the other half and other samples were used for SXRCT measurements and further investigations. The hydrogen concentration was determined by carrier gas hot extraction [113, 114]. The fracture surfaces were investigated by scanning electron microscopy (SEM) to distinguish brittle and ductile fracture as well as identify secondary cracks.

Table 6: Summary of the lean-duplex steel samples with their respective hydrogen content and tensile loading state

Sample	Hydrogen charging time /h	Hydrogen concentration /ppm	loading state
D1	170	198	fracture
D2	120	78	fracture
D3	120	78	plastic

The SXRCT measurements were performed as described in Section 3.3.2. The photon energy was set to 50 keV using the DCM and the nominal pixel size was $(3.5\,\mu\mathrm{m})^2$. The

resulting X-ray transmission amounted to just about 10 %. The SXRCT and SXCT measurements were performed with 1800 projections evenly distributed over a full rotation of the sample. An exposure time of 10 s had to be chosen to achieve enough signal, which resulted in a total scanning time of more than 10 h for the SXRCT and SXCT measurement of one sample. The calculated projections representing $C \cdot d$ and $\mu \cdot d$ were reconstructed with the custom FBP algorithm of BAM. Because of the high noise level the volume data was additionally filtered using non-local means denoising [115] prior to analysis. Such a filter smooths the image not by averaging over the immediate neighborhood of a pixel but rather by averaging over all pixels in the entire image with similar neighborhood. The non-local means denoising is considered to preserve edges, textures and other fine details.

4.4.3 Results and Discussion

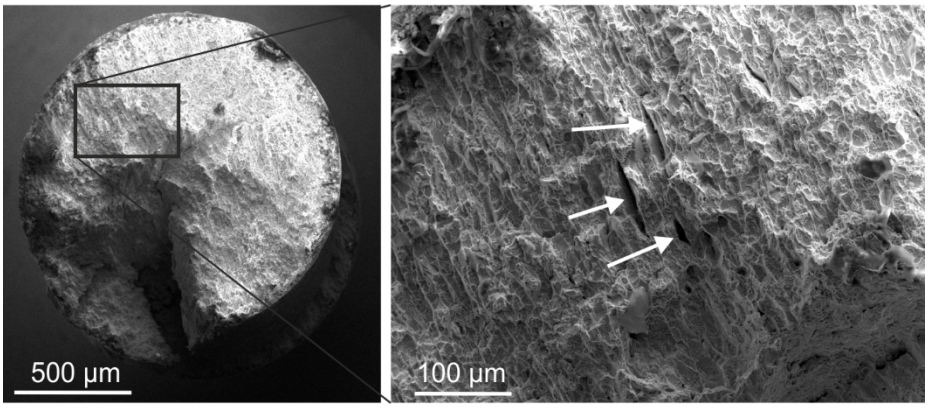

Figure 33: SEM image of fracture surface showing brittle fracture behavior and secondary cracks on the fracture surface (indicated by arrows)

A qualitative comparison between the SXCT, SXRCT and SEM results of sample D1 yields a cross-check of the data quality. SEM images of the fracture surface are presented in Figure 33. The fracture surface shows transcrystalline fracture over the entire cross-section indicating brittle fracture and, thus, hydrogen saturation over the entire sample. Additionally, the sample contains large secondary cracks on the fracture surface indicated by arrows in the enlarged detail of Figure 33. A tomogram and 3D renderings of the SXCT measurement are shown in Figure 34. In the SXCT volume multiple large cracks progressing from the outer surface of the sample are identified, apart from the main crack that caused failure. In close vicinity to these larger cracks, smaller cracks are observed. Also smaller cracks are found propagating from the fracture surface as shown in Figure 34c. The very same secondary cracks shown in the SEM images can be identified in the SXCT volume, see Figure 34b. However, the bulk of sample appears to be free of cracks.

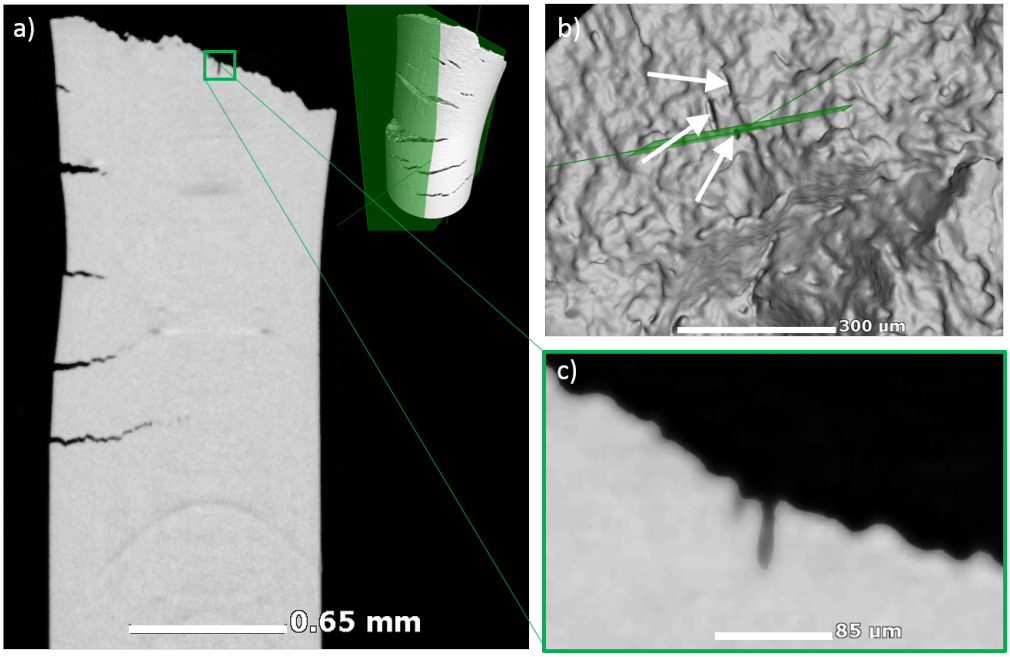

Figure 34: a) Tomogram and 3D rendering of the reconstructed SXCT volume of sample D1. Green plane indicates position of the tomogram b) 3D rendering of the fracture surface, arrows indicate secondary cracks identified in SEM images (see Figure 33) c) enlarged detail of the tomogram showing the secondary crack extending from the fracture surface

The SXRCT measurement shows similar results, although the secondary cracks at the fracture surface cannot be identified. This is because they have the wrong orientation with respect to the scattering plane to be detected. Also, the fracture surface is represented in less details than in the SEM or the SXCT images. The roughness of the fracture surface causes an overall high refraction value. Therefore, small secondary cracks cannot be distiguished in close the vicinity to the fracture surface. However, around the perimeter of the sample small areas with high refraction value are revealed in the SXRCT measurement which are not visible in the SXCT measurement (see Figure 35). These areas correspond either to cracks or blistering, i.e., the formation of hydrogen gas just below the surface of the sample during the charging process creating small hydrogen filled pores. Also small subsurface cracks are identified beneath the fracture surface, which were not detected in the SXCT scan. The bulk of the sample, however, appears to be free of cracks just as in the SXCT measurement.

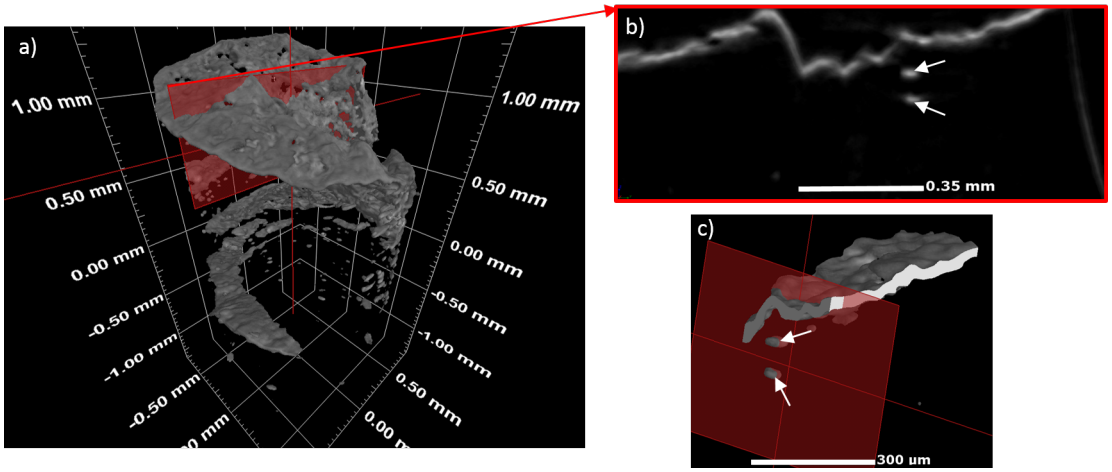

Figure 35: 3D rendering of the reconstructed SXRCT volume of sample D1 (a) with tomogram taken at the position indicated by the red plane (b) and an enlarged detail of the 3D rendering. Arrows indicate small cracks beneath the fracture surface.

Similar observations are made for samples D2 and D3. Figure 37 shows projections of the SXCT and SXRCT volume of the two samples along the center axis, i.e., the direction of the applied tensile load. This visualizes the location of cracks with respect to the outer perimeter of the samples and includes all cracks easily recognized in the volumes. There remain few ring artifacts caused by defects in the scintillator which could not be removed without also removing cracks. In both samples the cracks are predominantly located at the outer perimeter of the sample. Between plastic deformation and fracture only those cracks which are close to the outer perimeter of the sample grow significantly while small cracks in the bulk of the sample remain largely unaffected by the applied load. SEM measurements of the fracture surface, presented in Figure 36, show that sample D2 exhibits brittle fracture only at the periphery of the sample while in the center a ductile fracture behavior is observed. Thus, samples D2 and D3 are not saturated with hydrogen over the entire cross-section. This explains the observations made by SXCT and SXRCT that cracks grow only at the outer perimeter of the sample as cracks grow predominantly in the brittle areas. Visual comparison of the SXCT and SXRCT measurement in Figure 37 reveals that more cracks are detected in the SXRCT volume. When segmenting the defects a total of 373 and 602 cracks are found in the SXRCT volumes of samples D2 and D3, respectively, while the respective SXCT volumes show only 74 and 159 defects. Thus, a higher sensitivity of SXRCT to small cracks is also observed in these measurements.

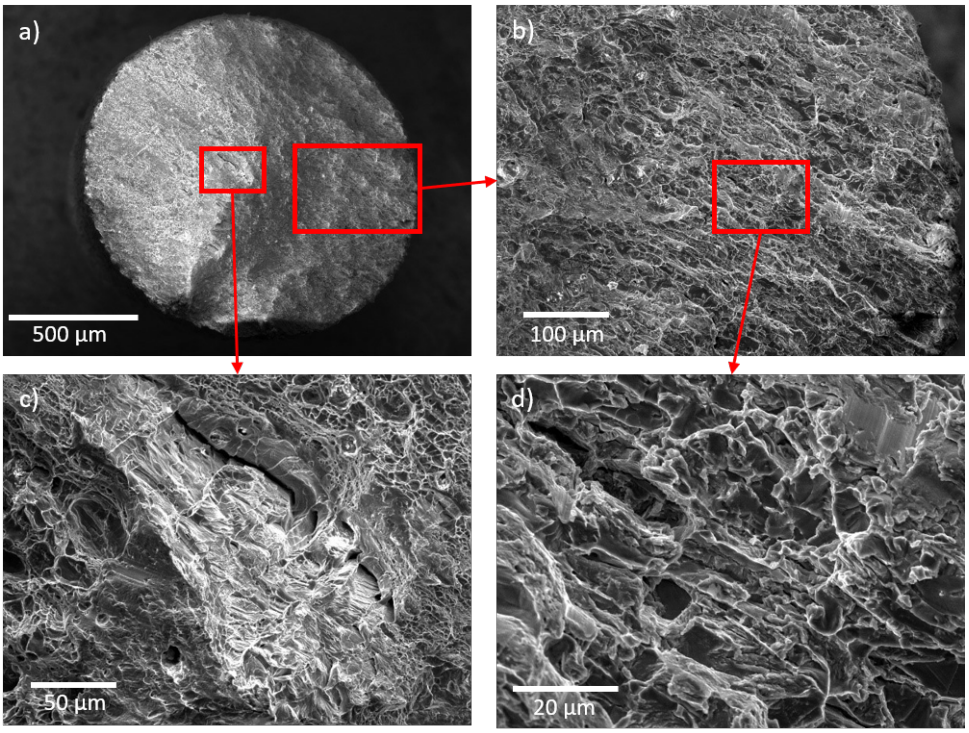

Figure 36: SEM imges of the fracture surface of sample D2; a) overview of the whole fracture surface; b) detail taken close to the perimeter; d) further detail of subfigure b) showing brittle transcrtaline fracture; c) detail taken from the center showing webbed structure typical for ductile fracture

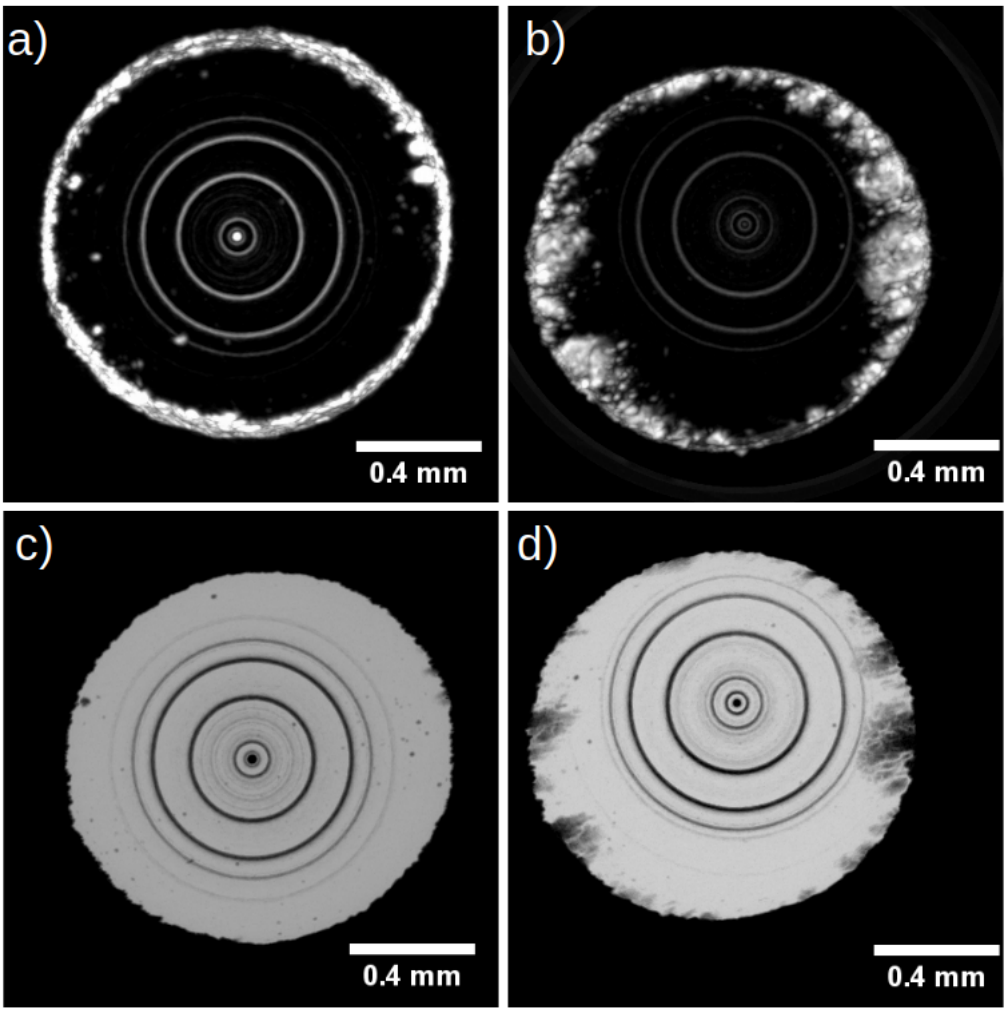

Figure 37: Projections along the center axis of the SXRCT volumes of samples D2 (a) and D3 (b) as well as respective projections of the SXCT volumes of samples D2 (c) and D3 (d); concentrical circles are ring artifacts originating from the monochromator, analyser crystal, and scintillator screen

On samples D2 and D3 a quantitative analysis of the crack sizes and the location of the cracks with respect to the outer perimeter of the same was performed in the SXRCT volumes. The crack size was evaluated as the diameter of the smallest sphere that contains the entire crack. This is equivalent to the largest extension of the crack in any arbitrary direction. It is, therefore, considered a measure of the crack length. The location was determined as the distance between the outer surface of the sample and the point of the crack closest to this outer surface. This is considered a measure for the depth in which the crack lays. Frequency histograms of both measures for samples D2 and D3 are presented in Figure 38. The histograms show that the size of the majority

of cracks does not change significantly between the two loading states of samples D2 and D3. To compare the crack sizes occuring with highest frequency the mode of the histrogramms presented in Figure 38a and b is analysed which is about 25 µm in both samples. Only the number of cracks increases significantly with increasing tensile load. However, in sample D3 several cracks are observed with crack sizes larger 100 µm and up to 300 µm, which are not observed in sample D2. The depth at which the cracks occur shifts slightly to larger depths in sample D3. In sample D2 most cracks occur within 20 µm from the outer perimeter of the sample with very few occurrences at depth larger 40 µm. In sample D3, however, a significant number of cracks occur at depths of up to 120 µm. In the center of both samples, i.e., depths of about 500 µm, there are almost no cracks detected by SXRCT.

Thus, the major portion of the damage in samples D2 and D3 is located cose to the outer perimeter of the samples. This can be explained by the hydrogen charging procedure. During the electrochemical charging the hydrogen is absorbed at the surface of the sample and then diffuses further inwards. Therefore, there is a gradient in the hydrogen concentration along the depth of the sample, unless it is charged to saturation. As the SEM analysis showed ductile fracture at the center of samples D3, the hydrogen content does not saturate in samples D2 and D3. Thus, these samples are more susceptible to HAC at the perimeter and cracks will occur predominantly in this region. The major amount of damage observed by SXRCT arises shortly before failure. The plastically deformed sample shows relatively little damage compared to the damage observed after failure.

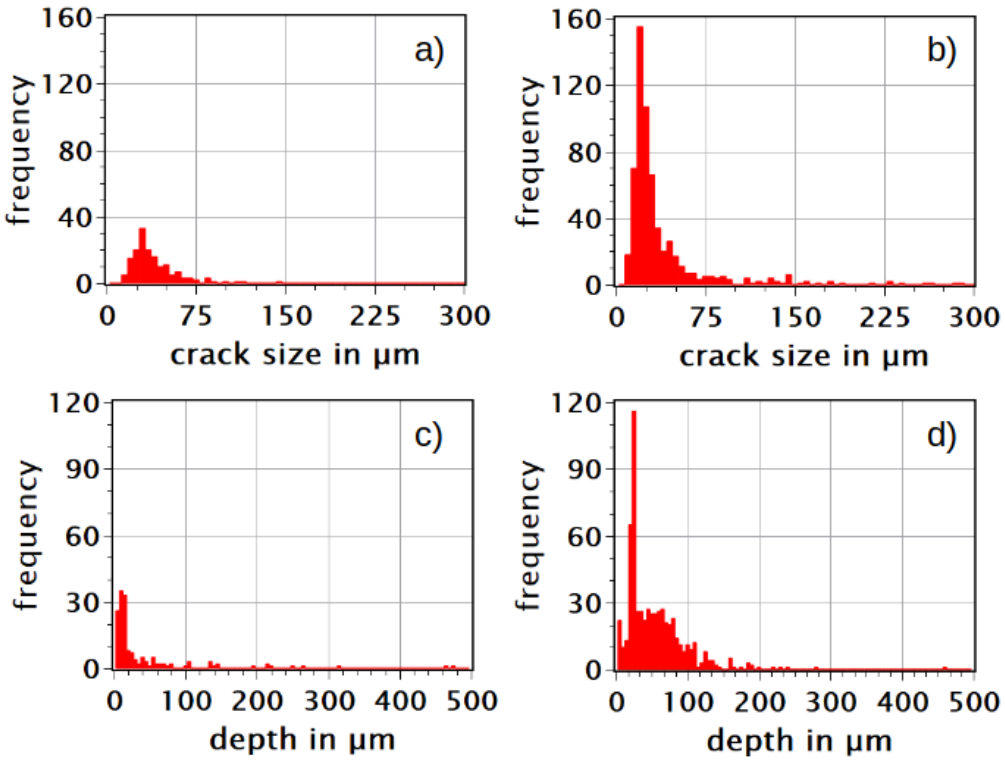

Figure 38: Frequency histograms showing the distribution of crack sizes in samples D2 (a) and sample D3 (b) and the distribution of the depth in which the cracks occur in samples D2 (c) and D3 (d) as obtained from SXRCT measurements

4.4.4 Conclusions

In this case study SXRCT was successfully applied to the quantitative analysis of HAC in lean-duplex stainless steel. It was shown that SXRCT measurements of steel objects are in principle possible with the imaging setup at BAMline. However, this requires to use the beamline at its upper photon energy limit. The low photon flux density at high photon energies cause increased noise in the projection images and the scanning times to increase significantly. The smaller refraction angles reduce the contrast complicating the detection of small features. Nevertheless, SXRCT was capable of detecting significantly more cracks than the SXCT measurement with the same spatial resolution indicating that the higher sensitivity to small defects is maintained. The small isolated cracks in the ferrite phase with sizes of only few micrometers could not be detected. In fact no defects smaller than 10 µm are detected. This is likely due to the low contrast, high noise and necessary filtering of the data.

The SXRCT measurements revealed that HAC occurs predominantly at the edges of

the samples. This behavior is attributed to the setup of the hydrogen charging process which induces a gradient in the hydrogen concentration over the depth of the samples. Secondary cracks as observed in SEM investigations were only identified in close vicinity of larger cracks but not in the bulk of the samples. This shows that a full 3D analysis of the crack distribution is necessary for the evaluation of crack initiation and growth, since a 2D analysis might lead to wrong conclusions about the crack generation in the bulk of the sample. Furthermore, it was shown that the major portion of the damage is induced shortly before failure.

4.5 Summary and general discussion

The four case studies demonstrate how SXRR and SXRCT are applied to the analysis of metallic materials and build on the published applications of the two methods.

In case study A, the capability of SXRR and SXRCT to detect finer cracks compared to X-ray radiography and SXCT is demonstrated on a coupon from an aluminum weld seam. The coupon was measured under imaging conditions similar to those used, e.g., in [53, 55]. Consequently the achieved image quality is similar. However, the focus here is on the detection of individual cracks rather than areas of high microcrack density. In [53–55] the refraction value is statistically analyzed over the whole sample while in case study A the cracks are segmented and the precision of this segmentation is analyzed. Further, a quantitative gray value analysis of two volumes representing i) the quantity $C + \mu$ obtained from reconstructing the SXRCT projections alone and ii) the quantity C obtained from reconstructing $C \cdot d$ projections is performed. The analysis verified the model for the computation of the refraction value for synchrotron applications. While the respective formula (Eq. 10) was used before, its derivation was first published in the publication of case study B [72] and an experimental validation of this model was not published before. The case study also demonstrates the feasibility of reconstructing the 3D distribution C from SXRCT measurements. This approach is new for the processing of SXRCT data. In previously published applications of SXRCT [51, 52] the SXRCT projections were reconstructed without extracting the refraction value C. Especially in [52] the SXRCT data can only be interpreted in direct comparison to the SXCT data because the sample contains Fe-rich inclusions. Without the help of the SXCT data these inclusions cannot be distinguished from cracks or pores yielding a high refraction value. The approach proposed here supersedes such a direct comparison as the high density parts do not appear in the reconstruction of C, thus, enabling quantitative evaluation of the inner surfaces in 3D.

Case study B builds on the findings of case study A and extends the application of SXRR to *in-situ* measurements on a particle reinforced MMC. As in case study A, the material under investigation is aluminum based and, hence, a similar photon energy is used and similar image quality is reached. The *in-situ* SXRR measurements are evaluated analyzing the mean value of C over the whole sample area in dependency of the applied tensile load. The observation, i.e., a non-linear increase of inner surfaces for stresses over the yield strength of the material, is consistent with *in-situ* CT measurements, e.g. [74], where the amount of cracked particles was analyzed. However, for the

material used in case study B such an analysis would not be feasible. Automatic crack detection tools would be required because of the small size and large number of particles, but such tools are not reliable in the case of cracks with sizes close to the spatial resolution, especially in multi-phase materials. Also the design of an *in-situ* test rig can be much simpler than for *in-situ* CT as no sample rotation is required. Therefore, the added value of *in-situ* SXRR measurements is to enable the analysis of damage evolution in such materials with less experimental and computational effort. Further, in case study B SXRCT and SXCT measurements are compared demonstrating that SXRCT detects cracks which can not be discerned in SXCT data with a seven times better spatial resolution. For the evaluation of the SXRCT measurement the approach of reconstructing C, introduced in case study A, is successfully applied.

In case study C, porosity in LPBF Ti-Al6-V4 is analyzed by SXRR. Here, a stronger absorbing material is investigated compared to case studies A and B requiring a higher photon energy of 30 keV. Such photon energies were used before, e.g., in [54], but the focus of this publication was on microcrack densities by statistically analyzing the refraction value over the sample area. In case study C, the defects are segmented as in case study A and, thus, the analysis is more susceptible to noise. While the SXRR radiographs show higher noise compared to case study A, as is expected due to the higher photon energy, this is found to be not yet detrimental to the segmentation. The refraction value is analyzed for each segmented defect in dependency of the sample orientation and used to classify defects into keyhole pores and binding defects. The existence of these two defect types, their morphology and preferential occurrence in dependency of the laser energy density is well documented in literature [95–98]. Traditionally the defects are analyzed by means of optical microscopy or CT. Because of the high resolution needed to reliably find the defects and evaluate their morphology, both methods require more experimental effort to gain statistical information. For example, in [95] 100 optical micrographs were taken at three different depths to analyze a sample of the same size as those analyzed in one SXRR radiograph. Thus, case study C presents SXRR as valuable tool to readily gain information about the distribution of the two defect types in materials produced by LPBF as well as demonstrates that titanium as slightly higher attenuating metal can be quantitatively analyzed by SXRR. While a titanium based material was already investigated in [51] the cracks found there were rather large compared to the defects investigated in case study C. Further, in [51] no quantitative analysis of the cracks was performed.

Case study D explores the limits of SXRCT by investigating steel samples. Steel because of its high X-ray attenuation requires much higher photon energies than aluminum or titanium. The used photon energy of 50 keV is the upper limit of the usable range at BAMline. The achieved transmission of 10 % is much lower than the 30 % usually aimed for and, thus, an even higher photon energy would have been preferable. While the usage of 50 keV photons comes with certain limitations, i.e., low photon flux density and smaller field-of-view, it was used before with good results [51]. However, in [51] the material under investigation was titanium and the usual level of transmission was achieved. Therefore, the images obtained in case study D contain significantly more noise than in the three previous case studies, mainly because of the low transmis-

sion. This high noise demands additional filtering of the data, especially since the data is again analyzed by segmenting the defects. However, the filtering is likely to remove very small defects although a texture preserving filter is applied. This is most likely the reason that no cracks smaller than 10 µm are detected. However, a quantitative analysis of the cracks is performed and SXRCT is able to still find smaller defects than a comparable SXCT measurement, which also suffers from the low transmission. The focus of case study D is the 3D distribution of cracks and, therefore, only SXRCT is applied using the same reconstruction procedure established in case studies A and B.

Comparing SXRR and SXRCT to the published research on DEI (Section 2.2) shows that the evaluation of the refraction value as measure for the inner surfaces of a material is unique and similar evaluations are not pursued by other research groups. The original evaluation of DEI, which is the most widely used, is concerned only with the refraction angle [3]. Therefore, DEI mostly improves the visibility of edges between different materials and is best applied to the imaging of weakly absorbing materials and not for the detection of sub-resolution features. SXRR and SXRCT focus on the evaluation of what is referred to as USAXS in the literature concerning DEI, i.e., a broadening of the rocking curve due to multiple refraction at sub-resolution features. While the research on DEI addressed USAXS by developing methods to extract it from the DEI measurement [19, 21, 22, 26] and presenting a model for its physical origin [20], the link between the measured effect and the physical origin was not pursued. The reason for this is most likely the envisioned application of DEI in medical diagnostics where the improvement of image contrast is much more important than the precise quantification of physical properties. However, for materials science applications this quantification is essential and such a link is given for SXRR and SXRCT allowing to quantitatively analyze the physical properties of materials.

5 Conclusion

In conclusion, the X-ray refraction based imaging methods of SXRR and SXRCT are well suited for investigating metallic materials. In four case studies, both methods are successfully applied to quantitatively analyze porosity and cracking in different types of metallic materials. The quality of the obtained results, with the exception of case study D, is similar to those achieved with light-weight ceramic or plastic materials, i.e., the established fields of application for SXRR and SXRCT. The most important challenge to the application of SXRR and SXRCT to metallic materials, identified in this work, is the necessity to use higher photon energies. This results generally in smaller refraction angles caused by the inner surfaces of the sample and lower photon flux density of the X-ray beam. These effects decrease the contrast and increase the noise of the images, respectively. However, in case studies A, B, and C no decrease in the detectability of defects smaller than the spatial resolution of the images is observed. Only in case study D a size limit for the detectable defects is observed.

In case study A, the capability of SXRR and SXRCT to detect finer cracks compared to X-ray radiography and SXCT is demonstrated on a coupon from an aluminum weld seam. In the SXRR radiograph cracks, undetected in the respective X-ray radiograph, are segmented showing the reliabilty of segmentation. A similar evaluation of the SXRCT data is performed with the same result, thus, verifying the detection of sub-resolution features by SXRR and SXRCT. Further, a quantitative gray value analysis verifies the model for the computation of the refraction value for synchrotron applications and proves that the proposed procedure to register the SXRCT and SXCT scans to each other is sufficiently accurate to not blurr edges or introduce artifacts.

Case study B, demonstrates the same capabilities for crack detection in a multi-phase material under similar imaging conditions. The size of the detected defects is additionally analyzed by comparison to an SXCT measurement with a seven times better spatial resolution. It is shown that the SXRCT measurement reveals defects not detected in the high resolution SXCT measurement. Further, SXRR measurements under *in-situ* tensile load were successfully performed and the damage evolution with applied tensile load is analyzed quantitatively showing a non-linear increase of damage for stresses above the yield strength. The accuracy of the SXRR measurements within one *in-situ* measurements series and the repeatability between measurement series are both shown to be about 10 % without applying any corrections and are reduced to less than 3 % by normalization to a reference area.

In case study C, SXRR is successfully applied to analyze porosity in additively manufactured Ti-Al6-V4. The higher sensitivity to very small defects is again demonstrated. The SXRR radiographs respond differently to the two defect types predominant on either side of the optimum energy density range, i.e., i) keyhole pores at higher energy densities and ii) binding defects at lower energy densities. These different responses are linked to the morphology of the defects by comparing SXRR radiographs to high-resolution SXCT measurements. Further, an analysis strategy is devised which exploits the different responses to classify the detected defects into the two types with a precision of 94 % even when the shape of the defect cannot be discerned in the image.

Case study D presents the application of SXRCT to the analysis of hydrogen assisted cracking in lean-duplex stainless steel. This requires the beamline to be operated at the upper limit of the usable photon energy range, i.e., 50 keV. Therefore, the refraction angles and photon flux are reduced significantly causing reduced contrast and increased noise. In this case small defects ($< 10\,\mu m$) are obscured by the required additional filtering. However, SXRCT still proves to be more sensitive to smaller defects than SXCT because SXRCT detects defects which are not visible in the SXCT volume. Despite the poorer image quality the amount, size, and location of the cracks are analyzed quantitatively.

All case studies demonstrate that SXRR and SXRCT are complementary to X-ray radiography and SXCT. The advantage of SXRR and SXRCT is the detection of very small defects which cannot be resolved in X-ray radiography and SXCT due to limited spatial resolution. To be precise, SXRR and SXRCT also cannot actually resolve these defects. Both techniques rather detect a signal caused by the surfaces of the defect and quantitative analysis of this signal yields information about the total amount of surface. But the actual shape of the defect cannot be analyzed, although in some cases the orientation dependency can be used to gain a general perception about the shape. For detailed information about the defect morphology SXCT is a more suitable method. Thus, the combined application of SXRR and SXRCT as well as SXCT yields a comprehensive understanding of defects in materials providing information about morphology, size, amount, and location in samples of different scale.

With regard to metallic materials no fundamental obstacle for the application of SXRR and SXRCT is found in this work. The reduced refraction angles at higher photon energies proved to have little impact on the precision of the measurement. It remains only the rather trivial limitation that the sample must allow for sufficient X-ray transmission which is common to all X-ray imaging techniques and applies to all materials in much the same way.

List of Figures

List of Tables

References

(1) Cloetens, P.; Pateyron-Salomé, M.; Buffière, J. Y.; Peix, G.; Baruchel, J.; Peyrin, F.; Schlenker, M. *Journal of Applied Physics* **1997**, *81*, 5878–5886.

(2) Pfeiffer, F.; Weitkamp, T.; Bunk, O.; David, C. *Nature Physics* **2006**, *2*, 258–261.

(3) Chapman, D; Thomlinson, W; Johnston, R. E.; Washburn, D; Pisano, E; GmÃŒr, N; Zhong, Z; Menk, R; Arfelli, F; Sayers, D *Physics in Medicine & Biology* **1997**, *42*, 2015.

(4) Lider, V. V.; Kovalchuk, M. V. *Crystallography Reports* **2013**, *58*, 769–787.

(5) Hentschel, M. P.; Hosemann, R.; Lange, A.; Uther, B.; Brückner, R. *Acta Crystallographica Section A* **1987**, *43*, 506–513.

(6) Compton, A. H.; Allison, S. K., *X-rays in Theory and Experiment*; Van Nostrand: 1935.

(7) Hentschel, M. P.; Harbich, K.-W. *Materials Testing* **1993**, *35*, 63–67.

(8) Hentschel, M. P.; Ekenhorst, D.; Harbich, K.-W.; Lange, A.; Schors, J. In *Nondestructive Characterization of Materials VIII*, Green, R. E. J., Ed.; Springer US: 1998; Chapter New X-Ray Refractography for Nondestructive Evaluation of Advanced Materials, pp 409–416.

(9) Fensch-Kleemann, F. E.; Harbich, K.-W.; Hentschel, M. P. *Ceramic Forum International* **2002**, *79*, E35–E38.

(10) Hampe, A.; Harbich, K.-W.; Hentschel, M. P.; Rudolph, H.-V. In *ICCM-12 Europe*, Paris, France, 1999; Chapter The Determination of Inner Surfaces in Composites by X-Ray Refraction.

(11) Harbich, K. W.; Hentschel, M. P.; Schors, J. *NDT & E International* **2001**, *34*, 297–302.

(12) Harbich, K. W.; Klobes, P.; Hentschel, M. P. *Colloids and Surfaces A: Physicochemical and Engineering Aspects* **2004**, *241*, 225–229.

(13) Tzschichholz, G.; Steinborn, G.; Hentschel, M. P.; Lange, A.; Klobes, P. *Journal of Porous Materials* **2011**, *18*, 83–88.

(14) Erdmann, M.; Kupsch, A.; Müller, B. R.; Hentschel, M. P.; Niebergall, U.; Boehning, M.; Bruno, G. *Journal of Materials Science* **2019**, *54*, 11739–11755.

(15) Trappe, V; Hentschel, M; Ivers, H In *Testing, Reliability, and Application of Micro- and Nano-Material Systems III*, 2005; Vol. 5766, 15–24.

(16) Trappe, V.; Harbich, K. W. *International Journal of Fatigue* **2006**, *28*, 1187–1196.

(17) Grasse, F.; Trappe, V.; Hickmann, S.; Meister, O. *International Journal of Fatigue* **2010**, *32*, 94–99.

(18) Chapman, D.; Thomlinson, W.; Arfelli, F.; Gmür, N.; Zhong, Z.; Menk, R.; Johnson, R. E.; Washburn, D.; Pisano, E.; Sayers, D. *Review of Scientific Instruments* **1996**, *67*, 3360–3360.

(19) Wernick, M. N.; Wirjadi, O.; Chapman, D.; Zhong, Z.; Galatsanos, N. P.; Yang, Y. Y.; Brankov, J. G.; Oltulu, O.; Anastasio, M. A.; Muehleman, C. *Physics in Medicine and Biology* **2003**, *48*, 3875–3895.

(20) Khelashvili, G.; Brankov, J. G.; Chapman, D.; Anastasio, M. A.; Yang, Y. Y.; Zhong, Z.; Wernick, M. N. *Physics in Medicine and Biology* **2006**, *51*, 221–236.

(21) Oltulu, O.; Zhong, Z.; Hasnah, M.; Wernick, M. N.; Chapman, D. *Journal of Physics D-Applied Physics* **2003**, *36*, 2152–2156.

(22) Pagot, E.; Cloetens, P.; Fiedler, S.; Bravin, A.; Coan, P.; Baruchel, J.; Hartwig, J.; Thomlinson, W. *Applied Physics Letters* **2003**, *82*, 3421–3423.

(23) Chou, C. Y.; Anastasio, M. A.; Brankov, J. G.; Wernick, M. N.; Brey, E. M.; Connor, D. M.; Zhong, Z. *Physics in Medicine and Biology* **2007**, *52*, 1923–1945.

(24) Rigon, L.; Besch, H. J.; Arfelli, F.; Menk, R. H.; Heitner, G.; Plothow-Besch, H. *Journal of Physics D-Applied Physics* **2003**, *36*, A107–A112.

(25) Rigon, L.; Arfelli, F.; Menk, R. H. *Applied Physics Letters* **2007**, *90*.

(26) Rigon, L.; Arfelli, F.; Menk, R. H. *Journal of Physics D-Applied Physics* **2007**, *40*, 3077–3089.

(27) Pavlov, K. M.; Kewish, C. M.; Davis, J. R.; Morgan, M. J. *Journal of Physics D-Applied Physics* **2001**, *34*, A168–A172.

(28) Nesterets, Y. I.; Gureyev, T. E.; Paganin, D.; Pavlov, K. M.; Wilkins, S. W. *Journal of Physics D-Applied Physics* **2004**, *37*, 1262–1274.

(29) Dilmanian, F. A.; Zhong, Z.; Ren, B.; Wu, X. Y.; Chapman, L. D.; Orion, I.; Thomlinson, W. C. *Physics in Medicine and Biology* **2000**, *45*, 933–946.

(30) Zhu, P. P.; Wang, J. Y.; Yuan, Q. X.; Huang, W. X.; Shu, H.; Gao, B.; Hu, T. D.; Wu, Z. Y. *Applied Physics Letters* **2005**, *87*.

(31) Sun, Y.; Zhu, P. P.; Yu, J.; Chen, X. *Computerized Medical Imaging and Graphics* **2007**, *31*, 383–389.

(32) Nesterets, Y. I.; Gureyev, T. E.; Wilkins, S. W. *Applied Physics Letters* **2006**, *89*.

(33) Brankov, J. G.; Wernick, M. N.; Yang, Y. Y.; Li, J.; Muehleman, C.; Zhong, Z.; Anastasio, M. A. *Medical Physics* **2006**, *33*, 278–289.

(34) Majidi, K.; Wernick, M. N.; Li, J.; Muehleman, C.; Brankov, J. G. *Physics in Medicine and Biology* **2014**, *59*, 3483–3500.

(35) Rigon, L.; Astolfo, A.; Arfelli, F.; Menk, R.-H. *European Journal of Radiology* **2008**, *68*, S3–S7.

(36) Maksimenko, A.; Ando, M.; Hiroshi, S.; Yuasa, T. *Applied Physics Letters* **2005**, *86*.

(37) Wang, M.; Zhu, P. P.; Zhang, K.; Hu, X. F.; Huang, W. X.; Cen, Y. W.; Yuan, Q. X.; Yu, X. L.; Wang, J. Y. *Journal of Physics D-Applied Physics* **2007**, *40*, 6917–6921.

(38) Li, J.; Sun, Y. *Optics Communications* **2012**, *285*, 2972–2975.

(39) Bravin, A.; Keyrilainen, J.; Fernandez, M.; Fiedler, S.; Nemoz, C.; Karjalainen-Lindsberg, M. L.; Tenhunen, M.; Virkkunen, P.; Leidenius, M.; von Smitten, K.; Sipila, P.; Suortti, P. *Physics in Medicine and Biology* **2007**, *52*, 2197–2211.

(40) Rocha, H. S.; Pereira, G. R.; Faria, P.; Kellermann, G.; Mazzaro, I.; Tirao, G.; Giles, C.; Lopes, R. T. *European Journal of Radiology* **2008**, *68*, S37–S40.

(41) Castelli, E. et al. *Radiology* **2011**, *259*, 684–694.

(42) Antunes, A.; Honnicke, M. G.; Safatle, A. M. V.; Cusatis, C.; Barros, P. S. M.; Morelhao, S. L. *Nuclear Instruments & Methods in Physics Research Section B-Beam Interactions with Materials and Atoms* **2005**, *238*, 28–31.

(43) Koyama, I.; Momose, A.; Wu, J.; Lwin, T. T.; Takeda, T. *Japanese Journal of Applied Physics Part 1-Regular Papers Brief Communications & Review Papers* **2005**, *44*, 8219–8221.

(44) Rhoades, G. W.; Belev, G. S.; Chapman, L. D.; Wiebe, S. P.; Cooper, D. M.; Wong, A. T. F.; Rosenberg, A. M. *Comparative Medicine* **2015**, *65*, 342–347.

(45) Izadifar, Z.; Honaramooz, A.; Wiebe, S.; Belev, G.; Chen, X. B.; Chapman, D. *Biomaterials* **2016**, *82*, 151–167.

(46) Coan, P.; Mollenhauer, J.; Wagner, A.; Muehleman, C.; Bravin, A. *European Journal of Radiology* **2008**, *68*, S41–S48.

(47) Xia, C. C.; Yadav, A. K.; Zhang, K.; Peng, Y. F.; Yuan, Q. X.; Zhu, P. P.; Feng, L. J.; Xu, X. D.; Wu, A. S.; Tang, G. Y. *Journal of X-Ray Science and Technology* **2016**, *24*, 145–159.

(48) Bravin, A.; Coan, P.; Suortti, P. *Physics in Medicine and Biology* **2013**, *58*, R1–R35.

(49) Müller, B. R.; Hentschel, M. P. *X-Ray Spectrometry* **2004**, *33*, 402–406.

(50) Müller, B. R.; Lange, A.; Harwardt, M.; Hentschel, M. P.; Illerhaus, B.; Goebbels, J.; Bamberg, J.; Heutling, F. *Materials Testing* **2004**, *46*, 314–319.

(51) Müller, B. R.; Lange, A.; Harwardt, M.; Hentschel, M. P. *Advanced Engineering Materials* **2009**, *11*, 435–440.

(52) De Andrade Silva, F.; Williams, J. J.; Müller, B. R.; Hentschel, M. P.; Portella, P. D.; Chawla, N. *Metallurgical and Materials Transactions A* **2010**, *41*, 2121–2128.

(53) Kupsch, A.; Lange, A.; Hentschel, M. P.; Onel, Y.; Wolk, T.; Staude, A.; Ehrig, K.; Müller, B. R.; Bruno, G. *Journal of Ceramic Science and Technology* **2013**, *4*, 169–175.

(54) Müller, B. R.; Cooper, R. C.; Lange, A.; Kupsch, A.; Wheeler, M.; Hentschel, M. P.; Staude, A.; Pandey, A.; Shyam, A.; Bruno, G. *Acta Materialia* **2018**, *144*, 627–641.

(55) Cabeza, S.; Müller, B. R.; Pereyra, R.; Fernández, R.; González-Doncel, G.; Bruno, G. *Journal of Applied Crystallography* **2018**, *51*, 420–427.

(56) Kupsch, A.; Müller, B. R.; Lange, A.; Bruno, G. *Journal of the European Ceramic Society* **2017**, *37*, 1879–1889.

(57) Buzug, T. M., *Computed Tomography*; Springer, Berlin/Heidelberg: 2008.

(58) Goebbels, J. In, Czichos, H., Ed.; Springer, Berlin/Heidelberg: 2013; Chapter Computed Tomography.

(59) Hsieh, J., *Computed Tomography: Principles, Design, Artifacts, and Recent Advances, Third Edition*; SPIE Press Books: 2015.

(60) Kastner, J.; Heinzel, C. In, Liu, Z., Ukida, H., Ramuhalli, P., Niel, K., Eds.; Springer London: 2015; Chapter X-ray Computed Tomography for Non-destructive Testing and Materials Characterization.

(61) *Industrial X-Ray Computed Tomography*; Carmignato, S., Dewulf, W., Leach, R., Eds.; Springer, Cham: 2018.

(62) Görner, W.; Hentschel, M. P.; Müller, B. R.; Riesemeier, H.; Krumrey, M.; Ulm, G.; Diete, W.; Klein, U.; Frahm, R. *Nuclear Instruments and Methods in Physics Research Section A: Accelerators, Spectrometers, Detectors and Associated Equipment* **2001**, *467-468, Part 1*, 703–706.

(63) Rack, A.; Zabler, S.; Müller, B. R.; Riesemeier, H.; Weidemann, G.; Lange, A.; Goebbels, J.; Hentschel, M.; Görner, W. *Nuclear Instruments & Methods in Physics Research Section A-Accelerators Spectrometers Detectors and Associated Equipment* **2008**, *586*, 327–344.

(64) Henke, B.; Gullikson, E.; Davis, J. *Atomic Data and Nuclear Data Tables* **1993**, *54*, 181 –342.

(65) Kak, A. C.; Slaney, M., *Principles of Computerized Tomographic Imaging*; IEEE Press: 1988.

(66) Klobes, P.; Meyer, K.; Munro, R. G., *Porosity and Specific Surface Area Measurements for Solid Materials*; NIST: 2006.

(67) Schindelin, J. et al. *Nat. Meth.* **2012**, *9*, 676–682.

(68) Arganda-Carreras, I.; Sorzano, C. O. S.; Marabini, R.; Carazo, J. M.; Ortiz-de Solorzano, C.; Kybic, J. In *Computer Vision Approaches to Medical Image Analysis*, ed. by Beichel, R. R.; Sonka, M., Springer Berlin Heidelberg: Berlin, Heidelberg, 2006, pp 85–95.

(69) Laquai, R.; Schaupp, T.; Müller, B. R.; Griesche, A.; Bruno, G.; Kannengiesser, T. In *International Symposium of Non-Destructive Testing in Civil Engineering (NDTCE 2015)*, 2015.

(70) Huang, L.-K.; Wang, M.-J. J. *Pattern Recognition* **1995**, *28*, 41 –51.

(71) Cloetens, P.; Ludwig, W.; Baruchel, J.; Van Dyck, D.; Van Landuyt, J.; Guigay, J. P.; Schlenker, M. *Applied Physics Letters* **1999**, *75*, 2912–2914.

(72) Nellesen, J.; Laquai, R.; Müller, B. R.; Kupsch, A.; Hentschel, M. P.; Anar, N. B.; Soppa, E.; Tillmann, W.; Bruno, G. *Journal of Materials Science* **2018**, *53*, 6021–6032.

(73) Clyne, T. W.; Withers, P. J., *An Introduction to Metal Matrix Composites*; Cambridge Solid State Science Series; Cambridge University Press: 1993.

(74) Buffière, J.-Y.; Maire, E.; Verdu, C.; Cloetens, P.; Pateyron, M.; Peix, G.; Baruchel, J. *Materials Science and Engineering: A* **1997**, *234-236*, 633 –635.

(75) Buffière, J.-Y; Maire, E; Cloetens, P; Lormand, G; Fougères, R *Acta Materialia* **1999**, *47*, 1613 –1625.

(76) Babout, L.; Maire, E.; Buffièere, J.-Y.; Fougères, R. *Acta Materialia* **2001**, *49*, 2055 –2063.

(77) Borbély, A.; Biermann, H.; Hartmann, O.; Buffière, J.-Y. *Computational Materials Science* **2003**, *26*, 183 –188.

(78) Babout, L.; Maire, E.; Fougères, R. *Acta Materialia* **2004**, *52*, 2475 –2487.

(79) Khor, K. H.; Buffière, J.-Y.; Ludwig, W.; Toda, H.; Ubhi, H. S.; Gregson, P. J.; Sinclair, I. *Journal of Physics: Condensed Matter* **2004**, *16*, S3511.

(80) Buffière, J.-Y.; Proudhon, H.; Ferrie, E.; Ludwig, W.; Maire, E.; Cloetens, P. *Nuclear Instruments and Methods in Physics Research Section B: Beam Interactions with Materials and Atoms* **2005**, *238*, 75 –82.

(81) Ferrié, E.; Buffière, J.-Y.; Ludwig, W.; Gravouil, A.; Edwards, L. *Acta Materialia* **2006**, *54*, 1111 –1122.

(82) Maire, E.; Carmona, V.; Courbon, J.; Ludwig, W. *Acta Materialia* **2007**, *55*, 6806 –6815.

(83) Tomasi, C.; Manduchi, R. In *6th International Conference on Computer Vision*, 1998, pp 839–846.

(84) Laquai, R.; Müller, B. R.; Kasperovich, G.; Haubrich, J.; Requena, G.; Bruno, G. *Materials Research Letters* **2018**, *6*, 130–135.

(85) Laquai, R.; Müller, B. R.; Kasperovich, G.; Requena, G.; Haubrich, J.; Bruno, G. *Materials Performance and Characterization* **2020**, *9*, 82–93.

(86) Yap, C. Y.; Chua, C. K.; Dong, Z. L.; Liu, Z. H.; Zhang, D. Q.; Loh, L. E.; Sing, S. L. *Applied Physics Reviews* **2015**, *2*, 041101.

(87) Thijs, L.; Verhaeghe, F.; Craeghs, T.; van Humbeeck, J.; Kruth, J.-P. *Acta Materialia* **2010**, *58*, 3303–3312.

(88) Leuders, S.; Thöne, M.; Riemer, A.; Niendorf, T.; Tröster, T.; Richard, H.; Maier, H. *International Journal of Fatigue* **2013**, *48*, 300 –307.

(89) Gong, H.; Rafi, K.; Gu, H.; Janaki Ram, G. D.; Starr, T.; Stucker, B. *Materials & Design* **2015**, *86*, 545 –554.

(90) Khairallah, S. A.; Anderson, A. T.; Rubenchik, A.; King, W. E. *Acta Materialia* **2016**, *108*, 36 –45.

(91) Leuders, S.; Meiners, S.; Wu, L.; Taube, A.; Tröster, T.; Niendorf, T. *Journal of Materials Processing Technology* **2017**, *248*, 130 –142.

(92) Kabir, M. R.; Richter, H. *Materials* **2017**, *10*, 145.

(93) Kasperovich, G.; Hausmann, J. *Journal of Materials Processing Technology* **2015**, *220*, 202 –214.

(94) Günther, J.; Krewerth, D.; Lippmann, T.; Leuders, S.; Tröster, T.; Weidner, A.; Biermann, H.; Niendorf, T. *International Journal of Fatigue* **2017**, *94*, 236 –245.

(95) Kasperovich, G.; Haubrich, J; Gussone, J.; Requena, G. *Materials & Design* **2016**, *105*, 160 –170.

(96) Vrancken, B.; Thijs, L.; Kruth, J.-P.; van Humbeeck, J. *Journal of Alloys and Compounds* **2012**, *541*, 177 –185.

(97) Cain, V.; Thijs, L.; van Humbeeck, J.; van Hooreweder, B.; Knutsen, R. *Additive Manufacturing* **2015**, *5*, 68 –76.

(98) Chastand, V.; Tezenas, A.; Cadoret, Y.; Quaegebeur, P.; Maia, W.; Charkaluk, E. *Procedia Structural Integrity* **2016**, *2*, 3168 –3176.

(99) Oriani, R. A. *Corrosion* **1987**, *43*, 390–397.

(100) Lynch, S. *Corrosion Reviews* **2012**, *30*, 105.

(101) Oriani, R. A. *Berichte der Bunsengesellschaft für physikalische Chemie* **1972**, *76*, 848–857.

(102) Birnbaum, H.; Sofronis, P. *Materials Science and Engineering: A* **1994**, *176*, 191 –202.

(103) Kandasamy, K.; Lewis, F. *International Journal of Hydrogen Energy* **1999**, *24*, 763 –769.

(104) Hadam, U.; Zakroczymski, T. *International Journal of Hydrogen Energy* **2009**, *34*, 2449 –2459.

(105) Beyer, K.; Kannengiesser, T.; Griesche, A.; Schillinger, B. *Nuclear Instruments and Methods in Physics Research Section A: Accelerators, Spectrometers, Detectors and Associated Equipment* **2011**, *651*, 211 –215.

(106) Griesche, A.; Solòrzano, E.; Beyer, K.; Kannengiesser, T. *International Journal of Hydrogen Energy* **2013**, *38*, 14725–14729.

(107) Dabah, E.; Kannengiesser, T.; Eliezer, D.; Boellinghaus, T. In *Mechanical Stress Evaluation by Neutrons and Synchrotron Radiation VI*, Trans Tech Publications Ltd: 2014; Vol. 772, pp 91–95.

(108) Fabrègue, D.; Deschamps, A.; Suéry, M.; Proudhon, H. *Scripta Materialia* **2008**, *59*, 324–327.

(109) Kannengiesser, T.; Rethmeier, M.; Portella, P. D.; Ewert, U.; Redmer, B. *International Journal of Materials Research* **2011**, *102*, 1001–1006.

(110) Williams, J.; Yazzie, K.; Padilla, E.; Chawla, N.; Xiao, X.; De Carlo, F. *International Journal of Fatigue* **2013**, *57*, 79–85.

(111) Zhang, H.; Toda, H.; Qu, P.; Sakaguchi, Y.; Kobayashi, M.; Uesugi, K.; Suzuki, Y. *Acta Materialia* **2009**, *57*, 3287–3300.

(112) Gamboa, E.; Giuliani, M.; Lavigne, O. *Scripta Materialia* **2014**, *81*, 1–3.

(113) Salmi, S.; Rhode, M.; Jüttner, S.; Zinke, M. *Welding in the World* **2015**, *59*, 137–144.

(114) Rhode, M.; Schaupp, T.; Muenster, C.; Mente, T.; Boellinghaus, T.; Kannengiesser, T. *Welding in the World* **2019**, *63*, 511–526.

(115) Buades, A.; Coll, B.; Morel, J.-M. *Image Processing On Line* **2011**, *1*, 208–212.

List of own publications

The content of this work was disseminated to the scientific community through the following publications.

Articles in peer-reviewed journals:

J. Nellesen, R. Laquai, B. R. Müller, A. Kupsch, M. P. Hentschel, N. B. Anar, E. Soppa, W. Tillmann and G. Bruno. In situ analysis of damage evolution in an Al/Al_2O_3 MMC under tensile load by sychrotron X-ray refraction imaging. *Journal of Materials Science*, 53(8):6021-6032, 2018.

R. Laquai, B . R. Müller, G. Kasperovich, J. Haubrich, G. Requena and G. Bruno. X-ray refraction distinguishes unprocessed powder from empty pores in selective laser melting Ti-6Al-4V. *Materials Research Letters*, 6(2):130-135, 2018.

R. Laquai, B. R. Müller, G. Kasperovich, G. Requena, J. Haubrich, and G. Bruno. Classication of defect types in SLM Ti-6Al-V4 by X-ray refraction topography. *Materials Performance and Characterization* , 9(1):82-93, 2020.

Contributions to national and international conferences:

R. Laquai, T. Schaupp, B. R. Müller, A. Griesche, G. Bruno and T. Kannengiesser. 3D imaging of hydrogen assisted cracking in metals using refraction enhanced synchrotron CT. *International Symposium of Non-Destructive Testing in Civil Engineering (NDTCE 2015)*, 15-17 Sep 2015, Berlin, Germany.

R. Laquai, T. Schaupp, B. R. Müller, A. Griesche, A. Kupsch, A. Lange, T. Kannengiesser and G. Bruno. 3D crack analysis in hydrogen charged lean duplex stainless steel with synchrotron refraction CT. *19th World Conference on Non-Destructive Testing (WCNDT 2016)*, 13-17 June 2016, Munich, Germany.

R. Laquai, B. R. Müller, J. Nellesen, M. P. Hentschel, A. Kupsch and W. Tillmann. Synchrotron-Refraktion mit in-situ-Zugbelastung zur Charakterisierung der Schadensentwicklung in Metall-Matrix-Kompositen. *DGZfP Jahrestagung 2017*, 22-24 May, Koblenz, Germany.

R. Laquai, B. R. Müller, G. Kasperovich, G. Requena and G. Bruno. Unterscheidung verschiedener charakteristischer Defekte in mittels selektivem Laserschmelzen hergestelltem Ti-6Al-4V durch Röntgen-Refraktionsradiographie. *DGZfP Jahrestagung 2018*, 7-9 May 2018, Leipzig, Germany.

Additional publications in peer-reviewed journals whose content is not part of this thesis but which are related to this work by use of the same X-ray refraction imaging methods:

R. Laquai, F. Gouraud, B. R. Müller, M. Huger, T. Chotard, G. Antou and G. Bruno. Evolution of Thermal Microcracking in Refractory ZrO_2-SiO_2 after Application of External Loads at High Temperatures. *Materials*, 12(7), 2019.

R. Laquai, B. R. Müller, J. A. Schneider, A. Kupsch and G. Bruno. Using SXRR to Probe the Nature of Discontinuities in SLM Additive Manufactured Inconel 718 Specimens. *Metallurgical and Materials Transactions A*, 51(6):3194-3204, 2020.